Vortices in a Highly Rotating Bose Condensed Gas

by

I. R. Coddington

B.A., Reed College, 1998

A thesis submitted to the

Faculty of the Graduate School of the

University of Colorado in partial fulfillment

of the requirements for the degree of

Doctor of Philosophy

Department of Physics

2004

This thesis entitled:
Vortices in a Highly Rotating Bose Condensed Gas
written by I. R. Coddington
has been approved for the Department of Physics

Eric Cornell

Leo Radzihovsky

Date

The final copy of this thesis has been examined by the signatories, and we find that both the content and the form meet acceptable presentation standards of scholarly work in the above mentioned discipline.

Coddington, I. R. (Ph.D., Physics)

Vortices in a Highly Rotating Bose Condensed Gas

Thesis directed by Prof. Eric Cornell

Superfluids, with their dissipationless flow and exotic topologies, have puzzled researchers in diverse fields of physics for almost a century. One of the hallmark features of superfluids is their response to rotation, which requires the fluid to be pierced by an array quantized singularities or vortices. Over the past few years, vortices and the lattices they organize into have become one of the major fields of experimental research with dilute gas Bose-Einstein condensates.

This thesis explores the physics of vortices and vortex lattices in the dilute gas Bose-Einstein condensate while drawing connections to other superfluid systems. In addition to characterizing several equilibrium vortex effects, this work also studies several excitations. By removing atoms from the rotating condensate with a tightly focused, resonant laser, the density can be locally suppressed, creating aggregate vortices containing many units of circulation. These so called "giant vortices" offer insight into the dynamical stability of density defects in this system. Using similar techniques we can excite and directly image Tkachenko waves in the vortex. These low frequency modes are a consequence of the small but nonvanishing elastic shear modulus of the vortex-filled superfluid.

Finally, by working at extremely high rotations we can create a Bose-Einstein condensates in the lowest Landau level. In this regime, which requires rotation rates greater than 99% of the centrifugal limit for a harmonically trapped gas, we are able observe several expected and unexpected shifts in the physical properties of the condensate.

In conclusion the dilute gas Bose-Einstein condensates offers a rich system in which to study vortex physics, and explore dynamical effects common to all rotating

superfluids.

Dedication

To Odele for her love and support, and to my grandfather for getting me thinking about the world.

Acknowledgements

First I would like to thank my advisor, Eric Cornell, for his support and guidance over the last five years. His infectious enthusiasm and depth of knowledge never ceased to amaze me and both were a constant source of my own growth and understanding.

Also, I would like to thank Debbie Jin for her hands on approach and guidance that first year. I learned a lot in a very short period of time. We never ended up needing that stripe laser but I also never stopped using the skills I learned, either.

In the last five years it has been my pleasure share the lab with several other graduate students including Volker Schweikhard, Paul Haljan, and most recently Shih-Kuang Tung. It would be hard to ask for a brighter or more dedicated group of individuals. Even more exceptionally, this group has always been humorous and fun to work with no matter how arduous or frustrating the experiment became. Of course, no discussion of the lab group would be complete without acknowledging our ring leader and post doc Peter Engels. Over the last several years Peter has been both a great mentor as well as a personal friend, and I wish him luck in his new job. He may not believe me, but there is no doubt in my mind that Peter will grow to love his new appointment at Washington State.

This experiment has also benefited considerably from the assistance of a number of theorists. It has been an absolute pleasure to work with and learn from people like Leo Radzihovsky, Dan Sheehy, Gordon Baym, Allen MacDonald and Marco Cozzini.

Support services at JILA are of course outstanding and I could not even begin

to count all the ways that the machine shop, electronics shop and computing staff have made this thesis more successful. I would especially like to thank Hans Green and James Fung-A-Fat for their mentorship and patience. Also, I am eternally indebted to Jim McKown for tolerating, what I am sure were, inane questions about the inner workings of Windows and then miraculously making the problems go away.

Thanks, also, to the Cornell-Wieman-Jin group for an excellent working atmosphere and to the "Sloggies" Dave, Nate, Dan, and Andrew for an excellent living atmosphere.

Finally, thanks to the coffee girl and Burnt Toast for making such a good cup of coffee. Thanks to Mike Ziemkiewicz and to a lesser extent John Stewart of The Daily Show for making the last four years of presidential politics bearable.

Contents

Chapter

Tables

Table

Figures

Figure

Chapter 1

Introduction

1.1 Superfluids great and small

Traditionally in physics one learns that the world is divided into two. There is the microscopic world of quantum mechanics and there is the macroscopic world where classical physics still reigns. Superfluids are astonishing in that they shatter this barrier between worlds. These highly quantum systems can exist on length scale of a μm, a cm, or even 10^4 km. With their dissipationless flow and exotic topologies such fluids have puzzled researchers in diverse fields of physics for almost a century.

An understanding of superfluids starts with the early 1920's work of Satyendra Nath Bose [5] and Albert Einstein [6]. In these papers they argue that at a small but finite temperature a gas of bosons will quickly collect in the ground state. This transition to the ground state far exceeds the expectation for an equally cold ideal gas of atoms and can result in a nearly complete occupation of a single quantum state. This condensation, although an impressive first step, is however not sufficient to explain superfluidity. It was Fritz London [7, 8] who, while trying to explain the phenomena observed in superfluid Helium in the 1930's, would suggest that this macroscopically occupied state is governed by a single wave function, or order parameter, of the form

$$\Psi = \sqrt{\rho(\vec{r})}e^{iS(\vec{r})} \ . \tag{1.1}$$

In the 1930's this was a radical idea but even today it is a little unsettling to think

a thousand atoms, or a million atoms, or even Avagadro's number of atoms could be described by a single wavefunction commonly associated with a single particle. Ultimately what makes superfluids so interesting is that this macroscopic wavefunction extends quantum mechanics into the macroscopic world.

The experimental side of the story of superfluids arguably begins with Kamerlingh Onnes [9] who was, in many ways, the Christopher Columbus of superfluids. Onnes was first to liquify ^{4}He and in 1908 he was attempting to cool this new liquid further in order to produce solid ^{4}He. While unsuccessful in this attempt, Onnes did cool the liquid well into the superfluid regime that would later be called He II. Unfortunately Onnes did not recognize the superfluid for what it was. It would take 30 more years before a study of He II would find it to have no viscosity and for the term "superfluid" to be coined.

In the mean time Kamerlingh Onnes was at it again. It was 1911 and Onnes was attempting to understand the change in resistivity of a metal at very low temperatures. Mercury was chosen for the experiment because the metal could be cooled effectively. From here the story is well known. As Onnes cooled his mercury sample, the resistivity decreased roughly as expected until reaching 4.2 K, at which point a most unexpected thing happened, the resistivity of the sample dropped abruptly to zero. Onnes had made the first observation of superconductivity. A theoretical description of superconductivity would take much more time but ultimately Bardeen, Cooper and Schrieffer would demonstrate that the pairing of electrons into Cooper pairs would allow fermions to condense like bosons. Thus superconductors, like He II, become governed by a single coherent wavefunction.

Over the years many other similar systems have been discovered. In 1971 Lee, Osheroff and Richardson discovered two superfluid phases in the fermionic liquid ^{3}He. Like superconductors ^{3}He condenses through the pairing of fermionic atoms. Much as electrons in a superconductor sense each other through a Coulomb repulsion, the ^{3}He atoms interact via their strong magnetic moments. This super system has generated

a great deal of interest due to its relative accessibility [9]. The lack of background lattice structure or impurities make this system clean to work with and the magnetic susceptibility makes NMR a convenient diagnostic tool.

Superfluids are not just exotic laboratory creations, but can also occur in nature. Neutron stars, some of which predate Onnes' work by 10^7 years, are predicted to have a superfluid interior. Such neutron stars are a superfluid system that truly stretches the definition of "low" temperature. Having a density of roughly $10^{14}\, g/cm^3$ [10] these stars are thought to contain paired neutrons with a critical temperature, Tc, of roughly 10^9 K. Meanwhile core temperature of these stars is predicted to be a fairly cool couple-million K suggesting a highly degenerate state for the paired neutrons (and to a lesser degree paired-protons and paired-electrons [11]).

Contrasting starkly with the neutron star is a recent addition to the family of superfluids and the subject of this thesis, the dilute gas Bose-Einstein Condensate (BEC). Weighing in at densities of $10^{-11} - 10^{-13}\, g/cm^3$ these condensates exist at temperatures ranging from μK to pK. These systems are clearly more experimentally accessible than their astrological counterpart, and their dilute nature considerably simplifies the theory. The low density and weak interactions also lead to a much higher condensate fraction (nearly 100%) than the other systems discussed here (He II for example is only 10% condensate) [9].

Finally one should mention the newest addition to the superfluid family, the Fermionic condensates [12, 13, 14]. First observed in 2003, it is probably too soon to know exactly where this dilute gas system stands with respect to the other superfluid systems. However, it is clear that this promising new system will be able to probe the gap between fermion and bosonic supersystems. With the addition of this new system it is also clear that the superfluid field is still very much alive and developing.

1.2 Vortices

One of the most distinct features of superfluidity is its response to rotation or, equivalently, to an applied magnetic field in the case of superconductors. In any wavefunction, rotation manifests itself as a phase gradient along the direction of flow. More specifically, a loop integral around the center of rotation of the superfluid must yield a net change in phase regardless of loop size. At the same time the wavefunction of a superfluid must be, in all places, single valued. In the 1950's, Onsager [15] and Feynman [16] observed that quantized vortices, or tiny tornados in the fluid, were needed to fill such requirements and allow for rotation. Each vortex can be thought of as a quantum of angular momentum and contains, at its center, a phase singularity around which an integer 2π phase winding occurs. This integer 2π winding, and fluid depletion at the vortex center allow for the wavefunction to be single valued while providing the necessary phase gradient for rotation. Without these singularities the fluid velocity field is curl free and cannot support circulation. This is why superfluids without vortices are considered irrotational. It is interesting to think that a vortex-free superfluid is rotationally at rest, not in the lab frame or Earth frame, but with respect to some greater axis in the Universe.

When thinking of rotation one tends to visualize the typically classical, rigid-body rotation of a record on a player or a tire. It should be noted that the presence of a single vortex in a superfluid leads to an extremely non-rigid body flow. In this case, flow is rapid near the center of the vortex, where the phase gradient is steep and falls off as $1/r$ where r is the distance from the vortex center. However with increased rotation more vortices can be added to a superfluid. The repulsive vortex-vortex interaction causes vortices to distribute about the fluid and form a triangular lattice, or Abrikosov lattice seen in figure 1.1 a). As one would expect, with increasing quanta of angular momentum the system begins to behave classically, and this distribution of vortices

across the superfluid causes the system to rotate in an increasingly rigid-body like manner.

Not surprisingly, vortices can have profound effects on the system. For superconductors in sufficiently high magnetic fields, vortices can consume the sample and force it into a normal state [19]. In superfluid He II systems the generation of "vortex tangles" leads to finite viscosity even for flows below the critical velocity [9]. In neutron stars it is predicted that vortices, pinned to the crust of the star, can break free in an avalanche of vortex motion that causes the rotation of the entire core of the star to jump irregularly.

Vortices in a rotating dilute gas Bose-Einstein condensate [20, 21, 22, 23, 24, 25] are no exception and many of the profound effects they have on the BEC system will be detailed in the rest of this thesis. The study of vortices, in a dilute gas BEC is in no small way motivated by the connections shared with these other supersystems. We are blessed in that there has clearly been decades of work in these other systems that can guide our research. We are also blessed in that the BEC's offer a very clean system in which to study vortex effects. The perfectly smooth magnetic potential used to confine a BEC makes us immune to the effects of vortex pinning that complicates studies in other systems. Additionally, impurity isotopes are simply not an issue. Also interactions in the dilute BEC system are well understood making comparison with theory much easier. Thus, while BECs can mimik superfluid effects seen in other systems, they also promise novel effects of their own.

Tkachenko oscillations, or sound waves in a vortex lattice, represent a striking example of the interconnected nature of superfluid vortex systems. Tkachenko proposed that the triangular, Abrikosov, lattice structure seen in superconductors would also be supported in superfluid Helium. In a 1966 mathematical tour de force [26], Tkachenko demonstrated that this lattice structure should support sound waves. These elliptically polarized transverse waves in the lattice would later be dubbed Tkachenko modes. Tkachenko was so certain of this prediction that he spent the rest of his life looking for

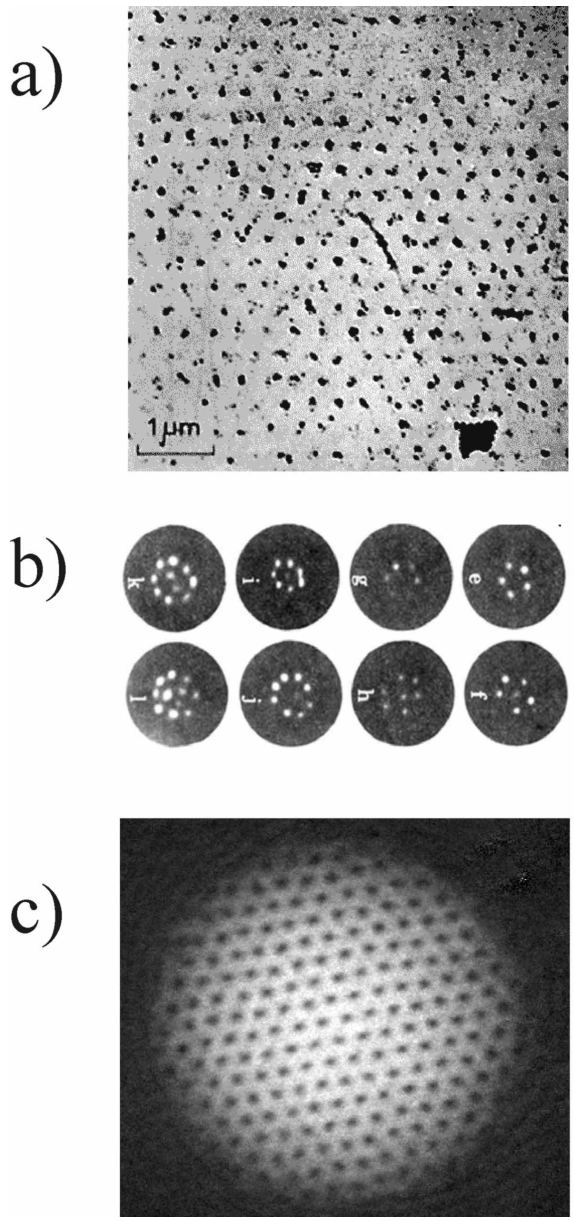

Figure 1.1: Vortices in supersystems. Image a) the first image of an Abrikosov lattice taken in 1967 [17]. Black dots are cobalt particles that are attracted to the magnetic field of the vortices in this superconducting lead rod. Image b) pictures of vortices in He II taken in 1979 by Yarmchuk **et al.** [18] In a heroic experiment, impurity ions where added to the superfluid and became trapped in the vortex cores. Images were taken by adding a strong electric field to project the ions onto a phosphorous screen that could be imaged onto film. Image c) vortices in a rotating Bose-Einstein condensate taken at JILA in 2003.

these excitations in He II, but ultimately met with frustration. It was Glaberson [27] who would first report a signature of these modes in He II. Performing a rotating disk experiment, Glaberson measured the response of the system at different excitation frequencies. While these experiments ultimately demonstrated the existence of Tkachenko modes they were a little unsatisfactory in that they necessitated the simultaneous excitation of many Tkachenko modes. Worse still, vortex pinning effects coupled the Tkachenko modes to other modes in the system, and ultimately it was impossible to study a Tkachenko mode in isolation. This would remain the state of the field for some time...

1.3 Rotating Bose-Einstein condensates

Recently Anglin and Crescimanno have predicted that these modes should exist in a dilute gas BEC [28]. In this initial work they develop a hydrodynamic theory of vortices that accounts for the finite and inhomogeneous density profile of the condensate. This paper yields several interesting results, the most relevant of which is that there exists a radially symmetric mode in condensates with a wavelength on the order of the condensate radius. This mode, dubbed the (1,0) mode, is predicted to have a frequency far smaller than any previously observed bulk fluid mode of the condensate. Two interesting observations about the vortex lattice can be made from the existence of this mode. First, the radially symmetric "s-bend" that it induces in the lattice could only be possible in the presence of a finite shear modulus. A finite shear modulas is not normally associated with a superfluid and could only exist because the superfluid is permeated with the vortex lattice. Secondly, the extremely low frequency of this mode suggests that this shear modulus is quite small and that the lattice is potentially very delicate under shear.

In Anglin and Crescimanno's notation the (1,0) mode corresponds to one radial node and zero azimuthal nodes. While this thesis primarily studies this one mode it

should be noted that there are others that are accessible or potentially accessible. As mentioned in §4.4 the (2,0) mode has been observed as well. Non-radially symmetric modes are also predicted and it is a little surprising that they have never been detected. The (0,2) mode in particular is predicted to be an extremely low energy mode (sub 1 Hz frequency for our system) and one might expect it to exist in nearly any vortex lattice.

By mid 2002 we began the study of Tkachenko modes in our dilute gas BEC. We are able to observe these modes quite easily, in contrast to He II where such modes are not directly observable. By gently perturbing the central density of the condensate we couple to a pure (1,0) Tkachenko mode. Because our initial conditions are so reproducible its becomes possible to map the vortex oscillation patterns in time, obtaining both oscillation frequency and an approximate wavelength. Surprisingly, as low as Anglin and Crescimanno's predicted Tkachenko frequencies are, our measured frequency is much lower, particulary at high rotation.

The explanation for this discrepancy would come in a slew of theory responses [29, 30, 31, 32, 33]. A particularly relevant point, made in nearly all of these works, is that Anglin and Crescimanno's theory is based on assumptions of incompressibility that are true in He II but not completely true for a highly rotating BEC. As the BEC rotation rate becomes comparable to the speed of sound the fluid becomes compressible. Interestingly this compressible regime is also expected to occur in neutron stars [34]. Accounting for compressibility effects lowers the predicted Tkachenko frequencies to a point where they are consistent with experiment.

A second effect, entering the lowest Landau level (LLL) regime, is also expected to decrease the lattice shear modulus and further lower the predicted Tkachenko frequencies. In the rotating frame and as the condensate rotation rate approaches the trapping frequency, the single-particle harmonic oscillator energy states organize into Landau levels or band like structures of nearly degenerate states. If condensate interactions are weaker than the energy splitting between Landau levels, then the condensate

primarily occupies the near-degenerate states of the lowest Landau level. This places significant constraints on the condensate wavefunction and one would expect to see a number of interesting effects including a weaker shear modulus in the vortex lattice [29].

Tkachenko modes aside, BECs in the lowest Landau level are intriguing on their own, as this system is somewhat analogous to type-II superconductors in a strong magnetic field [19]. In the extreme case exotic quantum Hall like effects are predicted to occur. For rotating BECs in the LLL, three regimes have been identified, distinguished by the filling factor (the ratio of atoms in the fluid to vortices). For high filling factors, the condensate is in the mean-field lowest Landau level regime [35, 19, 36] and forms an ordered vortex lattice ground state. Filling factors around 10, although currently out of reach, are expected to lead to melting of the vortex lattice. At such filling factors, the shear strength of the lattice is predicted to drop to a point where quantum fluctuations begin to melt the vortex lattice [37, 38], and a variety of strongly correlated vortex liquid states similar to those in the Fermionic fractional quantum Hall systems are predicted to appear [37]. For filling factors around 1, exotic quasiparticle excitations obeying fractional statistics [39] are predicted.

By monitoring the frequency of the (1,0) Tkachenko mode and the frequency of the axial breathing mode [40] we observe a transition to the 2D, high-filling factor, LLL regime. Two theory predictions in particular are addressed for this regime. First there is the Ho prediction [35] that the radial condensate profile should become gaussian as one enters the lowest Landau level. This prediction arises from the fact the condensate wavefunction in the lowest Landau level is so constrained that the position of the vortices dictates the entire condensate profile. If one assumes a perfect Abrikosov lattice then the resulting condensate profile is Gaussian. However our experimental observation shows a decidedly parabolic profile that implies that the lattice, far from the condensate center, distorts slightly as predicted by several other groups [41, 42, 43]. It is interesting to note that this predicted distortion closely resembles the lattice distortion predicted by

Sheehy and Radzihovsky [44] for the Thomas Fermi regime.

Also in the lowest Landau level the vortex core size becomes comparable to the lattice spacing. This is highly suggestive of type-II superconductors in a strong magnetic field where vortices become increasing tightly packed. When the applied magnetic field in these systems reaches a critical value (generally dubbed Hc_2) the vortices effectively swallow the entire system, forcing it into a normal state. In the dilute-gas BEC, early extrapolations from Thomas-Fermi theory [45, 46] suggest a similar effect. Alternatively it is argued by argued by Fischer and Baym [19] and Baym and Pethick [36] that kinetic energy considerations prevent this overlap and that the ratio of core size to spacing will ultimately saturate. A challenging set of experiments discussed in §5.5 demonstrates that the latter prediction is correct.

Multiply quantized vortices also offer intriguing comparisons across supersystems. Vortices discussed so far have all been singly quantized but, in principle, a vortex can have any integer 2π phase winding. Such multiply quantized vortices are just one of the exotic vortex phases seen in ^{3}He-A systems [47] and can also be observed at pinning sites in superconductors [48, 49, 50]. To date, doubly quantized vortices have been observed as the result of topological vortex formation [51], but higher quanta have not been observed. In this thesis, I discuss a somewhat less elegant means of forming a "giant" vortex. Here we suppress the fluid density in the center of the condensate by employing a focused, resonate laser to burn a hole in the cloud. This is not a true multiply-quantized vortex, since density suppression does not actually lead to vortex core overlap. Nonetheless, these experiments yield interesting information about the dynamical stability of such giant vortex features. The Giant vortex itself drastically demonstrates the effects of Coriolis force and the changed dynamics in the rapidly rotating system

1.4 Outlook

Predicting the future course of the TOP trap apparatus has traditionally been very hazardous. However, one obvious direction is the study of the exotic, low-filling-factor states discussed earlier. It should be noted however that this has also been our stated goal for much of the last three years. While this goal has yielded a great deal of interesting science, it has also become clear that low signal and fragile condensates will make low filling factors hard to achieve. There is some hope that the installation of an optical lattice could make this regime accessible and a serious effort to do so is currently underway.

On a separate note, vortex experiments could truly benefit from a Feshbach resonance. It is exciting to think that with such a resonance one could tune a rotating BEC from the He II regime to a compressible neutron star regime to the lowest Landau level regime, instantly and without adjusting atom number or rotation. Theory predictions have even suggested that with a Feshbach resonance, a rotating BEC could serve as nothing less then a model system for the expanding universe [52]. Unfortunately, this is complicated by the fact that our current atom, ^{87}Rb, does not offer any easily usable resonances [53]. On the plus side experience has taught me that while it is hazardous to predict the future of the TOP trap it is equally hazardous to rule anything out.

1.5 Thesis overview

The structure of this thesis is follows. Chapter 2 discusses experimental techniques for generating and imaging vortices. Chapter 3 is a discussion of giant vortices and dynamically stable density deformations in a rotating condensate. Chapter 4 details the excitation of the (1,0) and (2,0) Tkachenko modes in a vortex lattice. These modes are compared to theory and to similar bulk fluid modes of the condensate. Chapter 5 discusses the crossover to the lowest Landau level regime. Breathing modes and

Tkachenko modes are used to demonstrate two-dimensionality and passage into the lowest Landau level regime respectively. Additionally, the condensate and vortex density profiles in this regime are discussed, with particular attention paid to fractional core area effects. Finally, Chapter 6 characterizes several equilibrium vortex lattice effects. Specifically, we attempt precision measurements of vortex lattice spacing and the vortex core size over a range of condensate densities and rotation rates. Lastly, the effects of finite temperature on vortex contrast are studied.

Chapter 2

Experiment and Hardware

2.1 Generating highly rotating condensates

Highly rotating condensates are the bread and butter of this thesis and will be the starting point for every following chapter. Naturally this thesis would not be complete without a description of how these clouds are produced. It is worth noting that the techniques for creating highly rotating condensates have undergone only small refinements since originally being detailed by Paul Haljan [54].

Our experiment begins with a magnetically trapped cloud containing greater than 10^7 ^{87}Rb atoms in the $|F = 1, m_F = -1\rangle$ hyperfine ground state, cooled to a temperature roughly three times the critical temperature (T_c) for Bose condensation. Using a TOP trap we confine these atoms in an axially symmetric, oblate and harmonic potential with trapping frequencies ($\{\omega_\rho, \omega_z\} = 2\pi\{7, 13\}$Hz) with axis of symmetry along the vertical (z) axis. This trap is commonly referred to as the stirring trap as it is where we impart angular momentum to the thermal cloud. Rotation is generated in the thermal cloud by resonantly coupling to a scissors mode of the cloud [55, 56]. To do this we gradually apply an elliptical deformation to the magnetic trapping potential by distorting the amplitude of the rotating TOP field in time. The resulting distorted trap has roughly similar average radial-trapping frequency but an ellipticity in the horizontal plane of

0.25. Here trap ellipticity is defined as

$$\epsilon_{trap} = \frac{\omega_+^2 - \omega_-^2}{\omega_+^2 + \omega_-^2} \ . \tag{2.1}$$

where ω_+ and ω_- are the trap frequencies along the major and minor trap axis. The uncondensed cloud is held in this trap for 5 seconds while any excitations die out. At this point the angle of the major axis of the elliptically distorted trapping field is jumped quickly by 45 degrees in the horizontal plane to generate the initial conditions of the scissors mode. From here the cloud is allowed to evolve for 155 ms, or roughly one quarter period of the resulting scissors mode, at which point we transfer the cloud to a radially symmetric trap. Essentially we have caught the scissors oscillation between turning points where all the initial linear velocity has turned into rotational velocity. Using this method we can generate a cloud rotating at roughly half the radial trap frequency, with minimal heating. By lowering the amplitude of the trap distortion or the angle by which the trap is jumped, we can easily generate more slowly rotating clouds as well.

At this point we begin a second phase of rf evaporation, but this time we evaporate in one dimension along the axis of rotation [25, 54]. The motivation for this seemingly inefficient technique is that the 1D evaporation allows us to remove energy from the z axis of the condensate without preferentially removing high angular momentum atoms. Lowering the energy per particle without lowering the angular momentum per particle accelerates the cloud rotation rate Ω. To perform this 1D evaporation, we adiabatically ramp to a prolate geometry ($\{\omega_\rho, \omega_z\} = 2\pi\{8.3, 5.3\}$Hz) where the rest of the experiment is carried out. This prolate geometry is commonly referred to as the cigar trap.

Reaching significant rotation rates by the end of evaporation requires that the lifetime of the thermal cloud's angular momentum be comparable to the evaporation time. The nearly one-dimensional nature of the evaporation together with the low average trap frequencies makes cooling to BEC in the prolate trap very slow (2 minutes).

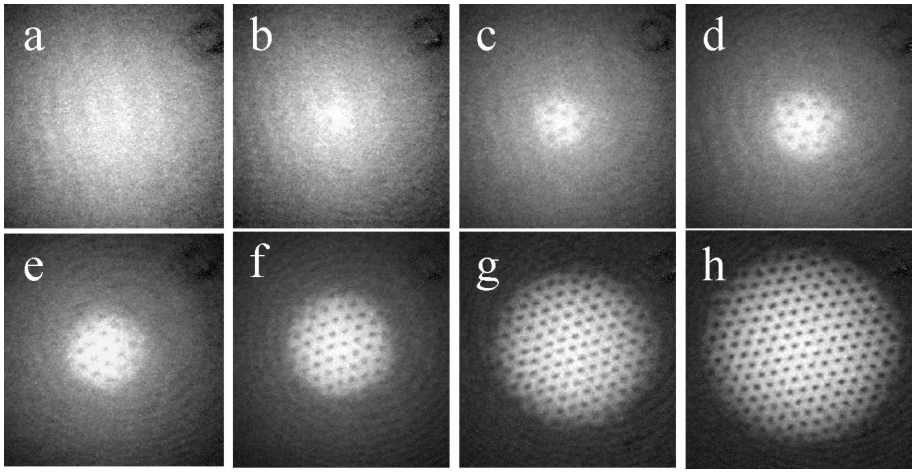

Figure 2.1: Growth of a rotating BEC from a rotating normal cloud. Pictures taken in expansion after different final rf frequencies of the evaporative cooling: (a) 2.65 MHz (pure normal cloud),(b) 2.6 MHz, (c) 2.58 MHz, (d) 2.57 MHz,(e) 2.55 MHz,(f) 2.5 MHz,(g) 2.4 MHz,(h) 2.35 MHz.

We obtain angular momentum lifetimes this long by shimming the TOP trap's rotating bias field to cancel the few percent azimuthal trap asymmetry that exists despite careful construction. With this technique we suppress the azimuthal trap ellipticity to less than one part in a thousand.

After the evaporation we have a condensate with as many as 4.5 million atoms and rotation rates from $\Omega = (0 - 0.975)\omega_\rho$, with no observable thermal cloud. Rotation can be accurately determined by comparing the condensate aspect ratio λ (defined as the axial Thomas-Fermi radius over the radial Thomas-Fermi radius R_z/R_ρ) to the trap aspect ratio $\lambda_0 \equiv (\omega_\rho/\omega_z)$, and using the now standard relation

$$\Omega/\omega_\rho = \sqrt{(1 - (\lambda/\lambda_0)^2)} \ . \tag{2.2}$$

2.2 Rounding out the trap

As noted in the previous section, intrinsic vortex nucleation requires that the trap's ellipticity in the horizontal plane be less than 0.001, no small feat. Achieving this degree of roundness is a difficult task and it is unlikely, given the current technique

of assembling magnetic coils by hand, that a trap this round could achieved by careful initial fabrication. It is interesting to note that, despite careful construction, the JILA Mark III TOP trap has a natural 0.03 ellipticity when in the cigar configuration. While this asymmetry is roughly a factor of two better than competing Ioffe-Pritchard trap designs it is, of course, much too large to perform intrinsic nucleation of vortices. The glory of the TOP trap is that the rotating bias field does a great deal to define the trap's horizontal ellipticity and that by simply varying the amplitude of the bias field as it rotates, one can create a highly elliptical trap or, alternatively, suppress an existing anisotropy by more than an order of magnitude. Distorting the rotating bias field of the TOP trap is by no means a new technique and early discussion of it can be found in Jason Ensher's thesis [57]. Here I will limit my discussion to distortion of the TOP field as it applies to rounding of the trap for vortex generation.

Distortion of the top field can easily be done by adding together two oppositely-rotating, circular, bias fields to form an elliptical, rotating, bias field[1] . To clarify, by circular and elliptical I am referring to the shape carved out by the bias field vector as it does a complete rotation. It is convenient to refer to these two oppositely-rotating fields as Top2 and Ellipsifier. This historical designation refers to the hardware channels that provide each field. Generally, Top2 provides the unperturbed, circular field to which the Ellipsifier is generally added to provide the distortion. More precisely one can describe the rotating bias field of the Top2 channel as

$$B_{TOP} = a\ sin(\nu t)\hat{i} + a\ cos(\nu t)\hat{j}\ . \tag{2.3}$$

Here $\hat{i}$ and $\hat{j}$ can be thought of as the axes of the top coils (i.e. North-South and East-West). Here I have assumed that the field amplitude a is balanced along both

[1] It should be noted that the TOP box that switches between TOP channels allows for independent adjustment of amplitude of the signal sent to each pair of TOP coils as well as adjustment of the phase between them. In principle this analog adjustment could achieve the same effect as adding a counter-rotating bias field. NO ONE SHOULD EVER TRY THIS! These adjustments are far too sensitive for this work and settings are not easily reproduced. I mention this because one could easily, in thirty seconds, unround the trap to the point from which it would take a week to recover.

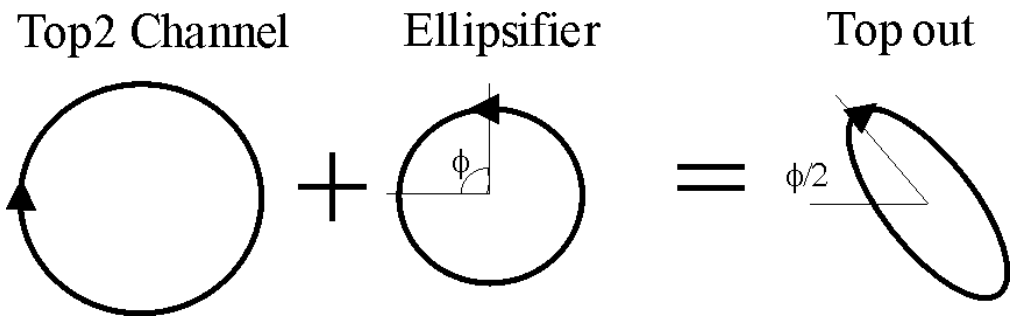

Figure 2.2: Addition of TOP fields forming an ellipse. The major axis of the ellipse is defined by half the phase angle between the top channel and the ellipsifier channel.

axes. In reality, this is probably not perfectly true. For the experiments presented in this thesis the bias field rotation frequency, ν, is 1800 Hz. We can then add a counter-rotating, Ellipsifier field such that the total bias field has the form

$$B_{TOP} = a\ (sin(\nu t) + \varepsilon\ sin(\nu t + \phi))\hat{i} + a\ (cos(\nu t) - \varepsilon\ cos(\nu t + \phi))\hat{j}\ . \tag{2.4}$$

Here ε is just the ratio of the magnetic field amplitude of the Top2 channel to the magnetic field amplitude of the Ellipsifier channel. The effect of increasing ε on the bias field is shown in figure 2.3. Here I have only considered the case $0 \leq \varepsilon \leq 1$. For $\varepsilon > 1$ the bias field asymmetry and orientation can be easily determined by noting that, for most purposes, there is no fundamental distinction between the Top2 and Ellipsifier channels and ε can also be thought of as the ratio of the Ellipsifier channel to the Top2 channel. To clarify, if the Top2 channel has half the amplitude of the Ellipsifier channel this will yield an elliptical bias field with the same orientation and ellipticity as when the Ellipsifier channel has half the amplitude of the Top2 channel. The only difference is the rotational direction of the final bias field which can usually be ignored.

The shape of the rotating bias field is of course not the whole story as noted in section 6.2.4 of Jason Ensher's thesis [57]. Ultimately the ellipticity of the TOP trap is determined by the interaction of the rotating bias field with the quadrupole gradient and with gravity. Thus the final ellipticity of the trap can vary dramatically between traps. As noted by Ensher this cannot be described analytically except for very small

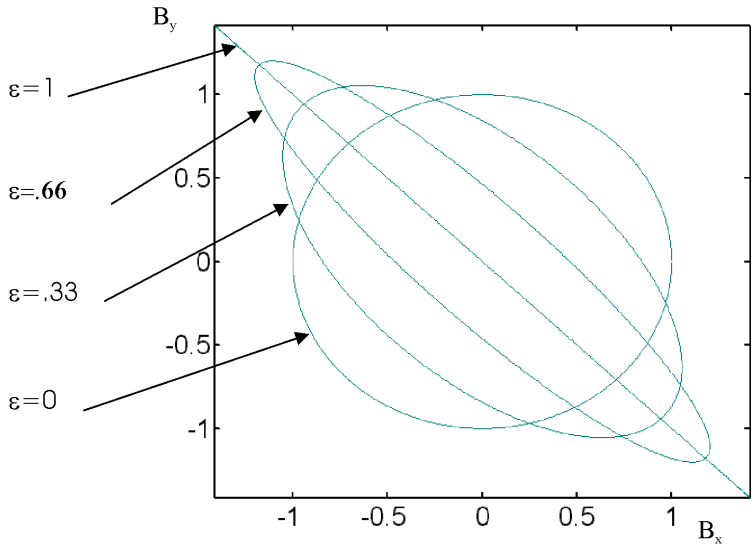

Figure 2.3: Plot of equation [2.4] demonstrating the effect of adding counter-rotating bias fields to form an elliptical bias field. In all cases the phase angle between counter-rotating bias fields is $\phi = 90^0$. Elliptical bias fields are plotted for a range of ε, the ratio of the strength of the two counter rotating fields.

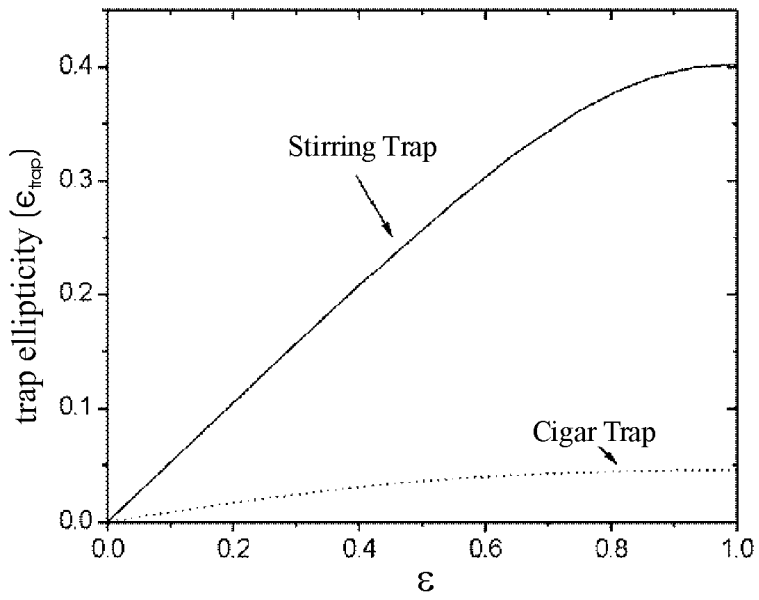

Figure 2.4: Effect on the calculated trap ellipticity of the rotating bias field distortion. The larger anharmonicities of the cigar trap make the trap ellipticity much waeker for the same ε.

eccentricities, which is not really the regime we are interested in. One can of course model this numerically (see appendix A for an outline of this process), the results of which have been plotted in figure 2.4 for the stirring trap[2] ($\{\omega_\rho, \omega_z\} = 2\pi\{7, 13\}$Hz) and the cigar trap ($\{\omega_\rho, \omega_z\} = 2\pi\{8.3, 5.3\}$Hz). The higher magnetic field gradients of the stirring trap (58 Gauss/cm vs. 32 Gauss/cm) allow for a much larger elliptical distortion.

In looking at figure 2.4 one can begin to understand the strategy for exciting vortices. The stirring trap provides a high ellipticity which allows for stronger coupling to rotational modes of the thermal cloud. On the other hand, the relatively weak dependance of ellipticity on ε in the cigar trap allows us to cancel out the natural ellipticity of this trap to a very high precision without being overly sensitive to drift in the strength of the elipsifier field. This is of course not the exact natural order of things as the cigar trap was actually chosen to facilitate one-dimensional evaporation.

While it is clear that these traps have the ability to shim away a few percent asymmetry with an elliptical bias field, it is a somewhat more complicated issue to perform the shimming at the level of 0.001 ellipticity that is required for evaporative spin up of the condensate. Worse still we have a two-dimensional parameter space (phase and amplitude of the counter-rotating field). To "round out the trap" we have developed several techniques that are essentially a means to measure the unroundness of the trap so that we may iteratively adjust the orientation and amplitude of the bias field distortion to slowly correct for the natural asymmetry. These three methods can be divide into coarse, intermediate, and fine tuning techniques.

Coarse measurement of the trap ellipticity are made by performing horizontal beat measurements. To perform beat measurements we jump the North-South and/or the East-West shim coils to induce condensate slosh in the horizontal plane of the trap. When a condensate sloshes in an elliptical trap the slosh frequency is determined by the

[2] trap frequencies cited are for the case of radial symmetry or $\varepsilon = 0$

eigenfrequencies of the major and minor axes of the trap. Initial motion not directly along one of these eigen axes will result in a beating between the two frequencies as the condensate motion moves about the major axis in a manner shown in figure 2.5(a). This beat frequency (ω_{beat}) is, of course, at the difference of the trap frequencies along the major and minor axes of the trap (ω_+ and ω_-). In the limit that the trap is nearly round one can write a convenient version of equation 2.1,

$$\epsilon_{trap} \simeq \frac{\omega_+ - \omega_-}{\omega_\rho} = \frac{\omega_{beat}}{\omega_\rho} \ . \tag{2.5}$$

Here as before ω_ρ is the average radial trap frequency. Thus, by lowering the beat frequency one can round out the trap. The advantage of this technique is that it will work for very large ϵ_{trap}. Beat measurements can be resolved as long as ω_{beat} is at least 3-4 times smaller than ω_ρ which is nearly always the case. The challenge and ultimately the limitation in this technique is measuring the beating between the two axes.

The lifeblood of beat measurements is nondestructive imaging [58, 59, 54], which allows us to measure the beat frequency in a single shot. Considering the iterative nature of bias field tuning we would be sunk without it. The simplest nondestructive method for this measurement is streak mode or movie type imaging. Here most of the CCD array on the camera is masked off except for a small area at the bottom in which the condensate image is centered. Once the slosh is excited the CCD is scrolled slowly upward as the condensate is imaged. With large probe detunings and low probe powers one can image the condensate motion for as long as 20 seconds before atom loss destroys the signal.

As the beating occurs, the condensate motion goes from linear motion along the initial axis of excitation to circular motion and then back to linear motion, along an axis mirrored across the major axis of the trap, as is depicted in figure 2.5(a). If the imaging axis is oriented along the initial axis of linear motion then the beating appears as narrow and wide waists in the streak image (see figure 2.5(b)) and the frequency can be easily

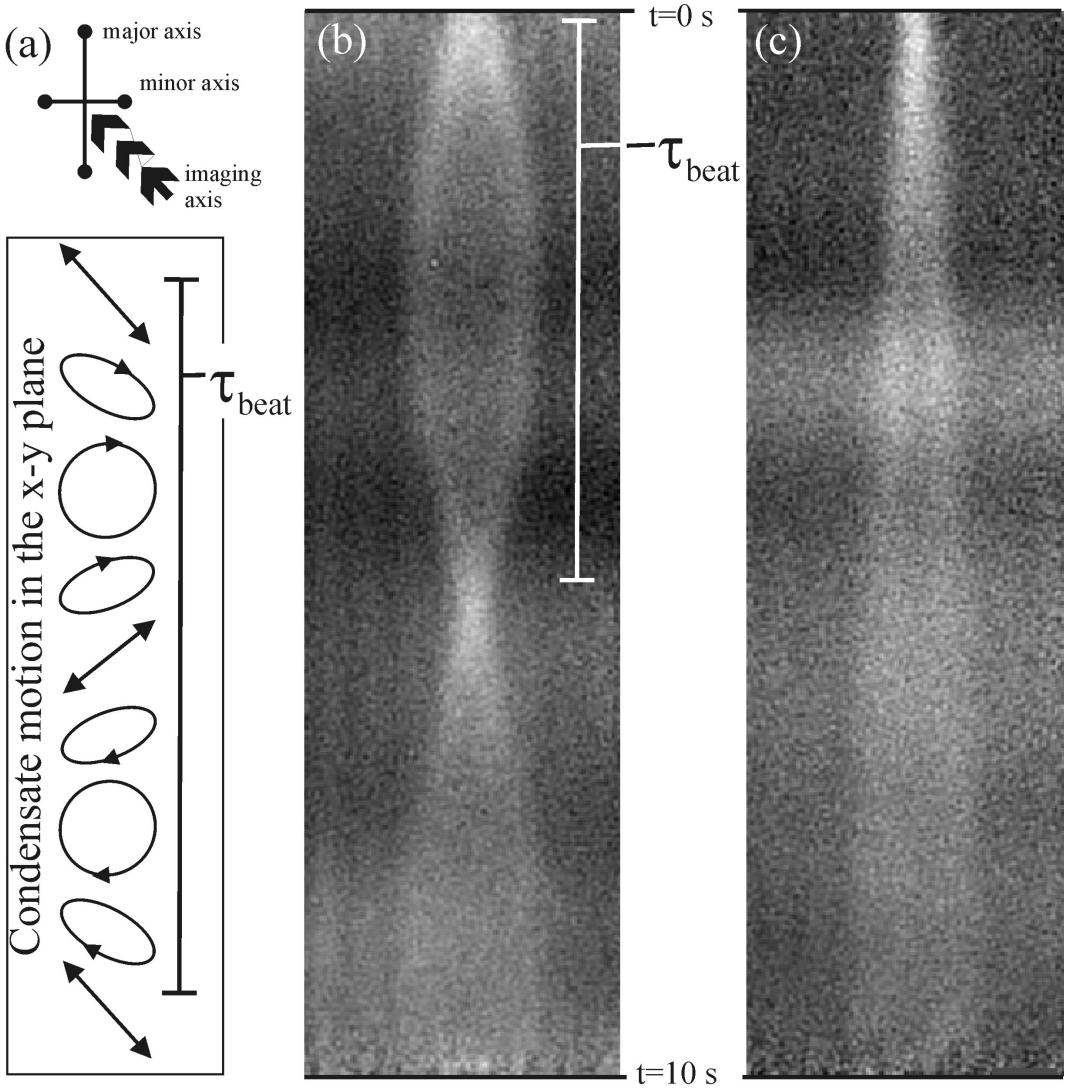

Figure 2.5: Beat measurements in the stirring trap. Image (a) shows the layout of the experiment and oscillation pattern of a sloshing condensate as it beats between the major and minor axis. The natural anisotropy of the trap seems to be such that major and minor axis of the trap are 45^0 from the imaging axis unless a highly elliptical top field is applied to move them away from this orientation. When the condensate oscillation is along the imaging axis we see a small waist in the streak image such as we do at the top of (b) and (c). Image (b) shows a double oscillation where τ_{beat} can be measured from the time between the two waists. Image (c) demonstrates the limit of this method. Here we can only measure roughly a half cycle and can only place an upper limit on ϵ_{trap}. The interrogation time can be increased to extend the range but noise quickly becomes a problem. One can already begin to see loss of contrast due to the atom loss and charge build up on the CCD.

measured given the scroll rate of the camera. The narrow waists are generally the most convenient way to measure the oscillation period ($\tau_{beat} = 2\pi/\omega_{beat}$) and the observed narrowness/sharpness of these small waists improves significantly when the initial slosh motion is precisely along the imaging axis. By carefully tuning the jumping of the shim coils one can dramatically increase the visibility of these waists. The width of the widest sections is dictated by the initial slosh amplitude and, more importantly, increases as the angle between the initial slosh direction to the major axis of the trap approaches 45^o. Thus, with careful observation the width of the wide sections can convey some information about movement of the major axis as one tries to round the trap. This also presents a potential problem since the width of the wide sections decreases as the angle of the initial slosh direction approaches the major or minor axis, and if this angle ever goes to zero the excitation is along an eigen axis and no beating occurs at all. We are somewhat blessed in that the natural eigen axes of the magnetic trap tend to be close to the axes of the TOP coils and 45^0 from the imaging axis so this zero angle situation almost never occurs while rounding the trap. Nonetheless, future grad students are advised to consider this point if their beat measurement is behaving funny.

The limitation of the beat measurement lies in the longest τ_{beat} one can observe. If one assumes that half an oscillation, like the one in figure 2.5(c), is the minimum oscillation period one can observe and still determine a τ_{beat}, then the lowest ω_{beat} measurable is roughly $2\pi/40$ seconds. Using this beat frequency in equation 2.5 and an ω_ρ of $2\pi \times 7$ Hz yields an ϵ_{trap} of 0.003. Thus beat measurements have the sensitivity to bring us close to the desired ellipticity. In the stirring trap, this technique is completely adequate since the requirements on trap roundness are greatly reduced due to the relatively small amount of time a rotating thermal cloud spends there. Unfortunately the same cannot be said for the cigar trap. The problem here is two-fold. As previously noted, the requirements on ϵ_{trap} in the cigar trap are somewhat higher due to the need to sustain rotation for a 100 s evaporation. In addition, beat measurements

are considerably less effective in the cigar trap. While streak mode measurements can be extended as long as 20 seconds in both the cigar and stirring trap, heating from slosh that occurs only in the cigar trap limits this interrogation time to at most 8-10 seconds, thus limiting the sensitivity of this method to $\epsilon_{trap} \approx 0.007$. While this is an important first step, additional techniques are clearly necessary.

To further round out the trap the angular momentum life time of the cloud can be used as a diagnostic for ϵ_{trap}. Guery-Odelin [60] has theoretically demonstrated that a rotating thermal cloud placed in an elliptical trap will spin down with a time constant of

$$t_{down} \approx 1/(2\epsilon_{trap}^2 \omega_\rho^2 \tau). \tag{2.6}$$

Here τ is the collision rate (roughly 1 Hz for data presented in this chapter) [3] . Thus by measuring the rotation decay in the thermal cloud one can continue to optimize trap roundness.

There are a few complications in this method associated with the switching of traps. The stirring trap is used to provide the initial rotation but we are interested in studying the cigar trap so the cloud must be transferred. The ramp to the cigar trap is not completely adiabatic and the thermal cloud under goes a few seconds of rethermalization. This rethermalization complicates the aspect ratio measurements made within the first few seconds after the ramp. In figure 2.6 this effect is clearly visible. Here the ramp to the cigar is completed a $t = 0$ and the black squares show the change in aspect ratio of a non-rotating cloud due to this rethermalization. When determining decay rates this rethermalization can be accounted for with a double exponential decay function none the less the rethermalization time constant limits the fastest decay one can hope to measure.

While the many-point lifetime measurements in figure 2.6 are a convenient way

[3] Equation 2.6 also assumes a relatively small ellipticity. As detailed in Ref. [60] this implies that $\epsilon_{trap} \ll 1/(4\omega_\rho \tau) \approx 0.03$ which is generally the case at this stage in the rounding process, but not universally true.

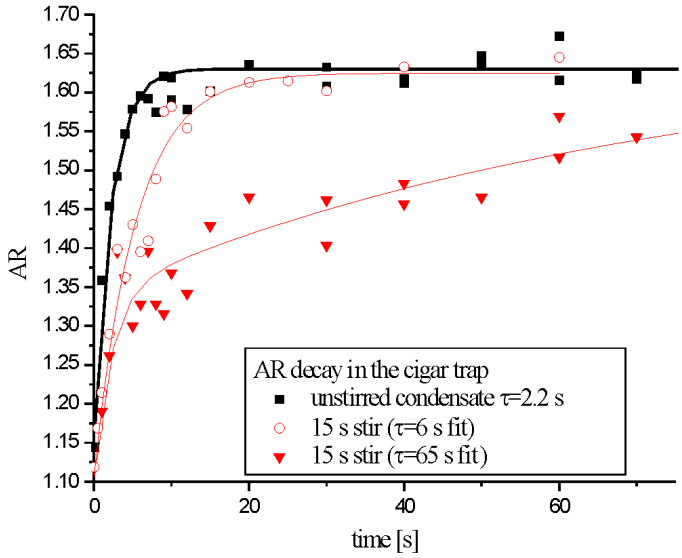

Figure 2.6: Thermal could aspect ratio decay rate in the cigar trap. Red circles and red triangles show the rotation decay in a trap with $\epsilon_{trap} = 0.03$ and $\epsilon_{trap} = 0.01$ respectively. Black squares are taken using a nonrotating cloud and show the effect of rethermalization to the cigar trap. Rotation decay time constants are found by first fitting the static cloud with a single exponential decay (black line) and then fitting the rotating cases with a double exponential where the first exponential is constrained to match the static case. Note that in the case $\epsilon_{trap} = 0.03$, rotation decay is nearly indistinguishable from rethermalization. It is this background noise from rethermalization that limits the maximum ϵ_{trap} one can measure using this method.

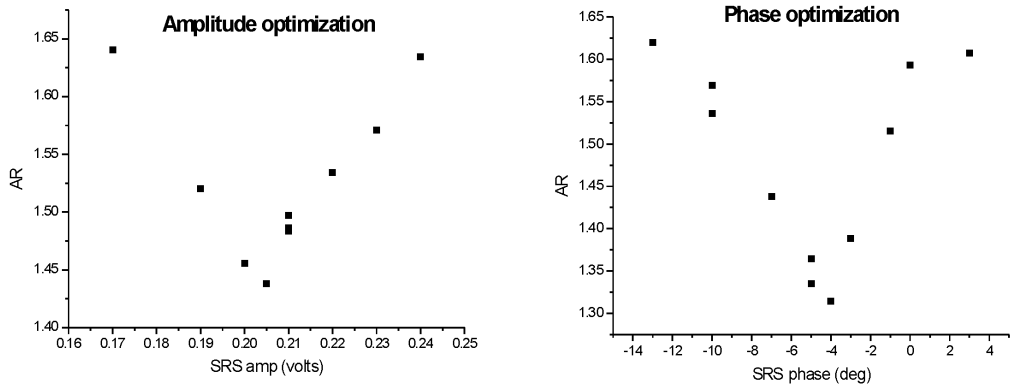

Figure 2.7: Examples of single point trap rounding measurements. These measurements can be performed with a thermal cloud at higher ϵ_{trap}'s or, when the system is sufficiently round to generate a rotating condensate, one can use condensed atoms. SRSamp is the experimental unit for the amplitude of the counter-rotating bias field. SRSphase is the phase, in degrees, between the rotating and counter-rotating bias fields.

to understand rotation decay, they are far too time consuming for the trap rounding procedure. If one is willing to forgo quantitative knowledge of ϵ_{trap}, trap rounding can be performed with a single point measurement by measuring the cloud aspect ratio after 10 or 20 seconds in the trap. Figure 2.7 shows such an effort as the amplitude of the counter rotating field is optimized and then the phase. Performing each of these optimizations twice is generally sufficient to round out the trap for the first time.

Finally, once the cigar trap is round, the roundness can be maintained simply by evaporating past Tc and optimizing on the condensate aspect ratio after evaporation in the same manner as one would with the single point thermal cloud measurements. While this yields no quantitative information about ϵ_{trap} it is certainly the most sensitive test of roundness and the most convenient to perform. Typically one can achieve condensate aspect ratios of 0.5 or lower using in this final step.

2.3 Anti-trapped expansion [1]

The clouds studied in this thesis typically contain between 1-300 vortices, each of which is too small to be observed in-trap but can be seen after expansion of the cloud. Our expansion technique is unusual enough to warrant a description. For the experiments presented here and elsewhere, we need a large radial expansion to make sure that the vortex cores are large compared to our imaging resolution. Additionally we need to suppress the axial expansion in order to preserve certain length scales in the condensate as discussed later in this section. Clearly, given our low and nearly isotropic trap frequencies, the usual expansion technique of shutting off the magnetic field and dropping the cloud would not meet such requirements. The solution, which has been demonstrated by other groups [61], is to perform an anti-trapped expansion. Rather than simply shutting off the trapping potential, we invert the trap in the radial direction so that the cloud is actively pulled apart. Simultaneously, the magnetic field gradient in the vertical direction is used to support against gravity.

The expansion is achieved in several steps that take place in rapid succession. First we employ a microwave adiabatic rapid passage technique (ARP) to transfer the atoms from the weak-field seeking $|F = 1, m_F = -1\rangle$ state to the strong-field seeking $|F = 2, m_F = -1\rangle$ state[4] . The microwave field employed is powerful enough to perform the transfer in 10μs but, as will be discussed shortly, we often take as long as 300μs for this transfer. After transfer to the anti-trapped state, the cloud still sits in its original position below the quadrupole zero, which means that both gravity and the magnetic field are acting to pull it downward. To counter this force a uniform vertical magnetic field is added to pull the quadrupole zero below the condensate so that the magnetic field gradient again cancels gravity. The field is applied within $10\mu s$, fast compared to relevant time scales. In this manner the cloud is again supported against gravity. To reduce curvature in the z direction, the TOP trap's rotating bias field is turned off leaving only the linear magnetic gradient of the quadrupole field. This gradient is tuned slightly to cancel gravity. Because the condensate is vertically displaced from the quadrupole center ($\sim 800\,\mu$m) the axial quadrupole field acts as a bias field for the radial gradient. Thus for radial displacements from the center, that are less then the sag distance, the radial anti-trapping potential is well approximated as an inverse parabola.

Using this technique, we are able to radially expand the cloud by more than a factor of 10 while, at the same time, seeing less than a factor of two axial expansion. Unfortunately even this much axial expansion is unacceptable in some cases. In the limit of adiabatic expansion, this factor of two decrease in condensate density would lead to an additional $\sqrt{2}$ increase in healing length during expansion. Thus, features that scale with healing length, such as vortex core radius in the slow rotation limit, would become distorted. The effect of axial expansion on vortex size was first noted by

[4] We also investigated transferring to the strong-field seeking $|F = 2, m_F = -2\rangle$ state used by [61] but found it unsatisfactory for our trap. The larger magnetic moment of this state made us more sensitive to bias field drift when cancelling gravity, while the nearly vertical magnetic field orientation in the cigar trap makes efficient transfer to the $|F = 2, m_F = -1\rangle$ much easier.

Dalfovo and Modugno [62].

To suppress the axial expansion, we give the condensate an initial inward or compressional impulse along the axial direction. This is done by slowing down the rate at which we transfer the atoms into the anti-trapped state. The ramping direction of the ARP is such that it transfers atoms at the top of the cloud first and moves down through the cloud at a linear rate. These upper atoms are then pulled downward with a force of 2g (gravity plus magnetic potential), thus giving them an initial inward impulse. Finally, the ARP sweep passes resonantly through the lowest atoms in the cloud: they, too, feel a downward acceleration but the axial magnetic field gradient is reversed before they can accumulate much downward velocity. On average the cloud experiences a downward impulse, but also an axial inward impulse. Normally the ARP happens much too fast for the effect to be observable but when the transfer time is slowed to $200 - 300\mu$s the effect is enough to cause the cloud to compress axially by 10-40% for the first quarter of the radial expansion duration. The cloud then expands back to its original axial size by the end of the radial expansion.

Despite our best efforts to null out axial expansion, we observe that the cloud experiences somewhere between 20% axial compression to 20% axial expansion at the time of the image, which should be, at most, a 10% systematic error on measured vortex core radius. The overall effect of axial expansion can be seen in figure 2.8, where image (b) and (c) are similar condensates and differ primarily in that (c) has undergone a factor of 3 in axial expansion while in (b) axial expansion has been suppressed. The effect on the vortex core size is clearly visible.

Since almost all of the data presented in this thesis is extracted from images acquired after the condensate expands, it is worth discussing the effect of radial expansion on the density structure in the cloud. In the Thomas-Fermi limit, it is easy to show that the anti-trapped expansion in a parabolic trap, combined with the mean-field and centrifugally driven expansion of the rotating cloud, leads to a simple scaling of the

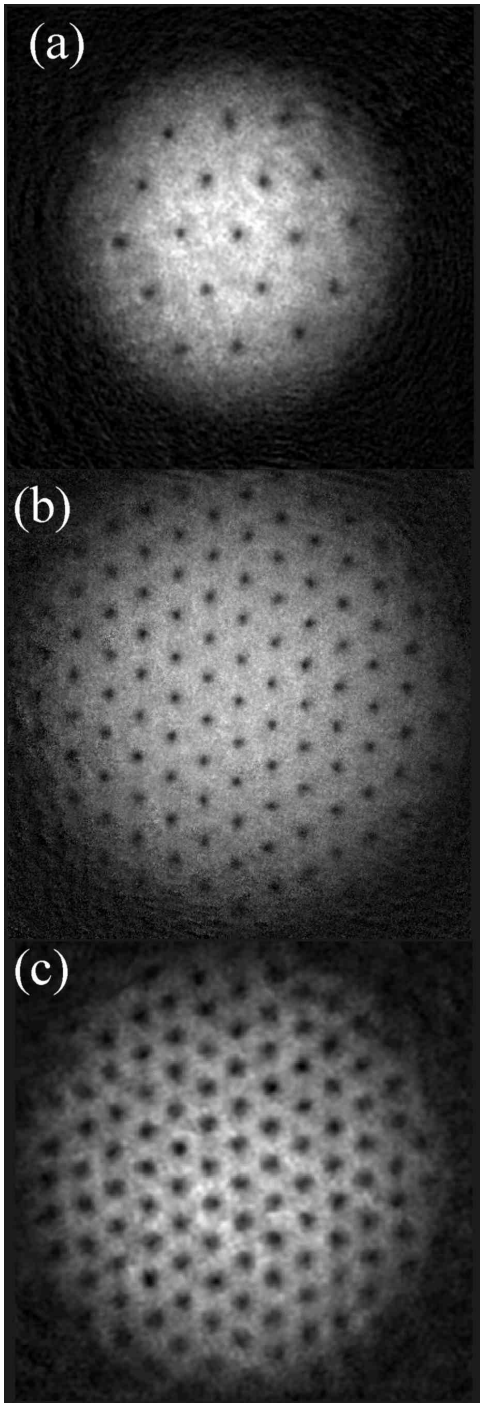

Figure 2.8: Examples of the condensates used in the experiment viewed after expansion. Image (a) is a slowly rotating condensate. Images (b) and (c) are of rapidly-rotating condensates with similar in-trap conditions. They differ only in that (c) was allowed to expand axially during the anti-trapped expansion. The effect on the vortex core size is visible by eye.

linear size [63] of the smoothed, inverted-parabolic density envelope. As the condensate radius, R_ρ, increases, what happens to the vortex-core size? There are two limits that are easy to understand. In a purely 2D expansion (in which the axial size remains constant), the density at any spot in the condensate comoving with the expansion goes as $1/R_\rho^2$, and the local healing length ξ then increases over time linearly with the increase in R_ρ. In equilibrium, the vortex core size scales linearly with ξ. The time scale for the vortex core size to adjust is given by $\hbar/\mu$ where μ is the chemical potential. In the limit (which holds early in the expansion process) where the fractional change in R_ρ is small in a time $\hbar/\mu$, the vortex core can adiabatically adjust to the increase in ξ, and the ratio of the core-size to R_ρ should remain fixed as the cloud expands.

In the opposite limit, which applies when R_ρ expands very rapidly compared to $\hbar/\mu$, the inverted parabolic potential dominates the dynamics, and every point in the cloud expands radially outward at a rate proportional to its distance from the cloud center. In this limit, the "fabric of the universe" is simply stretched outward, and all density features, including vortex core size expand at the same fractional rate. Again, the ratio of core-size to R_ρ should remain fixed.

So in the two extreme limits, the ratio of vortex core size to R_ρ (and other density features, such as nearest-neighbor vortex separation) remains fixed. It is reasonable then to assume that this behavior will be true in general for the intermediate regime between the two expansion rates. Extensive numerical simulations were performed to validate this assumption.

Once expanded, the cloud is imaged along the vertical direction, and data is extracted by fitting the integrated (along the line of sight) condensate density profile with a Thomas-Fermi distribution. We then subtract this fit from the image and easily fit the remaining vortex-core residuals with individual 2D Gaussian profiles to determine the core centers and radii. For the purpose of this section the vortex radius r_v is defined to be the RMS radius of the 2D Gaussian that we fit to the core. For clarification, the

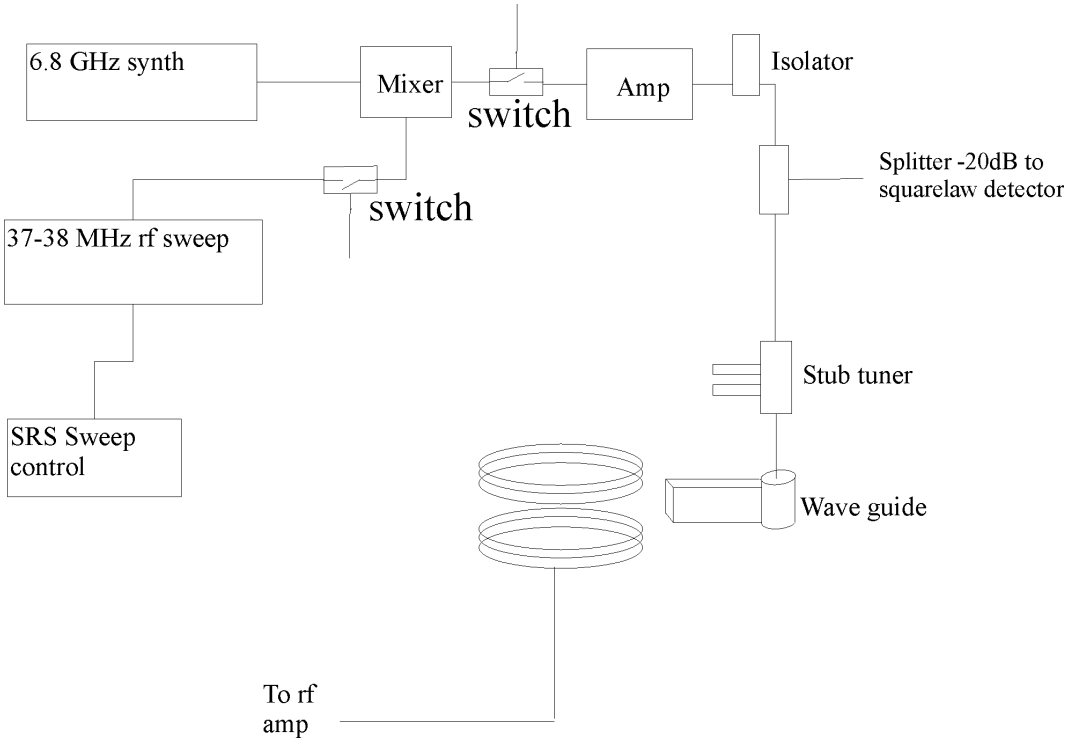

Figure 2.9: The microwave frequency chain has evolved somewhat since originally presented by Michael Matthews [59]. In order to perform the ARP, an image reject mixer has been inserted before the microwave amplifier. This mixer allows us to sweep the microwave frequency using more convenient rf technology. It also generates an accounting hazard since it has the effect of adding $\sim 35 - 38$ MHz to the microwave frequency depending on settings. This means that microwave values recorded in lab books prior to 9/02 need to be similarly adjusted. Other alterations to the experiment include a stub tuner to improve coupling to the wave guide, a new solid state amplifier, and SemFlex cabling between all components. This last alteration in particular has greatly reduced the sensitivity to bumps and slight movements of the components.

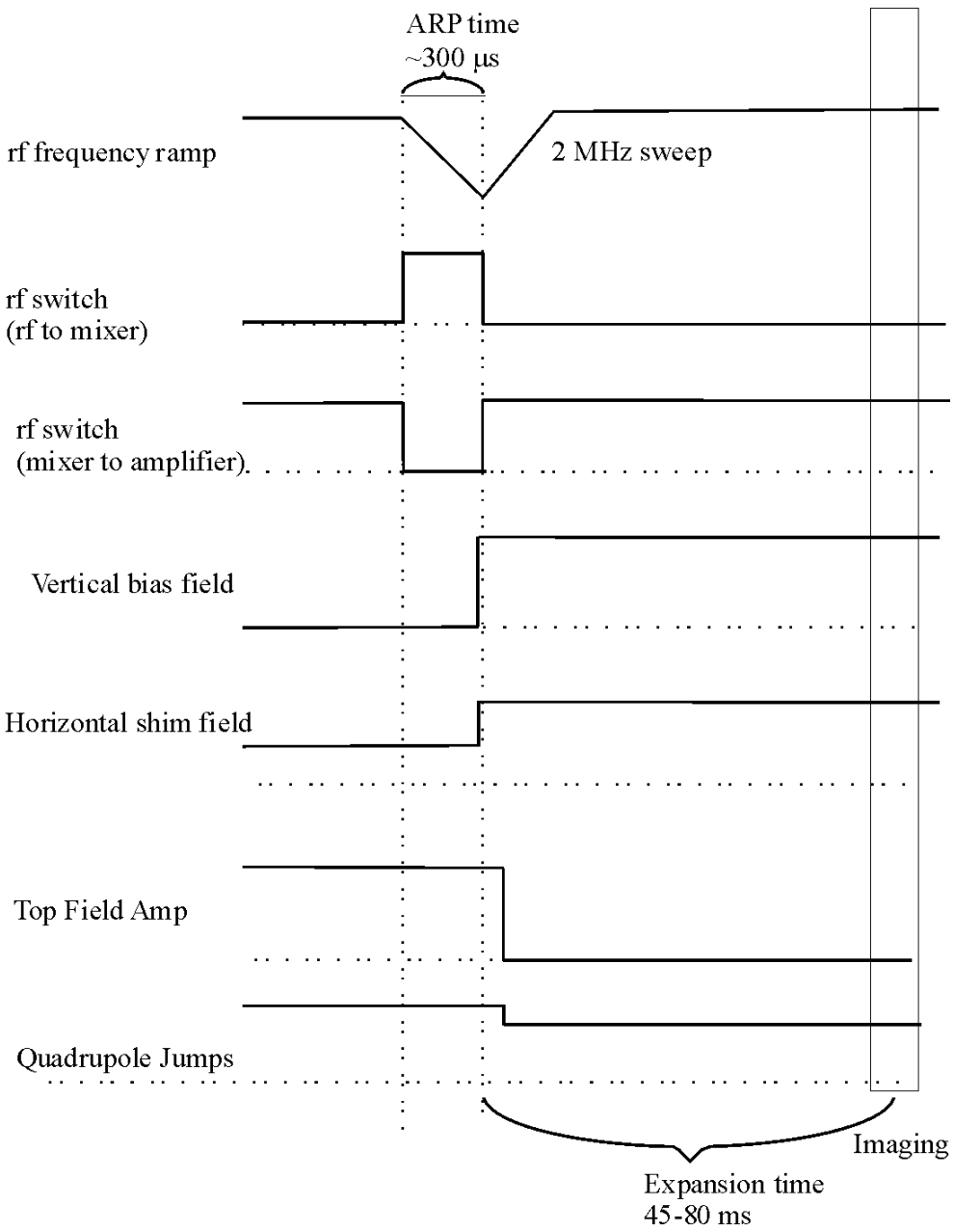

Figure 2.10: Timing sequence for the ARP (not to scale). The rf frequency ramp can be performed in as little as 10 μs, but is generally done in 300 μs to suppress axial expansion. The rf to the atoms is controlled by two switches, rf-mixer and mixer-amplifier, which have opposite logic. These switches are not actually redundant since the mixer-amplifier switch kills any leaks from the mixer and the mixer-rf switch helps to protect the mixer from the near threshold power levels that it would otherwise see all the time. The vertical bias field is triggered 100 μs before the end of the ARP to account for delays in the electronics. Horizontal shims are jumped to correct for the, imperfectly aligned, vertical bias field. It is important that the vertical bias go on very quickly after the ARP because the atoms feel a 2g downward acceleration prior to this field jump. The TOP fields are shut off a 5 ms after the ARP to limit field curvature in the vertical direction. A concurrent 1-3 bit change in the quadrupole voltage is done to roughly maintain the trap center.

RMS radius of a 2D Gaussian would be 0.60 times its FWHM. Condensate and vortex fits can be performed iteratively to reduce error.

Before each expanded image we also take a horizontal, nondestructive, in-trap image of the cloud immediately before expansion. From this image, rotation rate and atom number are determined. Length scales in the expanded cloud can be scaled back to in-trap values by dividing by the radial expansion factor, defined as $R_\rho(expanded)/R_\rho(in-trap)$.

2.4 Poking, prodding, cutting and blasting beams

Finally, I would like to discuss some of the atom removal and prodding techniques. My aim here is not to provide a comprehensive description of these techniques, as they are still in a state of flux and will likely be out dated for most readers of this thesis. Rather, it is my hope to provide a rough description of the apparatus and a context for the experiments detailed later in this thesis.

The "poking beam", as it is often called, is meant to perturb a very localized section of the condensate in a manner that is axially symmetric. This perturbation is accomplished by bringing a beam up through the cell along the MOT beam path and focusing it onto the condensate so that the $1/e^2$ beam waist is between 10 and 100 μm depending on the application. Uses of this beam path have included; pushing atoms away from the center of the cloud with a blue detuned beam to create shock waves [cite peter], drawing atoms into the center with a red detuned beam to excite Tkachenko modes, and selectively removing atoms near the condensate center to spin up the cloud to create giant vortices or excite Tkachenko modes.

Figure 2.11 depicts the beam path that enables us to do this. The poking setup has several noteworthy features. The fiber output coupler provides both a clean mode profile and beam pointing stability. Is is also convenient in that it allows for quick switching between 850 nm light for an attractive dipole potential and 780 nm light used

for atom removal. Using an FC junction in the middle of the fiber allows for quick switching at the acceptable cost of some power loss (loss varies but is always less than 50%). Unfortunately, the blue detuned 670 nm beam requires a separate fiber since the 850 nm fiber used for the other two beams supports both the zeroth and first order spatial modes at this higher frequency.

Following the output coupler is an adjustable telescope that expands the beam. Given the 12 cm lens that ultimately focuses the light onto the atoms, one needs at least a 2-4 mm beam waist after the telescope. Placing the second mirror on a translation stage makes it far easier to focus the beam in real time while monitoring it on the vertical imaging camera. The other advantage of this translation stage is that, when needed, a larger beam waist at the atoms can be quickly generated by misaligning the telescope. It is also conceivable to image complicated patterns onto the condensate by placing masks in the focus of the telescope.

The second critical alignment tool is the pico motor set. Mounted on the last mirror on the elevated platform these motors provide the micro-radian angle adjustments that are needed to not only hit the condensate but also center the beam on it. The combination of realtime adjustments using the vertical imaging camera and the fairly reproducible steps of the pico motors makes the otherwise daunting task of hitting the condensate with the focus of the laser easy. Due to space constraints, most of the set up is mounted on an elevated platform that sits, on 1 in. posts, about a 30 cm above the optics table. This elevated platform is surprisingly stable and both long and short term drifts were not a problem. However, this poking application is forgiving in nature however and it should be noted that use of the elevated platform was found unsuitable for optical lattices.

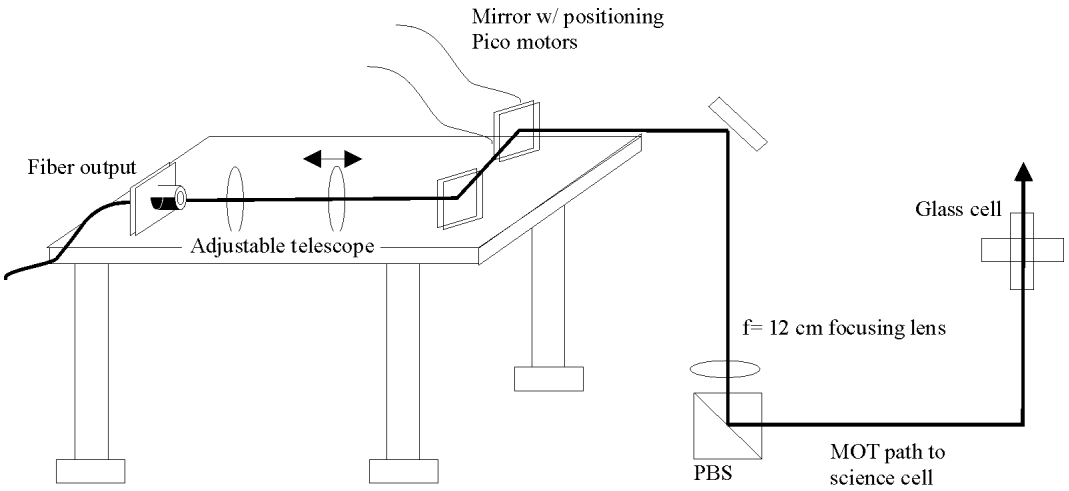

Figure 2.11: Poking beam setup. Optical fiber couples out into an adjustable telescope to allow for quick adjustments of the beam spot size at the atoms. Pico motors mounted on the steering mirror allow for fine tuning of the beam position across the condensate. A final 12 cm lens focuses the poking beam onto the condensate. Coupling to the MOT path is done using a polarizing beam splitter.

2.5 Other adjustments to JILA Mark III

As one can see, JILA Mark III has become increasingly and complex over the last few years as new functionality is added. The anti-trapped expansion technique and the vertical poking/blasting beam are just the latest in a long sequence of additions to the machine. The good news is that trapping laser upgrades and alterations have made the experiment somewhat simpler and much more robust. While a highly detailed description of these changes is probably unnecessary I will mention a few of them here if only to briefly discuss many of the lessons learned.

Arguably the most significant change has been to replace the science MOT laser with a master slave pair. The old setup (detailed in Jason Ensher's thesis [57]) was a particularly well stabilized ECDL made in the standard JILA design. While this laser was easily the best homemade laser I have worked with, it suffered from the fact that there was a long beam path from the laser to the MOT. Consequently, small tweaks to the grating or early mirrors could mean days of realignment, and replacing a burned out diode was an epic affair. In the new setup, a Vortex laser injects a 100 mW slave laser. This laser system is fiber coupled and then output coupled into the previous beam path just before the optical pumping AOM, thus leaving most of the beam path untouched. After building this system we realized that it offered several advantages some of which were unexpected.

As we had hoped, the fiber increased the pointing stability of the beam, leading to much less science MOT maintenance. Additionally, the fiber allows us to tweak the laser setup or replace a dead laser without altering the MOT alignment. Previously, the science MOT beam path was so temperamental that something as simple as a grating tweak could take a day to recover from and replacing a dead laser could take a week. With the fiber coupling we have been able to replace dead lasers within a few hours. An additional unforeseen advantage of the fiber is that the clean special profile of the

trapping light makes the MOT considerably less sensitive to small alignment changes and consequently much easier to align.

The effect of all this is best quantified anecdotally. With the old system beam drift and alignment problems would cause use to lose the ability to make a condensate roughly every two months and recovery time would be on the order of a week. With the current system, I don't believe drift has ever caused us to completely lose a condensate, and MOT alignment typically takes a day or two.

An additional advantage of the Vortex lasers is their temperature stability. It used to be that a two degree change in lab temperature would make it difficult, if not impossible, to make condensates. Generally the problem was a bad mode in the science MOT laser or the collection MOT laser (both of which were the standard JILA ECDL), and would manifest itself as poor science MOT loading or degradation of the molasses stage and a corresponding loss of condensates. After replacing both these systems with Vortex lasers we are able to accommodate 3^o C shifts in lab temperature, and still produce reasonable condensates.

We have also switched to using Vortex lasers for phase contrast imaging, an application for which they are ideally suited. The 70 GHz tuning range is excellent protection against the mode hops that plagued our system before, and being able to tune across the 6.8 GHz splitting of 87Rb is very practical when working with spinor condensates. Other groups have had trouble using Vortex lasers for absorption imaging due to the fact that mechanical noise (typically shutters) tends to broaden the line width of the laser. With phase contrast imaging we are typically detuned by a few hundred MHz so a few MHz change in the laser line is of no consequence.

I mention these changes primarily because I regret not making them sooner. The increased robustness of the experiment very quickly made up for the installation time in terms of hours spent on science, and, as a secondary issue, contributed favorably to the mental health of those of us in the lab.

2.6 Numerical studies

In the later part of this thesis it is useful to compare our experimental results to a numerically generated condensate wave function. These numerical studies are done by setting up an initial in-trap condensate wave function with a given atom number (N) and Ω on a 2048x2048 lattice and then relaxing this wave function by propagating the Gross-Pitaevskii equation in imaginary time. All work shown in §5.5 and §6.2 is done in 2D. Additionally a radially symmetric 3D simulation can be performed for a single vortex, as is done in §5.5 and in §6.3. Once the final wave function is found, we convert to an atom density profile which can be fit and analyzed in the same manner as the experimental data.

Chapter 3

Giant Vortices [2]

3.1 Introduction

In dilute gas Bose-Einstein condensates, vortex experiments have ranged from the study of individual or few vortices [20, 21, 22, 23] and vortex rings [64, 65] to the first creation of vortex lattices [66] and the study of systems containing large amounts of vorticity [24, 25]. In this chapter we begin the discussion of non-equilibrium vortex effects.

Using a refinement of our experimental technique, we are able to generate a giant vortex. I use the term "giant vortex" to denote a region, containing multiple units of vorticity, in which the density is completely suppressed such that the individual vortices are no longer discernible. Note that some authors reserve this term for higher order phase singularities. The possible existence of stable giant vortices under certain conditions like supersonic flow in potentials that have strong quartic terms has been theoretically predicted (Ref. [67, 68, 69, 19], see also Ref. [46]), and in Ref. [70] it is shown that a pinning potential can lead to stable multiquantum vortices. In our case, however, the giant vortex formation arises as a dynamic effect. Nevertheless the lifetime of our giant vortices can extend over many seconds, which we attribute to a stabilization of density features in a rapidly rotating condensate due to strong Coriolis forces. Previously, only short-lived regions containing a few phase singularities with suppressed density have been observed experimentally in Ref. [71] in the form of stripes

and in Ref. [51] as the result of topological vortex formation. The influence of Coriolis forces can also induce oscillations of the giant vortex core size in the early stages of its evolution.

3.2 Experiment

Experimental starting conditions are similar to the ones described in the previous chapter. We start with a cloud of condensed ^{87}Rb atoms in the $|F = 1, m_F = -1\rangle$ state, and held in the cigar trap with trap with frequencies $\{\omega_\rho, \omega_z\} = 2\pi\{8.3, 5.4\}$Hz. Cloud sizes are typically 3×10^6 atoms and we routinely achieve condensate rotation rates (Ω) of 95% of the radial trap frequency, with no detectable thermal cloud. These condensates typically contain 180 or more vortices as seen in figure 3.1(a) or figure 3.2(a). After careful optimization of the trap roundness and in the presence of a quasi 1-D rf-shield we are able to observe the BEC rotation for times exceeding 5 minutes. While we do lose atoms from the condensate over this time scale, the rotation rate remains at its initial value.

The evaporative spin-up mechanism discussed in §2.1 is limited because eventually all the uncondensed atoms will be removed or condensed during the quasi one-dimensional evaporation. However, the angular momentum per particle in the condensate can be further enhanced by selectively removing atoms with low angular momenta by a resonant, focused laser beam sent through the condensate on the axis of rotation. Selectivity is provided by having a beam width, at the focus, that is small compared to the condensate size. For experiments presented here the rotating BEC typically has a Thomas-Fermi radius of $66\mu m$ and the width of the laser beam is about $16\mu m$, stated here as the full width at half maximum (FWHM) of the Gaussian intensity profile. The frequency of the laser is tuned to the $F'' = 1 \rightarrow F' = 0$ transition of the D2 line, and the recoil from spontaneously scattered photons blasts atoms out of the condensate.

Using this new technique we are able to substantially increase the vorticity in

the BEC and can now routinely obtain condensates containing more than 250 vortices [figure 3.1(b)]. Since these vortex cores are too small to be imaged when the BEC is held in trap, the images in Figs. 3.1, 3.2, 3.3, and 3.7 are taken after having let the BEC expand. For this expansion an anti-trapped technique is used as detailed in §2.3. This technique allows us to expand the condensate to an adjustable diameter that can exceed 1.4 mm.

If the removal of central atoms is driven strongly enough, a giant vortex appears. The core is surrounded by a ring-shaped superflow. The circulation of this superflow is given by summing up all the "missing" phase singularities in the core and can assume very large values. Using the fact that for large amounts of circulation the rotation of the velocity field can be obtained classically, we determine that in some cases the BEC supports a ring-shaped superflow with a circulation of up to 60 quanta around the core. We can easily control the amount of this circulation by changing the intensity or the duration of the laser beam that removes atoms along the axis of rotation.

3.3 Giant vortex formation and condensate healing

In our experiment the formation of the giant vortex comes about in a sequence of very distinct stages as shown in figure 3.1. For this expansion image sequence a rapidly rotating BEC is first formed by our evaporative spin-up technique. Then the atom-removal laser is applied with a fixed power of 8 fW for a variable amount of time, followed by a 10 ms in-trap evolution time and a 45 ms expansion in the antitrapping configuration described above. During the atom removal an rf-shield is left on to constantly remove uncondensed atoms that tend to decelerate the condensate rotation. Figure 3.1(a) shows the result of only the evaporative spin-up. This particular condensate contains 180 vortices and has a Thomas-Fermi radius of $63.5\,\mu m$ when held in the trap. When the atom removal laser is applied for 14 s as in figure 3.1(b), the number of vortices is increased to 250 and the Thomas-Fermi radius to $71\,\mu m$. The rotation

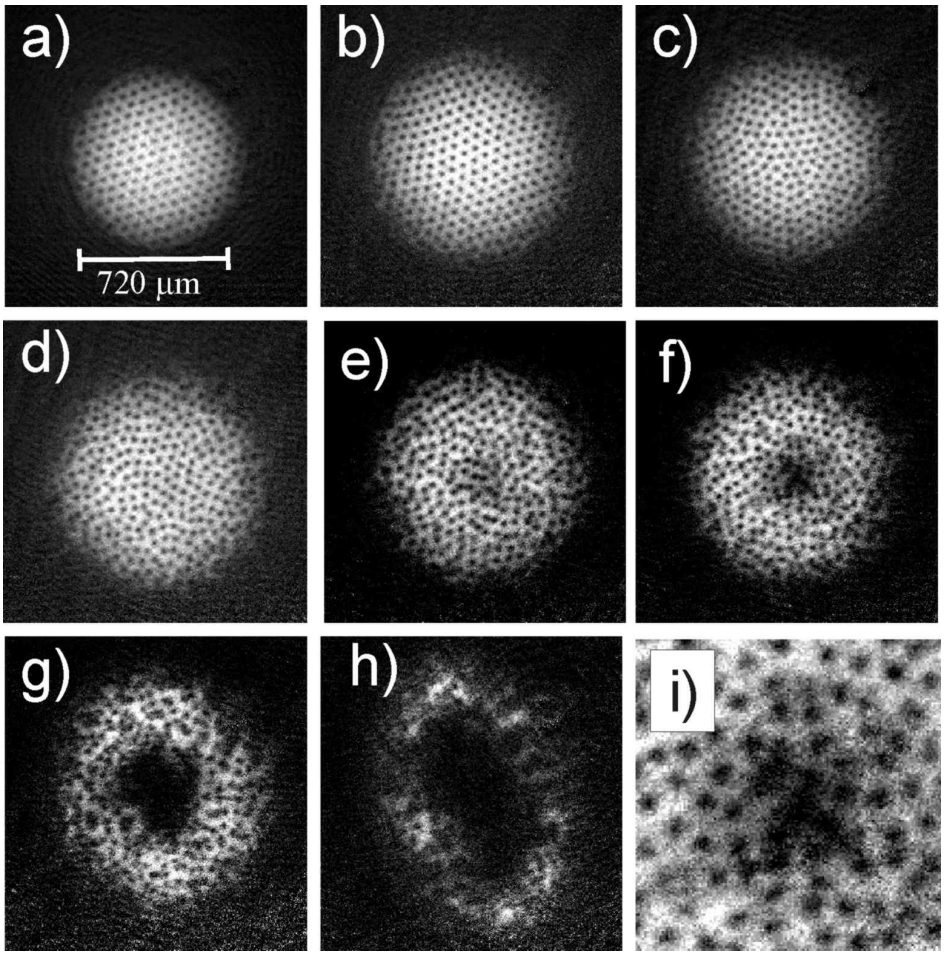

Figure 3.1: Different stages of giant vortex formation process. (a) Starting point: BEC after evaporative spin-up. (b)-(h) Laser shone onto BEC for (b) 14 s, (c) 15 s, (d) 20 s, (e) 22 s, (f) 23 s, (g) 40 s, (h) 70 s. Pictures are taken after 5.7-fold expansion of the BEC. Laser power is 8 fW. (i) Zoomed-in core region of (f).

rate, determined from sideview aspect-ratio images, has increased from $\Omega = 0.94\,\omega_\rho$ to $\Omega = 0.97\,\omega_\rho$. After atom removal times of 15 to 20 s, the vortex lattice becomes disordered [figure 3.1(c,d)], and the giant vortex core starts to develop in the center [figure 3.1(e,f)]. An enlarged view of the core region in this early stage of giant vortex core formation is seen in figure 3.1(i), which nicely demonstrates how the individual vortices in the center consolidate. For the larger removal times shown in Figs. 3.1(g) and (h), a clear elliptical deformation is observed. This deformation is due to $m = -2$ surface wave modes excited by residual static asymmetries of the trapping potential. As the condensate rotation rate approaches the trapping frequency of these $m = -2$ modes goes to zero [40] and are thus nearly resonantly driven by even a small asymmetry. We have verified this explanation by deliberately changing the roundness of the trapping potential and observing corresponding changes in the ellipticity and in the direction of the ellipse. If the trap roundness is not optimized, the ring-shaped superflow has a tendency to fragment into 5 to 8 blobs that continue to rotate around the core.

If the atom removal laser is applied only for a limited amount of time, the giant vortex will fill in and the vortices refreeze [72] into a well ordered lattice again after a sufficiently long evolution time. An example is shown in figure 3.2. Here, the starting point is the condensate in figure 3.2(a), containing 190 vortices and rotating at $\Omega = 0.95\,\omega_\rho$. A pulse from the atom removal laser creates the core seen in figure 3.2(b). Crudely assuming that, consistent with the observed atom removal of 35%, all atoms originally within a cylindrical volume of 0.4 times the Thomas-Fermi radius have been removed, we can perform an integral over the Thomas-Fermi density profile with a rigid-body-rotation velocity distribution and find that only 10% of the angular momentum has been removed. Since in equilibrium the total number of vortices should be linear in the average angular momentum per atom [45], we would expect that the original 190-vortex cloud should reequilibrate to form a cloud with 266 vortices, in good agreement with the value of 260 vortices observed in the reequilibrated cloud shown in figure 3.2(d).

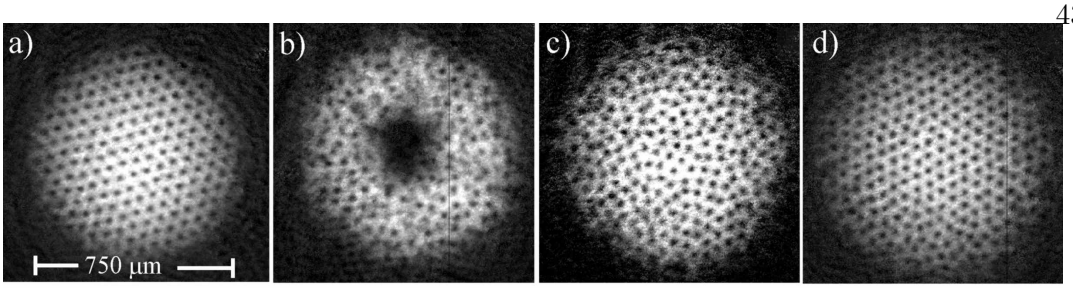

Figure 3.2: Lattice reforming after giant vortex formation. (a) BEC after evaporative spin-up. (b) Effect of a 60 fW, 2.5 s laser pulse. (c),(d) Same as (b), but additional 10 s (c) and 20 s (d) in-trap evolution time after end of laser pulse. Images taken after a sixfold expansion of the BEC.

In our case the formation of the giant vortex is not connected to a repulsive conservative optical potential produced by the central laser beam, but only due to the removal of atoms from the axis of rotation by spontaneous photon scattering. To prove this, we have varied the laser frequency over the range from -6 MHz to +6 MHz around the $F'' = 1 \rightarrow F' = 0$ resonance and in all cases have been able to generate a giant vortex.

In Ref. [67, 68, 69, 19] it is shown that quartic terms in the potential can lead to stable giant vortices. In our experiment, quartic terms are small and the giant vortex arises as a dynamical effect. We have calculated the term of the TOP trap potential that depends on the radial position as r^4. At the outer edge of the condensate this quartic term produces a correction to the potential on the order of 10^{-3}, compared to the effective r^2 term, even though the latter is much weakened by the centrifugal force. Moreover, our anharmonic terms have the wrong sign [67, 68, 69, 19] to generate stable giant vortices. Empirically, the refilling and refreezing we observe (figure 3.2) indicates that the giant vortex is not an equilibrium configuration but has instead only dynamical stability.

We suggest an intuitive, classical picture describing the formation as a dynamical effect: the removal of atoms from the center of the condensate produces a pressure

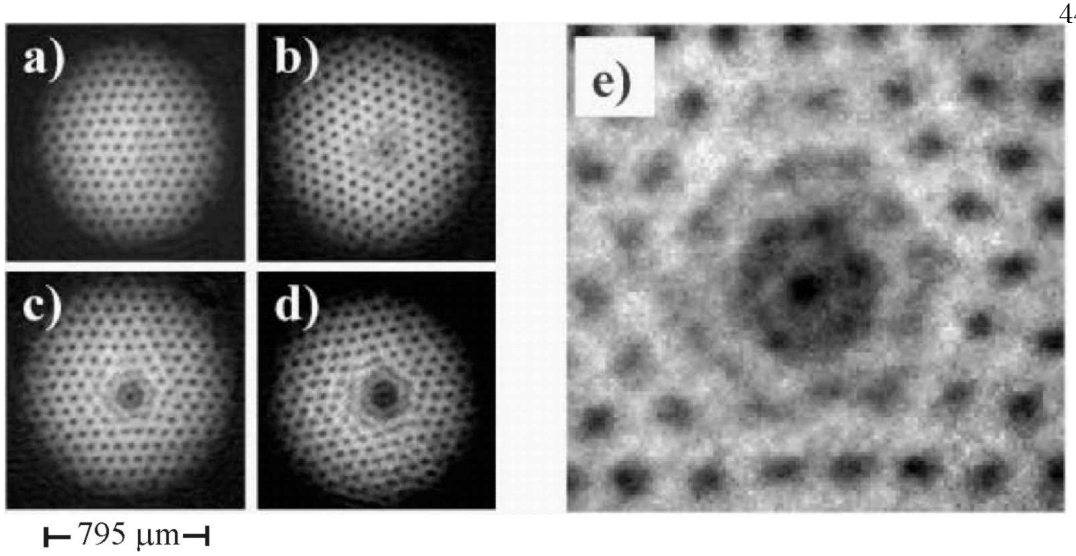

Figure 3.3: Core developing after a 5 ms short, 2.5 pW laser pulse. In-trap evolution time after end of pulse is (a) 0.5 ms, (b) 10.5 ms, (c) 20.5 ms, (d) 30.5 ms. Images taken after sixfold expansion of BEC. (e) Zoomed-in core region of (c).

gradient due to mean field energy that tries to drive atoms from the outer regions into the center, so as to close the hole. Due to Coriolis forces, however, atoms moving radially towards the center are deflected and assume a fast azimuthal motion around the core rather than filling the core, thus creating the giant vortex.

Some exotic features of the early stages of core formation are revealed when we apply only a very short, weak atom removal pulse and observe the subsequent evolution as in figure 3.3. Here, the atom removal laser has a power of 2.5 pW and a fixed pulse length of 5 ms. Its FWHM of 16 μm is approximately twice the lattice spacing, 7μm. By varying the delay time between the laser pulse and the expansion, we see (figure 3.3) that the core formation clearly lags behind the laser pulse. Figure 3.3(e) shows a zoomed-in view of the core region of figure 3.3(c). It is very interesting to observe that for these short, weak pulses the density depression appears to develop in discrete steps, and the step boundaries follow the hexagonal lattice pattern.

3.4 Giant vortex stability

When applying stronger laser pulses, we detect clear, damped oscillations of the core area as shown in figure 3.4. We study these oscillations by analyzing in-trap images taken after a variable evolution time between the end of the atom-removal pulse and the expansion, such as the ones shown in the inset of figure 3.4. The oscillation frequency depends on the initial conditions; for the case of figure 3.4 with initially 2.2×10^6 atoms at a rotation rate of $0.9\,\omega_\rho$ we obtain a frequency of $3.5\,\omega_\rho$. Decreasing the initial rotation rate of the condensate leads to faster core-oscillation frequencies and increases the amplitude of this oscillation; for condensate rotation rates below $\Omega = 0.9\,\omega_\rho$ in-trap images even show a near complete closure of the core, followed by the core opening again (see inset of figure 3.4). Presumably these oscillations arise when a sudden removal of atoms leaves forces from the density gradient and Coriolis forces initially out of equilibrium. The core oscillation is not observed to be related to an overall breathing mode of the condensate.

To study the dynamics, core size oscillations are measured for a range of condensate rotation rates. Figure 3.5 shows a plot of the measured oscillation frequencies as a function of the condensate rotation rate. A clear decrease of the oscillation frequency with increasing rotation rate is seen. Recently A. Fetter has developed analytic formulae, based on a variational Lagrangian, that describe the behavior seen in our experiment [73]. His results also imply that the parabolic trap and conservation of angular momentum, thus the influence of Coriolis forces, are governing the dynamics.

3.5 Giant vortex precession

In addition we can observe the precession [21] of an off-center giant vortex. For this, the atom removal laser is deliberately offset from the center of cloud rotation. The duration of the removal pulse is kept short (10 ms) in comparison to the initial

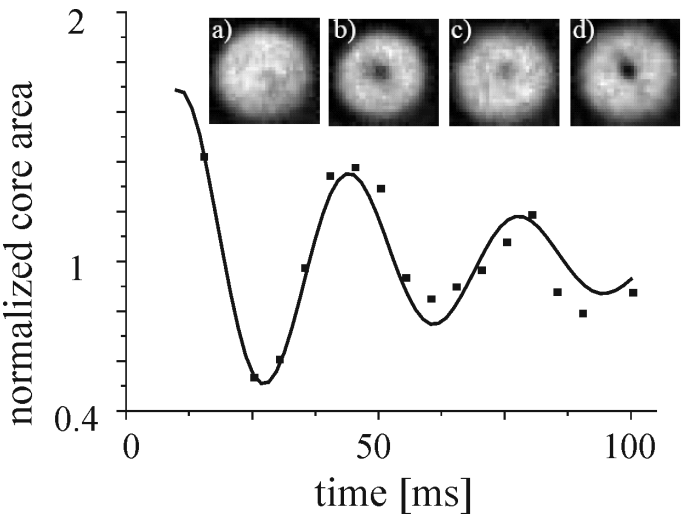

Figure 3.4: Oscillation of core area after an 8 pW, 5 ms laser pulse. Starting conditions are 2.5×10^6 atoms with rotation rate $\Omega = 0.9\,\omega_\rho$.Time given is in-trap evolution time after end of pulse. Core area is normalized to mean of all data points. Inset: Initial conditions 3.5×10^6 atoms with rotation rate $\Omega = 0.78\,\omega_\rho$; in-trap images taken after a 14 pW, 5 ms laser pulse followed by evolution time of (a) 20 ms, (b) 40 ms, (c) 60 ms, and (d) 80 ms.

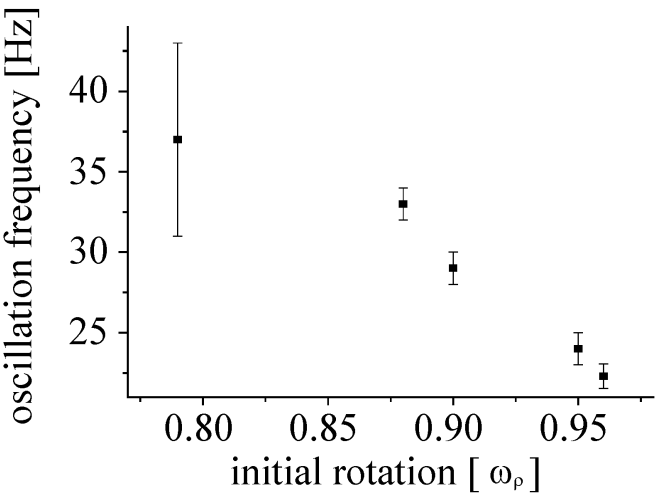

Figure 3.5: Measured oscillation frequencies of the aggregate size for different rotation rates. Oscillations were excited by a 5 ms long, resonant laser pulse that removed all atoms within a radius of 1/3 the Thomas Fermi radius of the BEC.

vortex lattice rotation period ($2\pi/(0.95\,\omega_\rho) = 126\ ms$) so as to create only a local hole. By using different laser powers, we can vary the size of the core from a small hole as in figure 3.6(a) all the way to the extreme case of a big hole that only leaves a crescent segment of the BEC as shown in figure 3.6(c). The precession of these holes can be monitored by applying variable evolution times of the trapped BEC after the atom removal pulse is finished. In all three cases the measured precession frequency is approximately ω_ρ. In the case of figure 3.6(b) and (c) we are able to follow the precession for more than 20 cycles. If, instead, the laser is left on for approximately a full lattice rotation cycle, a complete ring can be cut out of the condensate [figure 3.7(a)], which eventually breaks up into many individual blobs [figure 3.7(c)], each of which supports remnants of the original lattice. Both the long-lived core precession as well as the ring structure in figure 3.7 are impressive demonstrations of the stability of density features due to Coriolis forces in rapidly rotating condensates.

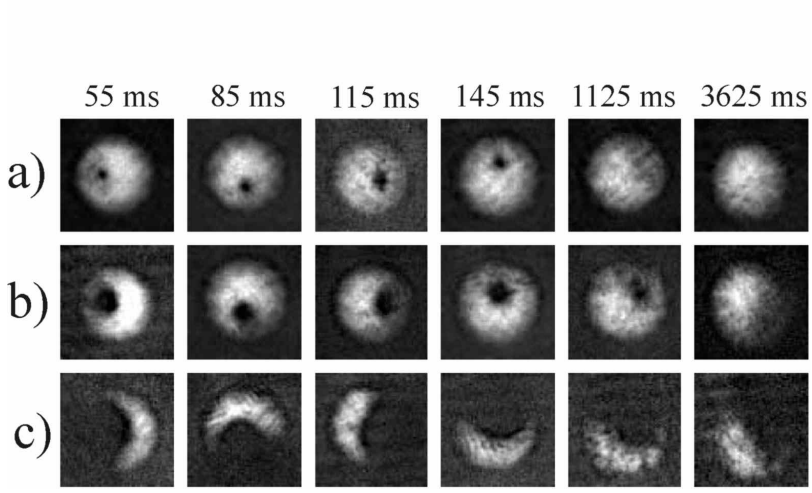

Figure 3.6: Giant core precession. Cores created by a 10 ms off-centered laser pulse with a power of (a) 4.2 pW, (b) 33 pW, (c) 470 pW. Time given in figure is in-trap evolution time after end of laser pulse. For reference, a naive expectation for the lifetime of a giant vortex given by the radius of the core divided by the speed of sound in the surrounding cloud would be 13 ms and 30 ms for (a) and (b), respectively.

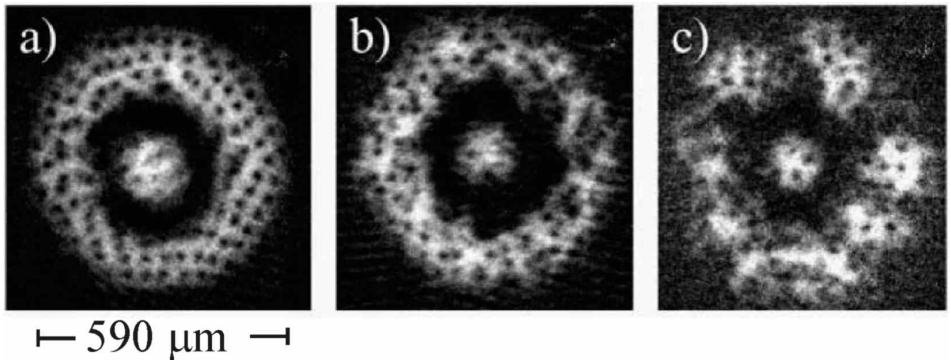

Figure 3.7: Ring cut out of a BEC by a 125 ms long, off-centered laser pulse. Expansion image taken (a) directly after end of pulse (b) after an additional in-trap evolution time of 200 ms after end of pulse and (c) evolution time 2 s.

Chapter 4

Tkachenko Modes [3]

4.1 Introduction

We have all seen a cylindrically confined fluid support azimuthal flow whether we are watching water flow down a drain or a recently stirred cup of coffee. What is somewhat harder to imagine is a fluid sustaining oscillatory azimuthal flow. Instinctively one does not expect a fluid to support shear forces, and this would seem especially true in the case of zero-viscosity superfluids, but such intuition is incomplete.

The key issue is vortices. In 1955, Feynman [16] predicted that a superfluid can rotate when pierced by an array of quantized singularities or vortices. In 1957, Abrikosov [74] demonstrated that such vortices in a type II superconductor will organize into a triangular crystalline lattice due to their mutual repulsion. Not surprisingly, the Abrikosov lattice has an associated rigidity. In 1966, Tkachenko proposed that a vortex lattice in a superfluid would support transverse elastic modes [26]. First observed by Andereck **et al.**[27], Tkachenko oscillations have been the object of considerable experimental and theoretical effort in superfluid helium, much of which was summarized by Sonin in 1987 [75].

In the last two years it has become possible to achieve a vortex lattice state in dilute gas BEC [22, 24, 23, 25] and recent theoretical work [28] has suggested that Tkachenko oscillations are also attainable. In this chapter I discuss the observation of Tkachenko oscillations in BEC. The particular strengths of BEC are that in the clean en-

vironment of a magnetically trapped gas there is no vortex pinning, and spatiotemporal evolution of the oscillation may be directly observed.

When we started our experimental investigation of Tkachenko modes, the only theory available to compare to was the one given in [28] by Anglin and Crescimanno. As described during the discussion of our experimental work in the following section, the oscillation frequencies predicted by this initial theory were not in excellent quantitative agreement with our experiments. As I will describe in §4.6, it was later pointed out by Gordon Baym that a more adequate theory for our experiments needs to account for compressibility effects of the lattice. This hints at a major difference between Tkachenko wave experiments in liquid Helium and in dilute gas BECs: Our experiments reach into a new regime that lies outside the region accessible with liquid Helium experiments.

4.2 Exciting Tkachenko modes

As before we begin this experiment with a rotating condensate held in an axially symmetric trap with trap frequencies $\{\omega_\rho, \omega_z\} = 2\pi\{8.3, 5.2\}$ Hz. The condensed cloud contains 1.5-2.9 million ^{87}Rb atoms in the $|F = 1, m_F = -1\rangle$ state. The cloud rotates about the vertical, z axis. Condensate rotation rates (Ω) for the experiments described in this chapter range from $\Omega = 0.84\omega_\rho$ to $\Omega = 0.975\omega_\rho$ (Ω defined as condensate rotation rate divided by ω_ρ). We have no observable normal cloud implying a T/Tc < 0.6. As before, rotation can be accurately measured by comparing the condensate aspect ratio to the trap aspect ratio using equation 2.2. Vortices, which are too small to observe in trap, can be seen by expanding the cloud as detailed in §2.3. At our high rotation rates the condensate is oblate and the vortex cores are essentially vertical lines except right at the surface.

We excite lattice oscillations by two mechanisms. The first mechanism presented is based on the selective removal of atoms that has also been discussed in §3.2. With this method we remove atoms at the center of the condensate with a resonant, focused laser

beam sent through the condensate along the axis of rotation. The width of the "blasting" laser beam is 16 μm FWHM (small compared to an in-trap condensate FWHM of 75 μm), with a Gaussian intensity profile. The frequency of the laser is tuned to the $F'' = 1 \rightarrow F' = 0$ transition of the D2 line, and the recoil from a spontaneously scattered photon blasts atoms out of the condensate. The laser power is about 10 fW and is left on for approximately one lattice rotation period (125 ms).

The effect of this blasting laser is to remove a small (barely observable) fraction of atoms from the center of the condensate. This has two consequences. First, the average angular momentum per particle is increased by the selective removal of low angular momentum atoms from the condensate center. This increase then requires a corresponding increase in the equilibrium condensate radius [76]. Secondly, the atom removal creates a density dip in the center of the cloud. Thus, after the blasting pulse, the condensate has fluid flowing inward to fill the density dip and fluid flowing outward to expand the radius. The Coriolis force acting on these flows causes the inward motion to be diverted in the lattice rotation direction and the outward flow to be diverted in the opposite direction. This sheared fluid flow drags the vortices from their equilibrium configuration and sets the initial conditions for the lattice oscillation as can be seen from the expanded images in figure 4.1.

The second method of exciting the Tkachenko oscillation is essentially the inverse of the previous method. Instead of removing atoms from the cloud we use a red-detuned optical dipole potential to draw atoms into the middle of the condensate. To do this we focus a 850 nm laser beam onto the condensate. The beam has 3 μW of power and a 40 μm FWHM. It propagates along the direction of condensate rotation and its effect is to create a 0.4 nK deep Gaussian dip in the radial trapping potential. This beam is left on for 125 ms to create an inward fluid flow similar to before. The resulting Tkachenko oscillation was studied for $\Omega = 0.95\omega_\rho$, and found to be completely consistent with the atom removal method. It is not surprising that these two methods are equivalent since

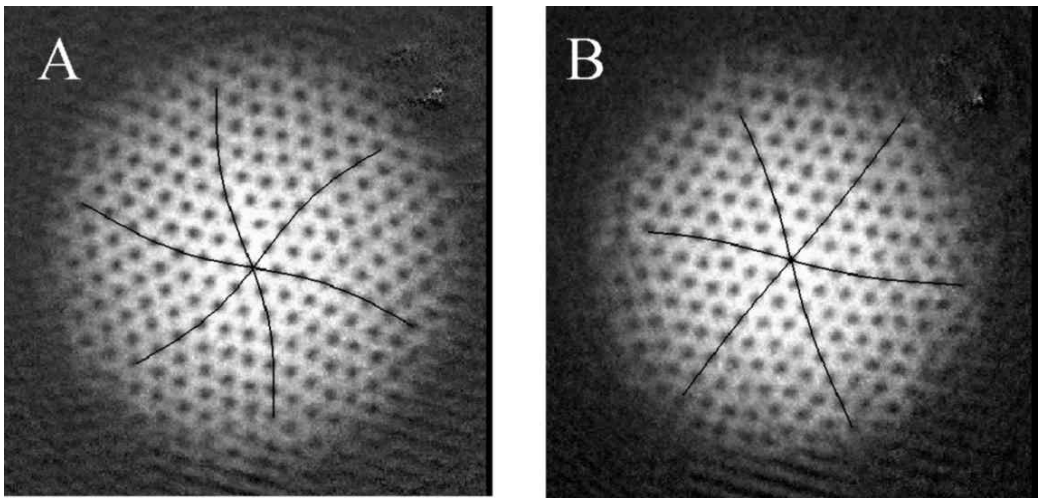

Figure 4.1: (1,0) Tkachenko mode excited by atom removal (a) taken 500 ms after the end of the blasting pulse (b) taken 1650 ms after the end of the blasting pulse. BEC rotation is counterclockwise. Lines are sine fits to the vortex lattice planes.

one works by creating a dip in the interaction potential and the other creates a similar dip in the trapping potential.

For these experiments, data is extracted by destructively imaging the vortex lattice in expansion and fitting the lattice oscillation. To perform this fit we find a curvilinear row of vortices going through the center of the cloud and fit a sinewave to the locations of the vortex centers, recording the sine amplitude. This is done for all three directions of lattice symmetry [see figure 4.1], with the amplitudes averaged to yield the net fit amplitude of the distortion.

4.3 The (1,0) mode

The resulting oscillation [see figure. 4.2] is heavily damped and has a Q value of 3-5 for the data presented. Here Q is given by Q=$2\pi f \tau_{damping}$, where $\tau_{damping}$ is the exponential-damping time constant for the oscillation. We are able to increase this to a Q of 10 by exciting lower amplitude oscillations (40% of the previous amplitude) and by better mode matching of the blasting beam to the shape and period of the oscillation (40 μm FWHM beam width and 500 ms blasting time). Measured frequencies for the high-amplitude oscillations are the same as for the low-amplitude, high-Q case so we do not believe that we are seeing anharmonic shifts[1] .

Because of the characteristic s-bend shape and the low resonant frequency of these oscillations [see figure 4.3(a)] we interpret them to be the (n=1,m=0) Tkachenko oscillations predicted by Anglin and Crescimanno [28]. Here (n,m) refer to the radial and angular nodes, respectively, in the presumed quasi-2-D geometry. The calculations of Ref.[28] predict that these lattice oscillations should have a frequency of $\nu_{10} = 1.43\epsilon\Omega/(2\pi)$ for the (1,0) mode and $\nu_{20} = 2.32\epsilon\Omega/(2\pi)$ for the (2,0) mode. Here $\epsilon = b/R_\rho$ denotes the nearest-neighbor vortex spacing, b, over the radial Thomas-Fermi radius, R_ρ. For our

[1] Note that for all cases the reported frequency is adjusted for damping according to the equation $f_o = 1/2\pi((2\pi f_{measured})^2 + (1/\tau_{damping})^2)^{1/2}$.

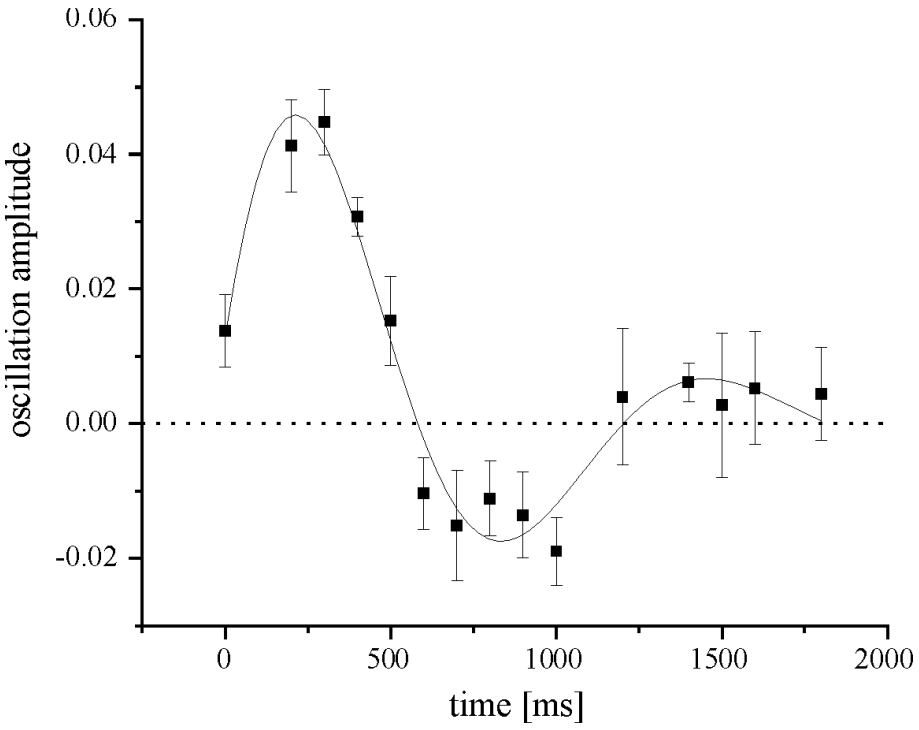

Figure 4.2: Measured oscillation amplitude for a typical excitation. Data shown is for a BEC rotating at $\Omega = 0.92\omega_\rho$ and containing 2.2×10^6 atoms. Fit is to a sinewave times an exponential decay and yields a frequency of 0.85 Hz and a Q of 3. The oscillation amplitude is expressed as the average amplitude of the sinewave fits to the vortex oscillation in units of the radial Thomas-Fermi radius (roughly the azimuthal displacement of a vortex a distance 0.33 R_ρ from the condensate center). Both values are in expansion.

system these predicted frequencies are around 1-2 Hz and are therefore far slower than any of the density-changing coherent oscillations of the condensate except for the m=-2 surface wave [25, 77, 40, 78]. In addition, the shape of the observed oscillation agrees well with theory. Specifically, the prediction[28] that the spatial period of a sinewave fit to a row of vortices in a (1,0) oscillation should be 1.33 R_ρ is in perfect agreement with our data.

The predicted frequencies are, however, problematic. To make the comparison to the theory presented in Ref.[28] we excite lattice oscillations in the condensate for $\epsilon\Omega/\omega_\rho$ ranging from 0.10 to 0.15. This is achieved by varying number and rotation rate. Over this range of $\epsilon\Omega$ the oscillation frequencies measured are consistently lower than those predicted by theory as can be seen in figure 4.3(b). For the slowest rotations, $\Omega = 0.84\omega_\rho$ ($\epsilon\Omega/\omega_\rho = 0.15$, N=$2.5\times10^6$), we observe frequencies that are as close as 0.70 of the predicted value. However, at larger rotation rates, $\Omega = 0.975\omega_\rho$ ($\epsilon\Omega/\omega_\rho = 0.10$, N=$1.7 \times 10^6$), the agreement is considerably worse (the measured value is 0.31 of the predicted value). One possible explanation for this general discrepancy is that the calculations are done in 2-D and ignore the issues of vortex bending at the boundary and finite condensate thickness [79]. In those cases, however, one would expect better agreement at high rotation rates where the condensate aspect ratio is more 2-D. A more likely explanation is that the continuum theory, used in the Anglin and Crescimanno calculation, is breaking down as the vortex core size to vortex spacing becomes finite [79]. This suggests that at high rotation and lower atom number we are entering a new regime. To further explore this possibility we reduced the atom number to N=$7-9\times10^5$, while keeping $\epsilon\Omega/\omega_\rho$ roughly the same. This should increase the core size and exacerbate the problem. As can be seen in figure 4.3(b) and figure 4.3(c) the agreement with theory is significantly worse under these conditions. These discrepancies will be discussed in more detail in §4.6.

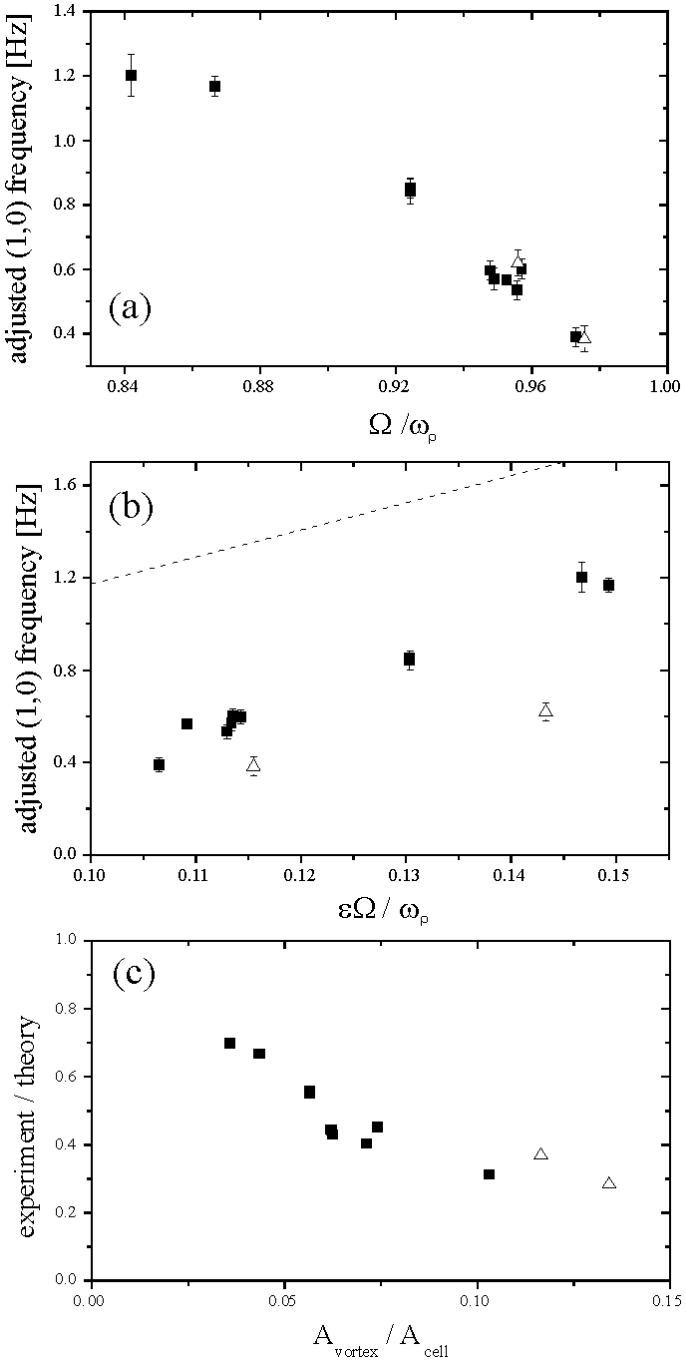

Figure 4.3: Plot (a) shows the damping-adjusted (n=1,m=0) Tkachenko oscillation frequencies as a function of scaled rotation rate Ω/ω_ρ. Plot (b) shows the (1,0) frequency as a function of the theory parameter $\epsilon\Omega/\omega_\rho$. The dotted line is the theory line $\nu_{10} = 1.43\epsilon\Omega/(2\pi)$ from Ref. [28]. Note that the low number data shows much worse agreement with theory. Plot (c) demonstrates the divergence of experimental frequency from the theory frequency as the ratio of vortex core area to unit cell area increases. A_{vortex} is $\pi\xi^2$ where the healing length $\xi = (8\pi na)^{-1/2}$ (here n is density-weighted average density and a is the s-wave scattering length). Lattice cell area A_{cell} is $\sqrt{3}b^2/2$ (here b is the nearest-neighbor vortex spacing). For all plots black squares and triangles refer to high and low atom number experiments, respectively.

4.4 The (2,0) mode

We are also able to excite the (2,0) mode. We note that atom removal creates an s-bend in the lattice that is centered on the atom removal spot. To write two s-bends onto the lattice one could imagine removing atoms from an annular ring instead of a spot. To make this ring we offset the blasting beam half a condensate radius and leave it on for 375 ms (three full condensate rotation periods). As one can see this does lead to an excitation of the (2,0) oscillation (see figure 4.4). We measure the frequency of this mode as before. For 2.3 million atoms and $\Omega = 0.95\omega_\rho$ we measure a lattice oscillation frequency of 1.1 ± 0.1 Hz, distinctly lower than the theoretical prediction [28] of 2.2 Hz for our parameters.

4.5 Bulk fluid modes

Vortex motion and condensate fluid motion are intimately linked [75]. In Tkachenko oscillations, the moving of vortices must also entail some motion of the underlying fluid, and pressure-velocity waves in the fluid must conversely entrain the vortices. Very generally, for a substance composed of two interpenetrating materials, one of which has an elastic shear modulus and one of which does not (in our case, the vortex lattice and its surrounding superfluid, respectively), one expects to find three distinct families of sound waves in the bulk: (i) a shear, or transverse, wave, (ii) a common-mode pressure or longitudinal wave, and (iii) a differential longitudinal wave, with the lattice and its fluid moving against one another [80]. The presence of strong Coriolis forces makes the distinction between longitudinal and transverse waves problematic, but the general characteristics of the three families should extend into the rotating case. For instance, one can still readily identify the Tkachenko modes discussed thus far as the transverse wave. Our assumption is that the common-mode longitudinal waves are nothing other than the conventional hydrodynamic shape oscillations studied previously [40, 78].

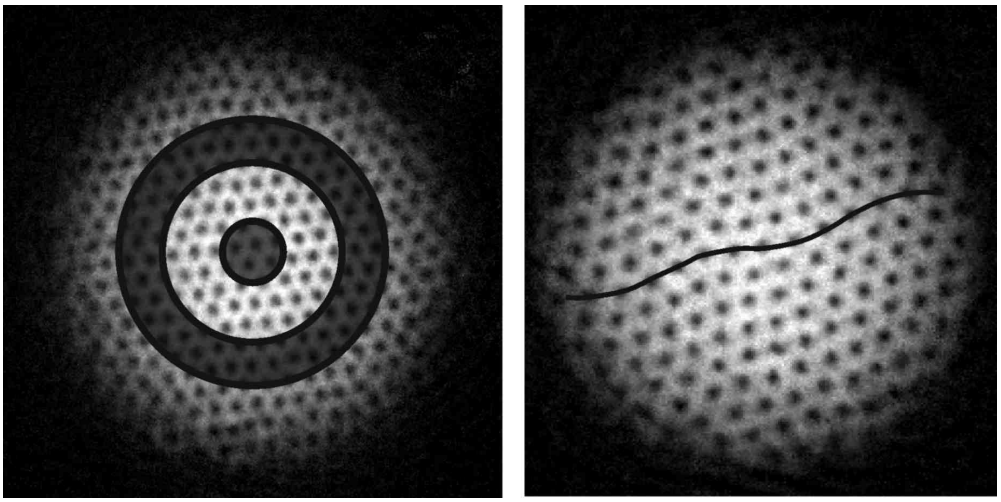

Figure 4.4: On the left are the locations where atoms are removed from the cloud. For the (1,0) excitations the atoms are removed from the shaded region in the center. For the (2,0) mode atoms are removed from the shaded ring half a condensate radius out. Image on the right is the resulting (2,0) mode, where the black line has been added to guide the eye.

To excite the common-mode longitudinal wave, we use the dipole force from the 850 nm red-detuned laser described earlier. In order to excite a broad spectrum of modes we shorten the laser pulse to 5 ms, widen the excitation beam to a 75 μm FWHM Gaussian profile, and increase the laser power to 1 mW, resulting in a 30 nK deep optical potential. We find that this pulse excites three distinct m=0 modes: the first is the (1,0) Tkachenko s-bend mode at about 0.6 Hz already discussed. The second is a radial breathing mode in which the condensate radius oscillates at 16.6 ± 0.3 Hz (or $2.0 \pm 0.1 \frac{\omega_\rho}{2\pi}$). This mode has been previously observed [81], and our observed frequency is consistent with hydrodynamic theory for a cloud rotating at $\Omega = 0.95\omega_\rho$ [40]. As the radius of the fluid density oscillates, so does the mean lattice spacing of the vortex lattice, but we observe no s-type bending of the lattice at this frequency. The fact that the frequency of the lowest m=0 radial longitudinal mode is more than 20 times that of the transverse mode demonstrates how relatively weak the transverse shear modulus is.

The same laser pulse excites a third mode, at the quite distinct frequency of $18.5 \pm$ 0.3 Hz. This mode manifests as a rapid s-bend distortion of the lattice indistinguishable in shape from the 0.6 Hz (1,0) Tkachenko oscillation as can be seen in figure 4.5. 18.5 Hz is much too fast to have anything to do with the shear modulus of the lattice, and we were very tempted to identify this mode as a member of the third family of sound-waves, the differential longitudinal waves. Simulations by Cozzini and Stringari [82, 83], however, show that our observed frequency is consistent with a higher-order, hydrodynamic mode of the rotating fluid that can be excited by an anharmonic radial potential such as our Gaussian optical potential. Moreover, they show that the radial velocity field of their mode is distorted by Coriolis forces so as to drag the lattice sites into an azimuthally oscillating s-bend distortion that coincidentally resembles the Tkachenko mode. It is worth noting that without the presence of the lattice to serve as tracers for the fluid velocity field, it would be very difficult to observe this higher-order mode, since this mode has very little effect on the mean radius of the fluid. In any case, the mode at

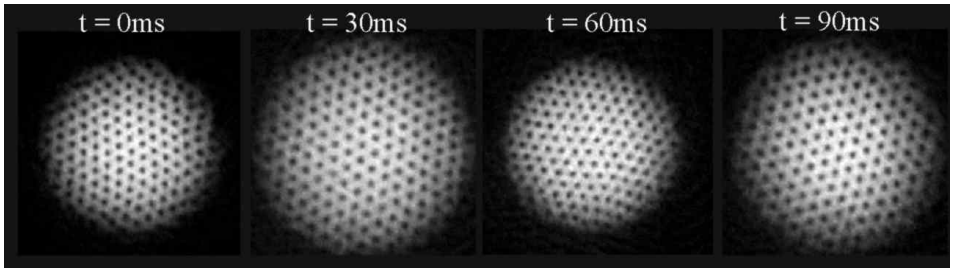

Figure 4.5: Radial breathing mode and fluid flow driven lattice bending as observed after a dipole beam pulse. For parameters, see text.

18.5 Hz appears to be yet another member in the family of common-mode longitudinal waves. The discovery of this longitundnal mode demonstrates the usefulness of vortices to visualize complicated hydrodynamic flow patterns in a BEC. So far we have been unable to observe a mode we can assign to the family of differential longitudinal waves.

4.6 Theory responds

In section §4.2 and in our original Tkachenko [84] paper, I suggest that our discrepancy with the Anglin and Crescimanno prediction, seen in figure 4.3, is due to the finite size of the vortex cores, which turns out not to be completely true. Finite core size turns out to be tantamount to saying that we are approaching the lowest Landau level (described in more detail in §5). As it happens, the lowest Landau level dynamics describe only a small part of this discrepancy. Since the original publishing of the Tkachenko paper there has been an extensive theory response [29, 83, 31, 85, 33, 86, 32]. A central point of nearly all these works is that lattice compressibility must be taken into account to describe the Tkachenko oscillation in BEC's.

In a highly rotating condensate the rotation rate can easily approach or even exceed the speed of sound in the condensate. As the speed of sound is approached, the lattice becomes compressible, and enters a regime not accessible to superfluid Helium systems. This compressibility also means that higher-order terms must be taken into account when determining the Tkachenko dispersion relation. As noted by Baym [29,

87, 88] the dispersion relation

$$\nu(k)^2 = \frac{1}{(2\pi)^2}\frac{2C_2}{nm}\frac{s^2k^4}{(4\Omega^2 + (s^2 + 4(C_1 + C_2)/nm)k^2)} \ . \tag{4.1}$$

Here n in the condensate density[2] and m is the mass of Rubidium. The wave number k for the (1,0) mode is taken, from Anglin and Crescimanno [28], to be $k_{(1,0)} = 2\pi/(1.33R_\rho)$ and s is the speed of sound. C_1 and C_2 are the compressional and shear modulus of the lattice respectively. In the incompressible limit, one would expect that $C_2 = -C_1 = n\Omega/8$. However, as Baym notes, the shear modulus weakens with higher rotation and as one approaches the lowest Landau level C_2, is know to have the form $C_2 \simeq (81/80\pi)ms^2n$ [29, 87, 88]. The exact nature of the transition between these two limits has not been rigorously determined.

Equation 4.1 can be broken into two interesting regimes. At low rotations ($\Omega \ll sk$), equation 4.1 simplifies to

$$\nu(k) = \frac{1}{2\pi}\sqrt{\frac{2C_2}{nm}}k \ . \tag{4.2}$$

This low rotation regime is often referred to as the "stiff" Thomas Fermi regime. In this regime, Tkachenko oscillations are expected to behave much like they do in superfluid helium systems, and the theory presented in Ref. [28] would be more appropriate. However, one notes that in our system $sk_{(1,0)} \simeq 0.66\omega_\rho$, which means that we are well out of this regime by the time our vortex lattices are large enough to observe a Tkachenko oscillation.

Alternatively, at high rotations ($\Omega \gg sk$) one enters the "soft" Thomas-Fermi regime where equation 4.1 simplifies to

$$\nu(k) = \frac{1}{2\pi}\sqrt{\frac{s^2C_2}{2\Omega^2nm}}k^2 \ . \tag{4.3}$$

The Tkachenko data presented in this thesis generally lies between these two regimes or in the "soft" regime. This second dispersion relation is striking in its' quadratic

[2] Baym uses peak density in his original paper but we have found that density-weighted density provides an equally good fit to the data and requires less fudging with the C_2 parameter. Density-weighted density also would seem appropriate as the Tkachenko excitation exists over the entire cloud.

behavior and is expected to lead to loss of long range phase coherence in the condensate [85]. Ultimately this loss of phase coherence is expected to lead to melting of the vortex lattice as one approaches the quantum Hall regime [89].

The Bigelow group has spent some time using numerics to examine the difference between these two regimes. A striking difference in the flow patterns in these two regimes can be seen in figure 4.6 which was provided by L. O. Baksmaty [83].

Interesting work has also been done on the condensate density profile during a Tkachenko oscillation. Using a sum rule method Cozzini **et al.** [32] has demonstrated that the condensate density profile dips slightly ($\sim$5%) in the center and the outer edge during a Tkachenko oscillation. This profile offers some insight into why our experimental technique of altering the condensate profile at the center, couples so nicely to the Tkachenko modes. They also suggest an alternate scheme of exciting these modes by modulating the radial trap frequencies, at the Tkachenko frequency, in order to couple to this density distribution. While so far untested, this suggestion would provide a way to perform frequency resolved spectroscopy of Tkachenko oscillations, which may one day prove useful.

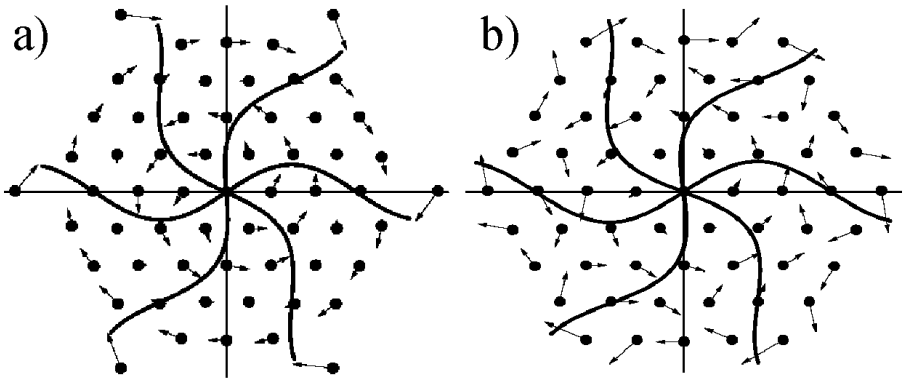

Figure 4.6: Figure taken from Ref. [83]. Plot a) and b) show the vortex lattice distortion resulting from a (1,0) Tkachenko mode in the stiff and soft Thomas-Fermi regimes respectively. Dots show the equilibrium vortex positions and the arrows show the direction and magnitude of the calculated vortex displacements. In plot a) one can see the very ordered nature of the Tkachenko oscillation. A time evolution of this image shows that each vortex precesses along a highly elliptical path. In soft Thomas Fermi regime, plot b), individual vortex motion appears more chaotic as the lattice becomes compressible. A time evolution of this image shows that the precession of each vortex has become nearly circular. All vortices at the same radii precess in the same manner.

Chapter 5

Lowest Landau Level [4]

5.1 Introduction

Rotating Bose-Einstein condensates provide a conceptual link between the physics of trapped gases and the physics of condensed matter systems such as superfluids, type-II superconductors and quantum Hall effect (QHE) materials. In all these systems, striking counterintuitive effects emerge when an external flux penetrates the sample. For charged particles this flux can be provided by a magnetic field, leading to the formation of Abrikosov flux line lattices in type-II superconductors [74], or in QHE systems to the formation of correlated electron-liquids and composite quasiparticles made of electrons with attached flux quanta [90]. For neutral superfluids, the analog to a magnetic field is a rotation of the system, which similarly spawns vortices [91]. In rotating atomic BECs, the creation of large ordered Abrikosov lattices of vortices [22, 24, 23, 25] has recently become possible.

Here we examine the vortex lattice of harmonically trapped BECs approaching the high rotation limit, when the centrifugal force nearly cancels the radial confining force. The formal analogy of neutral atoms in this limit with electrons in a strong magnetic field has led to the prediction that quantum-Hall like properties should emerge in rapidly rotating atomic BECs [37]. In particular, the single-particle energy states, in the rotating frame, organize into Landau levels (see figure 5.1), and if interactions are weaker than the cyclotron energy (approximately the energy splitting between Landau

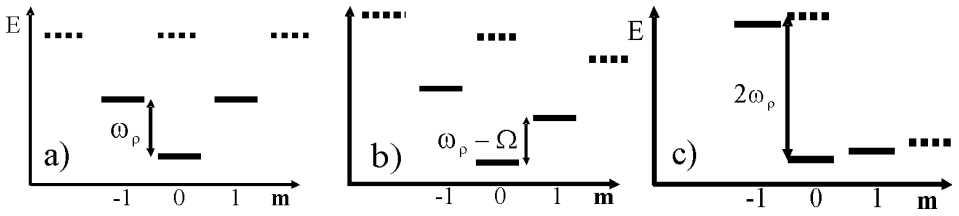

Figure 5.1: Harmonic oscillator states in the rotating frame as one approaches the lowest Landau level. Image a) shows the non-rotating case. With moderate condensate rotation the positive/negative m harmonic oscillator states shift down/up in energy as seen in image b). As condensate rotation rate (Ω) approaches the trap frequency (ω_ρ) the harmonic oscillator states form bands, or Landau levels, as in image c). The condensate becomes confined to the lowest Landau level if the chemical potential drops below the Landau level splitting ($2\omega_\rho$).

levels), the near-degenerate states of the lowest Landau level (LLL) are primarily occupied. For rotating bosons in the LLL, two regimes have been identified, distinguished by the filling factor $\nu \equiv N_p/N_v$, i.e., the ratio of the number of particles (N_p) to vortices (N_v). For high filling factors (always ≥ 500 in our system), the condensate is in the lowest Landau level regime [35, 19, 36], but mean-field theory is still a valid way to deal with interactions. In this state the condensate still forms an ordered vortex lattice ground state. With decreasing filling factor, the elastic shear strength of the vortex lattice decreases, which is reflected in very low frequencies of long-wavelength transverse lattice excitations (Tkachenko oscillations [28, 84, 29, 43, 30, 31, 83, 85, 33, 86, 32])[1] . For filling factors around $\nu \approx 10$, the shear strength is predicted to drop sufficiently for quantum fluctuations to melt the vortex lattice[37, 38]. For smaller ν there exists a variety of strongly correlated vortex liquid states similar to those in the Fermionic fractional QHE [37]. Starting from the Laughlin state, one can then even create excitations that obey fractional statistics [39].

In this chapter we report the observation of rapidly rotating BECs in the lowest Landau level, and provide evidence that the elastic shear strength of the vortex lattice

[1] Ref. [84] measured Tkachenko frequencies that showed deviations from existing TF-limit theory valid at low rotation [28] (also shown in §4.3). These were resolved in subsequent theoretical work [29, 30, 31].

drops substantially as the BEC enters the lowest Landau level regime [29]. This effect is a precursor to the predicted quantum melting of the lattice at lower filling factors. Our rapidly rotating condensates spin out into a pancake shape and approach the quasi-two-dimensional regime. We observe a corresponding cross-over in the spectrum of breathing excitations along the axial direction. The high rotation limit has been studied experimentally in Ref. [92], focusing on effects of a rotating trap anisotropy, which is not present in our setup, and in Ref. [93] where the addition of a quartic term to the trapping potential led to a loss of vortex visibility.

5.2 Experiment

These experiments take place in an axially symmetric harmonic trap with oscillation frequencies $\{\omega_\rho, \omega_z\} = 2\pi\{8.3, 5.3\}$ Hz. Using an evaporative spin-up technique described in §2.1 we create condensates containing up to 5.5×10^6 ^{87}Rb atoms in the $|F = 1, m_F = -1\rangle$ state, rotating about the vertical, z axis, at a rate $\tilde{\Omega} = 0.95$ ($\tilde{\Omega} \equiv \Omega/\omega_\rho$ is the rotation rate Ω scaled by the centrifugal rotation limit, ω_ρ, for a harmonically trapped gas). To further approach the limit $\tilde{\Omega} \to 1$, we employ an optical spin-up technique, where the BEC is illuminated uniformly with laser light, and the recoil from spontaneously scattered photons removes atoms from the condensate. Since the condensate is optically thin to the laser light, atoms are removed without position or angular-momentum selectivity, such that angular momentum per particle is unchanged. Atom loss leads to a small decrease in cloud radius which, through conservation of angular momentum, increases $\tilde{\Omega}$. Over a period of up to 2 seconds we decrease the number of BEC atoms by up to a factor of 100, to 5×10^4, while increasing[2] $\tilde{\Omega}$ from 0.95 to more than 0.99. At this point, further reduction in number degrades the quality of images unacceptably. Ongoing evaporation is imposed to retain a quasi-pure BEC with

[2] Rotation rates are accurately determined by comparing the measured BEC aspect ratio to the trap aspect ratio (see e.g. [40]). At our lowest values of Γ_{2D} we correct for quantum-pressure contributions to axial size.

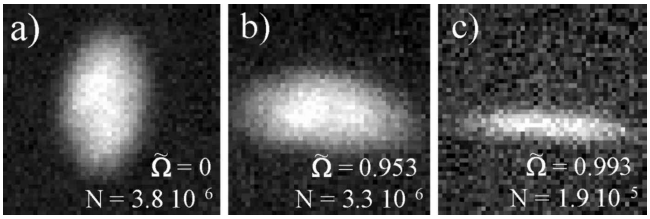

Figure 5.2: Side view images of BECs in trap. (a) Static BEC. The aspect ratio $R_z/R_\rho = 1.57$ ($N = 3.8 \times 10^6$ atoms) resembles the prolate trap shape. (b) After evaporative spin-up, $N = 3.3 \times 10^6$, $\tilde{\Omega} = 0.953$, (c) evaporative plus optical spin-up, $N = 1.9 \times 10^5$, $\tilde{\Omega} = 0.993$. Due to centrifugal distortion the aspect ratio is changed by a factor 8 compared to (a).

no discernible thermal cloud.

5.3 Breathing mode spectrum in the lowest Landau level

With increasing rotation, centrifugal force distorts the cloud into an extremely oblate shape [see figure 5.2] and reduces the density significantly - thus the BEC approaches the quasi-two-dimensional regime. For the highest rotation rates we achieve, the chemical potential μ is reduced close to the axial oscillator energy, $\Gamma_{2D} \equiv \frac{\mu}{2\hbar\omega_z} \approx 1.5$, and the gas undergoes a cross-over from interacting- to ideal-gas behavior along the axial direction.

To probe this cross-over, we excite the lowest order axial breathing mode over a range of rotation rates. For a BEC in the axial Thomas-Fermi regime, an axial breathing frequency $\omega_B = \sqrt{3}\,\omega_z$ has been predicted in the limit $\tilde{\Omega} \to 1$ [40], whereas $\omega_B = 2\,\omega_z$ is expected for a non-interacting gas.

To excite the breathing mode, we jump the axial trap frequency by 6%, while leaving the radial frequency unchanged (within $< 0.5\%$). To extract the axial breathing frequency ω_B, we take 13 nondestructive in-trap images of the cloud, perpendicular to the axis of rotation. From the oscillation of the axial Thomas-Fermi radius[3] in time we obtain ω_B. Rotation rates are obtained from the aspect ratio by averaging over

[3] For the smallest values Γ_{2D}, the axial density profile is slightly better fitted by a Gaussian. To avoid bias however we fit all data assuming a TF profile.

all 13 images to eliminate the effect of axial breathing. As shown in figure 5.3(a), we do indeed observe a frequency cross-over from $\omega_B = \sqrt{3}\,\omega_z$ to $\omega_B = 2\,\omega_z$ as $\tilde{\Omega} \to 1$. To quantify under which conditions the cross-over occurs, we plot the same data vs. Γ_{2D} [figure 5.3(b)], where the chemical potential is determined from the measured atom number, the rotation rate and the trap frequencies. For $\Gamma_{2D} < 3$, the ratio ω_B/ω_z starts to deviate from the predicted hydrodynamic value, and approaches 2 for our lowest $\Gamma_{2D} \approx 1.5$.

As $\tilde{\Omega} \to 1$, the dynamics in the radial plane are also affected. For the highest rotation rates, interactions become sufficiently weak that the chemical potential μ drops below the cyclotron energy $2\hbar\Omega$, which is only a few percent smaller than the Landau level spacing $2\hbar\omega_\rho$. Then, $\Gamma_{LLL} \equiv \frac{\mu}{2\hbar\Omega} < 1$, and the condensate primarily occupies single-particle states in the LLL. These form a ladder of near-degenerate states, with a frequency splitting of $\epsilon = \omega_\rho - \Omega$. The number of occupied states is $N_{LLL} \approx \frac{\mu}{\hbar\epsilon}$. We are able to create condensates with Γ_{LLL} as low as 0.6, which occupy $N_{LLL} \approx 120$ states, with a splitting $\epsilon < 2\pi \times 0.06\,\mathrm{Hz}$. In this regime of near-degenerate single-particle states a drastic decrease of the lattice's elastic shear strength takes place. The elastic shear modulus, C_2, is predicted by Baym [29] to decrease with increasing rotation rate from its value in the "stiff" Thomas-Fermi (TF) limit, $C_2^{TF} = n_{(\Omega)}\hbar\Omega/8$ (where $n_{(\Omega)}$ is the BEC number density) to its value in the mean-field quantum Hall regime, of $C_2^{LLL} \approx 0.16 \times \Gamma_{LLL} \times C_2^{TF}$. We directly probe this shear strength by exciting the lowest order azimuthally symmetric lattice mode ($(n = 1, m = 0)$ Tkachenko mode [28, 84, 29]). Its frequency $\omega_{(1,0)} \sim \sqrt{C_2}$ is expected to drop by a factor ≈ 2.5 below the TF prediction when $\Gamma_{LLL} = 1$.

5.4 Tkachenko spectrum in the lowest Landau level

Our excitation technique for Tkachenko modes has been described in §4.2. Here the lower interaction strength of the condensates makes it preferable to use the focused,

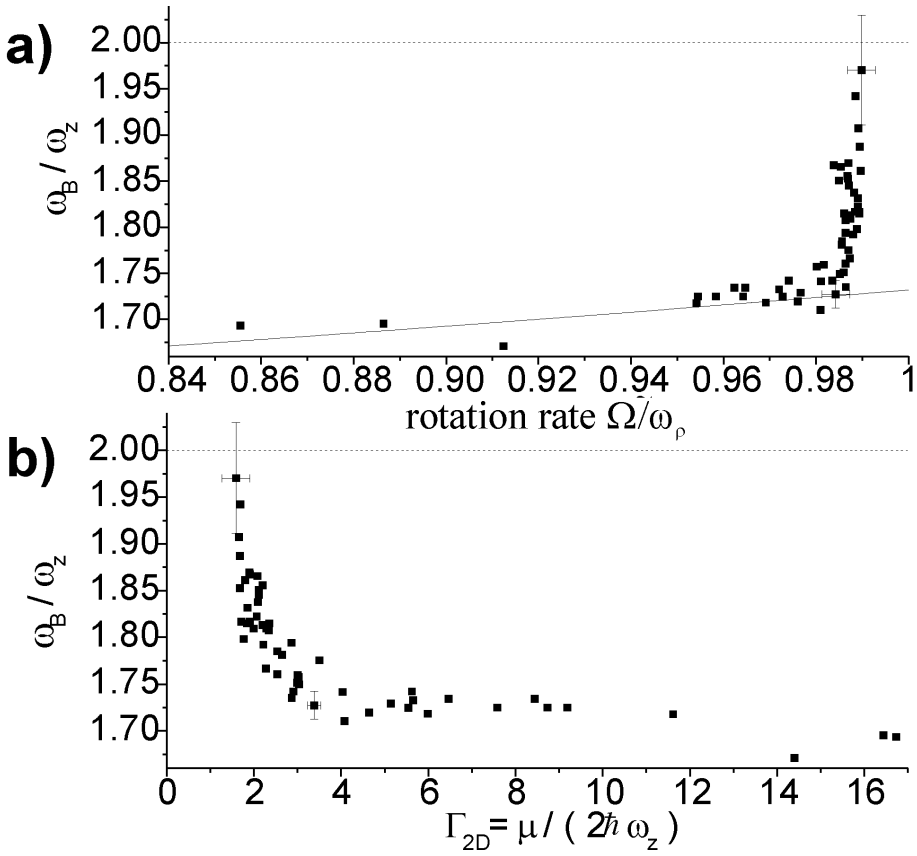

Figure 5.3: Measured axial breathing frequency ω_B/ω_z (a) as a function of rotation rate $\tilde{\Omega}$ and (b) vs. Γ_{2D}. Solid line: Prediction for the hydrodynamic regime [40]; Dashed line: ideal gas limit. For $\tilde{\Omega} > 0.98$ ($\Gamma_{2D} < 3$) a cross-over from interacting- to ideal-gas behavior is observed. Representative error bars are shown for two data points.

red-detuned laser (850 nm). This laser draws atoms into the center, and Coriolis force diverts the atoms' inward motion into the lattice rotation direction. The vortex lattice adjusts to this distortion, and after we turn off the beam, the lattice elasticity drives oscillations at the frequency $\omega_{(1,0)}$. We observe the oscillation by varying the wait time after the excitation, and then expanding the condensate before imaging the vortex lattice along the z-axis [see figure 5.4(a),(b)]. In figure 5.4(c), we compare the measured frequencies $\omega_{(1,0)}$ to the predictions of Ref. [29] for the TF limit and for the mean-field quantum Hall regime. For $\tilde{\Omega} < 0.98$ ($\Gamma_{LLL} > 3$), the frequency $\omega_{(1,0)}$ follows the prediction for the TF regime, whereas by $\tilde{\Omega} = 0.990$ ($\Gamma_{LLL} = 1.5$), $\omega_{(1,0)}$ has dropped to close to the prediction for the LLL, thus providing evidence for the cross-over to the lower shear modulus C_2 predicted for the LLL.

While we are able to produce clouds with Γ_{LLL} measured to be substantially lower than $\Gamma_{LLL} = 1.5$, we are unable to accurately measure Tkachenko frequencies under these extreme conditions, due at least in part to the very weakness of C_2. The Tkachenko mode frequencies become so low that it takes multiple seconds to track even a quarter oscillation [figure 5.4(a),(b)]. Concurrently, the very weak shear strength means that even minor perturbations to the cloud can cause the lattice to melt and the individual cores to lose contrast[4] in a matter of seconds. These perturbations can result from residual asymmetry of the magnetic trapping potential, or from spatial structure in the optical beam used to reduce the atom number, or perhaps from thermal fluctuations. In contrast, for a "stiff" cloud of 3×10^6 atoms at $\tilde{\Omega} = 0.95$ ($\Gamma_{LLL} \approx 7$) we observe that the lattice remains ordered, and $\tilde{\Omega}$ can be kept constant, over the entire $1/e$ lifetime of the BEC (≈ 3 minutes).

[4] Melting and loss of contrast are also reported in Ref. [93].

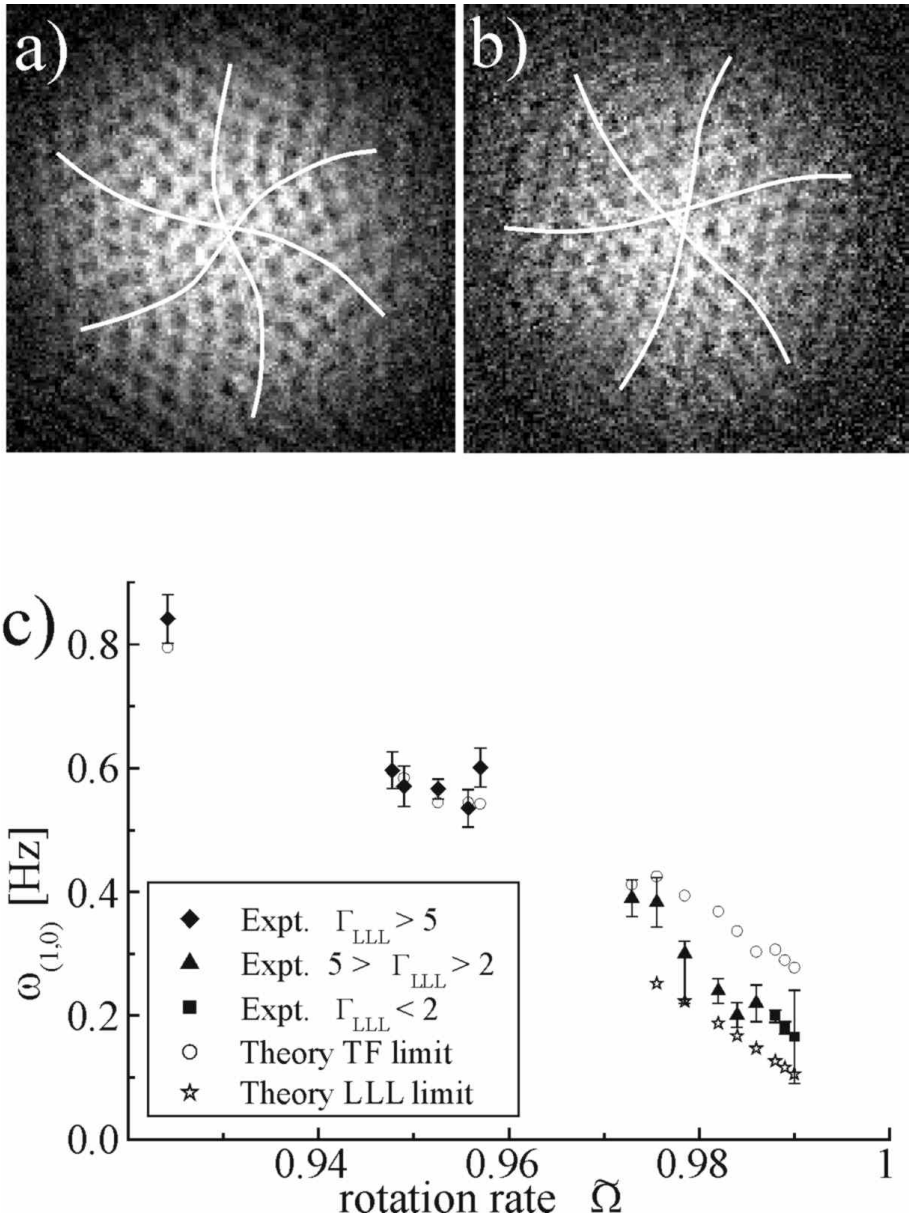

Figure 5.4: (a), (b) Tkachenko mode at $\Gamma_{LLL} = 1.2$ ($N = 1.5 \times 10^5$, $\tilde{\Omega} = 0.989$): (a) directly after excitation, (b) after 1 sec - the lattice oscillation has not yet completed 1/4 cycle. (c) Comparison of measured Tkachenko mode frequency $\omega_{(1,0)}$ (solid symbols) vs. $\tilde{\Omega}$ to theory, using vortex lattice shear modulus C_2^{TF} in the Thomas-Fermi (TF) limit (circles), and C_2^{LLL} in the mean-field quantum Hall regime (stars). Note that both N and Γ_{LLL} decrease as $\tilde{\Omega}$ increases. For $\Gamma_{LLL} \approx 3$ (reached at $N = 7.8 \times 10^5$, $\tilde{\Omega} \approx 0.978$) the data cross over from the TF to the quantum Hall prediction.

5.5 Fractional core area

The fractional condensate area occupied by the vortex cores, as one approaches the lowest Landau level, is also a quantity that has been of much theoretical interest [19, 36, 45, 46]. It is argued by Fischer and Baym [19] and Baym and Pethick [36] that the fractional core area reaches a limiting value as one enters the LLL regime. A corollary to this argument is that fractional core area is a reasonable way to monitor the transition to the lowest Landau level regime. We examine this saturation with experimental and numerical work, which we can push further into this regime than we can achieve experimentally. Additionally we examine some of the systematic errors that can affect the experimental data. To this end numerical calculations were performed as previously described (§2.6), for 3×10^6,5×10^5,and 1×10^5 atoms, and for rotations ranging from Ω/ω_ρ =0.15 to 0.998. For the experimental data, actual condensates were generated over a similar range with Ω/ω_ρ =0.15 to 0.98 and N=$4 - 50 \times 10^5$. The numerical data as well as the experimental data are fit in the same manner as described in §2.3.

We define the fractional area, $\mathcal{A}$, occupied by the vortices to be $\mathcal{A} = n_v \pi \mathrm{r}_v^2$, where n_v is the areal density of vortices and r_v^2 is the 2D RMS vortex core radius. To determine a theoretical value for r_v, we perform a numerical simulation of the Gross-Pitaevskii (GP) equation of a BEC containing an isolated vortex. We obtain $r_v = 1.94 \times \xi$ with $\xi = (8\pi na)^{-\frac{1}{2}}$, where a is the scattering length and n is the density [5] .

Ignoring density inhomogeneity effects (discussed later), and in the limit of many vortices, the expected vortex density n_v is $m\Omega/(\pi\hbar)$. The resulting prediction for $\mathcal{A}$ can be expressed as $\mathcal{A} = 1.34 \times \Gamma_{LLL}^{-1}$. This value exceeds unity for $\Gamma_{LLL} < 1.34$, which has led to the prediction that vortices should merge as the condensate enters the LLL

[5] The density $n = 7/10\, n_{peak}$ is density-weighted along the rotation axis and is radially averaged over the vortex cores within 1/2 the TF radius, as it is only in this region that we fit the observed vortex cores.

regime. An alternate treatment from Baym and Pethick [36] predicts that $\mathcal{A}$ saturates at 0.225 as the vortices go from a Thomas-Fermi profile to the profile of a LLL wave function. Our numerical data for $\mathcal{A}$, together with experimental points, are plotted in figure 5.5 (a,b). For $\Gamma_{LLL}^{-1} < 0.1$, the data agree reasonably well with the Thomas-Fermi result. For larger Γ_{LLL}^{-1}, the data clearly show a smooth transition to the LLL regime, and a saturation of $\mathcal{A}$ at the LLL limit.

The experimental data in figure 2.8(b) tend to lie above the numerical data. This is likely due to the fact that there are many systematic errors that tend to bias the data toward larger core size. Consequently, we tend to overestimate the core size. Of all the systematic errors we have studied, axial expansion of the cloud during the expansion process is by far the most prevalent. Figure 2.8(c) demonstrates the dangers of axial expansion in this measurement. For the data presented, the condensate undergoes a factor of 2-3 in axial expansion, and we see a corresponding increase in $\mathcal{A}$. This clearly illustrates the importance in suppressing axial expansion for these measurements. It is interesting to note that with our rapid axial expansion the fractional core area can overshoot the LLL limit, which in principle should still be valid in the limit of adiabatic expansion.

5.6 Vortex core density profile

We can also observe the transition to the LLL regime in the numerical data by examining the shape of the condensate vortex cores. In the Thomas-Fermi regime, the vortex-core density profile is well described by the form $n(r) = (r/\sqrt{2\xi^2 + r^2})^2$ [94], where r is measured from the vortex center. Alternatively in the LLL regime, the core is no longer dictated by the interactions but rather by kinetic energy considerations. In this case, within the Wigner-Seitz unit cell, the vortex is thought [36] to have a simple oscillator p-state structure $n(r) = ((Cr/b) \cdot exp[-r^2/2l^2])^2$ for $0 \leq r \leq l$, where C is a normalization constant, and l is the radius of the Wigner-Seitz unit cell and is

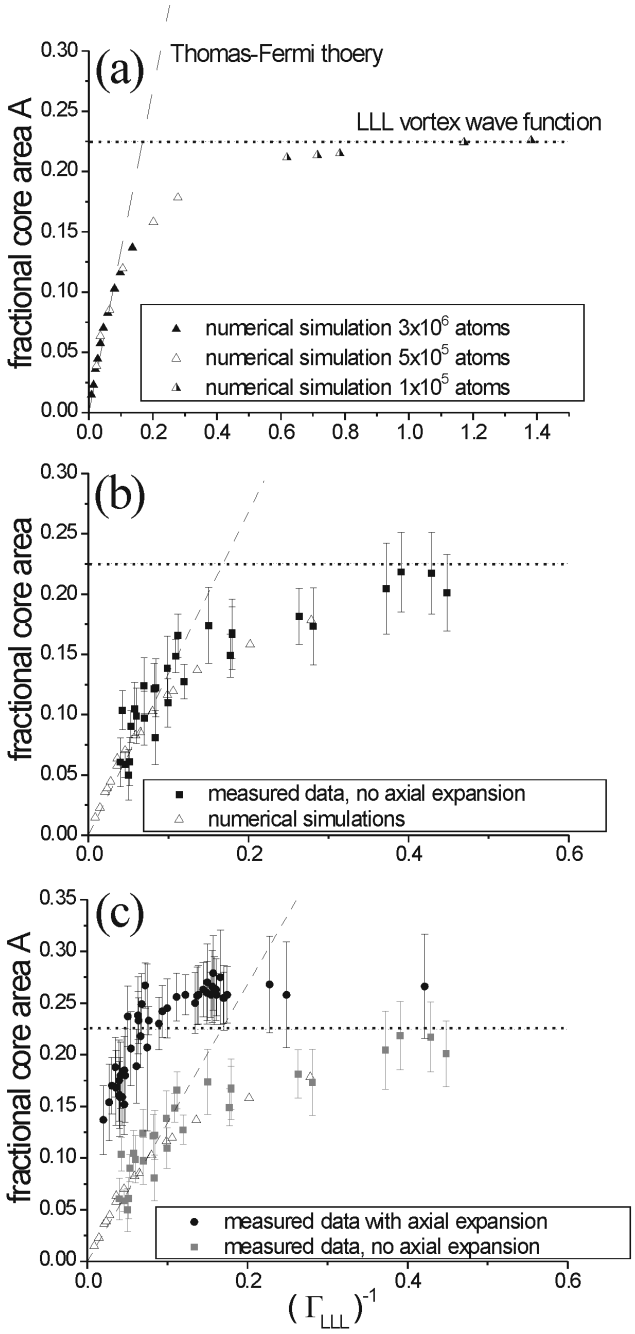

Figure 5.5: Fractional condensate area occupied by vortex cores ($\mathcal{A}$) as a function of $\Gamma_{LLL}^{-1} = 2\hbar\Omega/\mu$, the inverse lowest Landau level parameter. Plot (a) shows a smooth transition in the numerical data from the Thomas-Fermi limit where $\mathcal{A}$ is linear in Γ_{LLL}^{-1} to the LLL limit where $\mathcal{A}$ saturates. Here the Thomas-Fermi theory is represented by the dashed line and the LLL limit by the dotted line. Plot (b) is a comparison of the numerical data to experimental data. Plot (c) demonstrates the effect on the experimental measurement of allowing the condensate to expand axially during the expansion process.

related to the nearest-neighbor lattice spacing b by $l = (\sqrt{3}/2\pi)^{1/2}b$. Figure 5.6 is a comparison of the central vortex, in three numerically generated condensates, to both Thomas-Fermi and LLL predicted core shapes. The simulation for figure 5.6(a) was performed for 3×10^6 atoms and $\Omega/\omega_\rho = .15$ and is well inside the Thomas-Fermi regime ($\Gamma_{LLL} = 117$). Here the density profile of the numerical data (solid line) seems to fit quite well to the Thomas-Fermi vortex form (dotted line), but the LLL form is a poor description of the vortex core (dashed line). The simulation for figure 5.6(b) was performed for 5×10^5 atoms, $\Omega/\omega_\rho = .95$ and $\Gamma_{LLL} = 3.6$. One can see from figure 5.5 that this is in the transition region. Not surprisingly both vortex forms fit about equally well. In Figs. 5.6(b) and figure 5.6(c), the vertical line represents the edge of the Wigner-Seitz unit cell at $r = l$. The simulation for figure 5.6(c) was performed with 1×10^5 atoms, $\Omega/\omega_\rho = .998$ and $\Gamma_{LLL} = .72$. One can see that LLL is a much better description of the vortex.

5.7 Condensate radial density profile

On a separate but interesting note, as we enter the LLL regime, our numerical solution of the GP equation shows that the radial profile of the overall smoothed condensate fits much better to a parabola than to the Gaussian that was originally predicted [35]. We can also confirm this experimentally by imaging clouds with Γ_{LLL} as small as 0.6. Images are taken in-trap, to increase signal, and after 3 sec equilibration time. Examining the radial density profile we find that these images also fit better to a TF profile than to a Gaussian, showing no signs of a cross-over in the radial density profile as the LLL is entered.

The reason the Gaussian-density-profile prediction fails to pan out can be extrapolated from data presented in the next chapter. The density-profile prediction for the radial profile in the LLL arose from an elegant argument that was based on an assumption that the vortex nodes were on a perfect triangular lattice. As was originally pointed

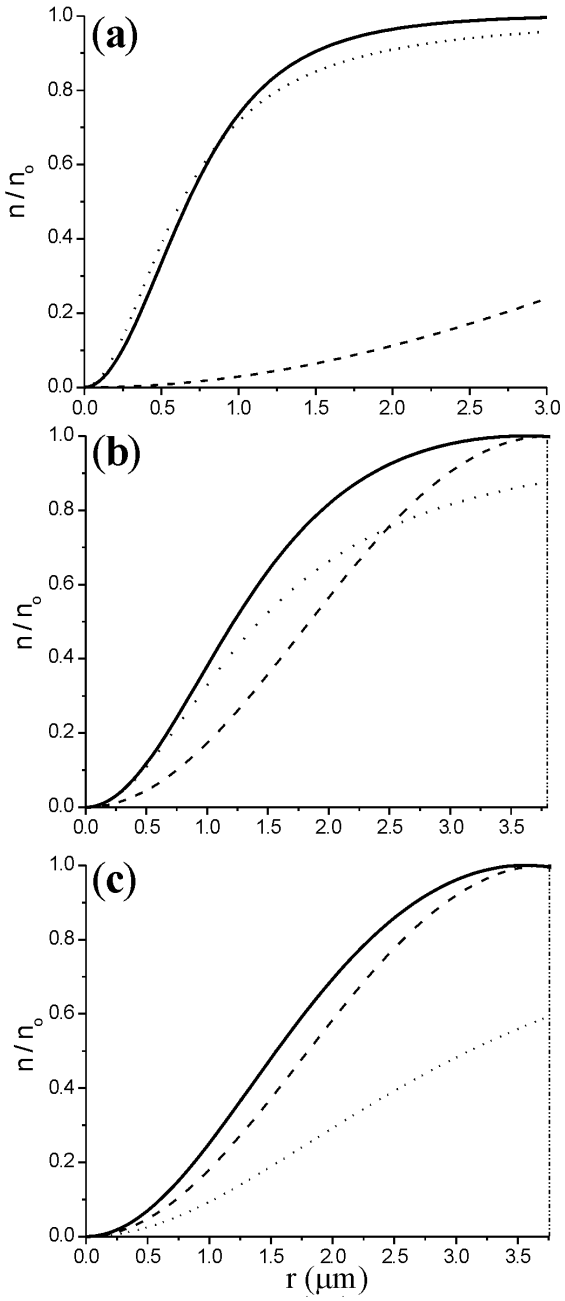

Figure 5.6: Numerically generated vortex core density profiles approaching the lowest Landau level regime. Density n is scaled by the peak debsity n_0. Solid lines represent the numerical result for (a) $\Gamma_{LLL} = 117, (b)\Gamma_{LLL} = 3.6, (c)\Gamma_{LLL} = .72$. The dashed line is the expected profile for a LLL wave function [36] given the condensate rotation. The dotted line is the expected vortex form in the Thomas-Fermi limit [94] given the condensate density. The vertical lines in figure (b) and (c) designate the edge of the Wigner-Seitz unit cell. As Γ_{LLL} decreases, one can see a clear transition from the interaction-dominated Thomas-Fermi regime to a LLL function where kinetic energy concerns and the vortex core spacing dictate the shape and size of the vortex.

out to us by A. H. MacDonald [43] and has been the subject of two recent theoretical works [41, 42], a slight radially dependant perturbation in the areal density of vortices is enough to convert a Gaussian density distribution into an inverted parabola. The analytic description of this perturbation in [41] (calculated in the LLL) bears a striking resemblance to the one measured in §6.2 in the Thomas-Fermi regime and also to the analytic form [44] calculated in the Thomas-Fermi regime. The surprising result of this perturbation in the areal density of vortices is that one of the most striking features of the Thomas-Fermi regime, the parabolic Thomas-Fermi density profile, still exists in the LLL regime where the condensate kinetic energy is clearly non-negligible compared to interaction energy.

Chapter 6

Experimental studies of equilibrium vortex properties in a Bose-condensed gas [1]

6.1 Introduction

After the initial observations of vortex lattices in Bose-Einstein condensed gases [22, 24, 25, 23], most of the experimental work has focused on dynamical behavior of vortices and lattices, including Kelvons [77, 95, 96], Tkachenko waves [28, 84, 29, 83, 31, 85, 33, 86, 32], and various nonequilibrium effects [71, 76]. Equilibrium properties, in contrast, have been relatively neglected by experimenters. This imbalance is not indicative of a lack of interesting physics in equilibrium behavior, but simply reflects the usual experimentalist's preference for measuring spectra rather than static structure. Theorists, on the other hand, have investigated equilibrium properties extensively [36, 44, 45, 94, 46, 35, 89, 97, 98, 41, 42, 99, 19], and our purpose in this chapter is to partially redress this imbalance with a series of experimental studies focusing on equilibrium properties of rotating condensates.

The vortex lattice in a rotating Bose-condensed gas naturally organizes into a regular triangular lattice, or Abrikosov lattice, originally observed in superconductors. The lattice can be well characterized by the nearest-neighbor lattice spacing and by the radius of each vortex core (b and r_v, respectively). The nearest-neighbor lattice spacing, b, is generally thought to be determined only by the rotation rate when in the high-rotation regime where the rotating BEC exhibits nearly rigid-body behavior. Nu-

merical work [45] and early analytical work [28], however, suggests that this rigid-body assumption yields lattice constants that are smaller than would be seen in the case of a finite-size trapped BEC. Recent work by Sheehy and Radzihovsky [44] has tackled this discrepancy analytically and found it to be a necessary consequence of the inhomogeneous density profile of the condensate. With this theory they address the question of why the lattice is so remarkably regular given the condensate density profile. They also derive a small, position-dependent, inhomogeneity-induced correction term to the lattice spacing. An interesting implication of this theory is that the vortices must move slightly faster than the surrounding superfluid even near the rigid-body limit. More striking still is the prediction that the superfluid should exhibit a radially-dependant angular velocity (or radial shear flow), which directly follows from their calculation of inhomogeneous vortex density. While a differential rotation rate is not directly observable in our system, the position-dependent variation of the nearest-neighbor lattice spacing is studied in §6.2. It should also be noted that the inhomogeneity in the areal density of vortices, predicted in Ref. [44], can also be derived in the limit of the lowest Landau level (LLL). This property of the LLL was first brought to our attention by A.H. MacDonald and has been the subject of two recent publications by Watanabe **et al.** [41] and Cooper **et al.** [42].

The second effect we study in this chapter concerns the core size of the vortices. Once rotation rate and density are fixed, the vortex core size is a length scale that the condensate chooses on its own. In this sense vortex core size constitutes a fundamental property of the system and has therefore been the subject of much theoretical work [94, 97, 98]. By analogy to superfluid ^{4}He, the core size is dictated by the atomic interactions and is of order of the healing length. For our system the healing length is only one and a half times the average interatomic spacing. As a result of this diluteness one might wonder if there are certain regimes of sufficiently low or high density where one would see a deviation from mean-field theory. Investigation of core size makes up §6.3.

Finally in §6.4 we examine the proposal that a measurement of the contrast of vortex cores could serve as a sensitive thermometer for a condensate in the regime for which the temperature is less than the chemical potential and other methods of thermometry become unreliable. We discuss our preliminary efforts to realize this vision. We are able to see an effect, but we have not yet been able to extend this measurement technique below the usual limits.

Note that our original paper on equilibrium effects [100] also contained a section examining the rotational suppression of quantum degeneracy. A description of this effect can be found in the thesis of Paul Haljan [54] or in [100].

6.2 The lattice constant

At first sight, vortex lattices, such as the one seen in figure 2.8(b), appear perfectly regular. However as noted in the introduction, Sheehy and Radzihovsky [44] predict that there should exist a small correction to the vortex density in the condensate due to the condensate, density inhomogeneity. One result from Ref. [44] is that the areal density of vortices is

$$n_v(\rho) = \frac{\Omega m}{\pi\hbar} - \frac{1}{2\pi R_\rho^2(1-(\rho/R_\rho)^2)^2} ln[\hbar/(2.718\, m\Omega\xi^2)] \ , \tag{6.1}$$

where m is the mass of rubidium and ξ is the healing length (calculated from the measured density). This equation can conveniently be thought of as the rigid body rotation (first term) plus the density inhomogeneity correction that reduces vortex density. We compare to experimental measurements by converting vortex density to a nearest-neighbor lattice spacing, conveniently expressed in units of condensate radius

$$b(\rho) = \sqrt{2/(3^{1/2} n_v(\rho))}\frac{1}{R_\rho} \ . \tag{6.2}$$

To study this lattice inhomogeneity effect experimentally, we generate condensates with rotation rates between $\Omega/\omega_\rho = 0.5 and 0.9$. To extract the vortex separation,

we expand the cloud by a factor of 10 in the radial direction using the anti-trapped expansion technique. The condensate and vortices are fit as described in §2.3. The nearest-neighbor separation for a given vortex is measured by averaging the distance from the vortex center to the centers of the six nearest vortices. Due to low signal, vortices further than 0.9 R_ρ from the condensate center are disregarded. Any remaining vortex with fewer than six nearest neighbors (i.e., a vortex in the outer ring) is used as a neighbor to other vortices but is not itself included in the final data. Obviously using the six nearest neighbors assumes a triangular lattice structure, so before fitting, each image is checked for defects in the lattice. Any image exhibiting broken lattice planes is not considered. Once the nearest-neighbor separation is measured, it is normalized by the expanded condensate radius to compare to equation 6.2. For this comparison, R_ρ, Ω, and ξ are measured or calculated from an in-trap image. To improve the theory fit, we allowed R_ρ to float, but, in each case, the fit value for R_ρ was within 5% of the measured value. Noise is suppressed by binning the lattice-spacing data by radial displacement of the vortex from the center.

Figure 6.1 shows a comparison to theory for three physical condensates and one numerically generated condensate density profile. Figure 6.1(a) is data taken from the condensate in figure 2.8(a). The two points shown correspond to the measured vortex density for the center vortex (first point) and the average vortex density for the first ring of vortices. Also plotted is equation 6.2 (solid line) and the expected nearest-neighbor lattice spacing for rigid body rotation (dashed line). The imperfect fit may be partly due to the discrete nature of the data, vis-a-vis a continuum theory [44]. Plots (b) and (c) are condensates with increasing rotation rates where (c) is taken from image 2.8(b). Plot (d) is a comparison with numerical data prepared with parameters similar to the experimental situation in (c). Figure 6.1(e) is the same data in figure 6.1(c) but plotted without the suppressed zero to emphasize the smallness of the position dependant effect. The areal density of vortices is constant to 2% over a region that experiences an atom-

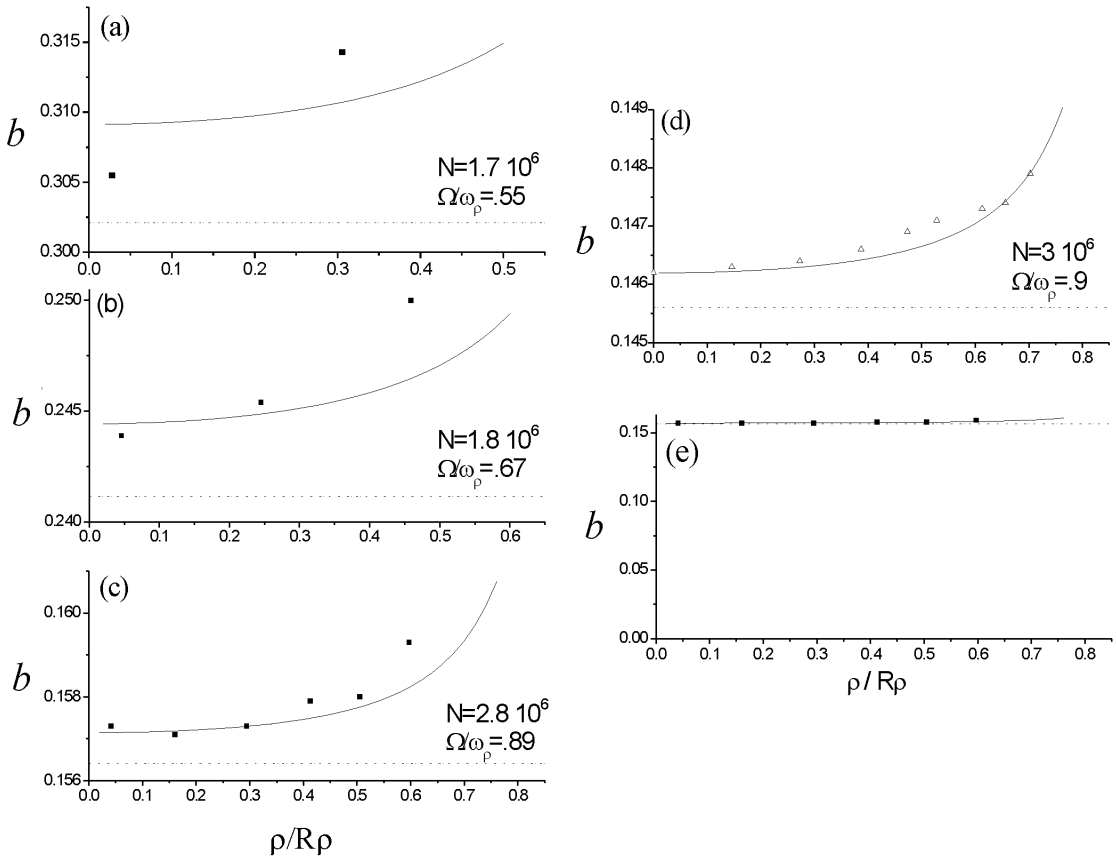

Figure 6.1: Measured and binned lattice spacings as a function of radial position ρ. The solid curve is the theory result (equation (6.2)) of Sheehy and Radzihovsky [44]. The rigid-body–rotation rate lattice spacing is also plotted for comparison (dashed line). Plots (a-c) are experimental data with increasing rotation. Plot (a) and (c) are data taken from the condensate in Figs. 2.8(a) and (b), respectively. Plot (d) is the same effect observed in the numerical data. One can see that theory and experiment show a similar dependence on radial position and that the fractional amplitude of the density inhomogeneity effect is suppressed at higher rotation. Plot (e) is the data in (c) plotted without suppressing the zero. The vortex lattice spacing changes less than 2% over a region in which the atom density varies by 35%.

density variation of 35%.

6.3 Vortex core size

The other defining length scale of the vortex lattice is the core radius. Here we study the core radius in the Thomas-Fermi regime (as opposed to the lowest Landau level regime, described later) where it should scale with the healing length. A theoretical value for the vortex core radius was generated by performing a numerical simulation for a 3D BEC containing an isolated vortex and comparing the fitted radius of this vortex to the corresponding healing length. Fitting the simulation in the same manner that we later treat the experimental data (described in §2.3) we obtain an expression for the core radius of

$$r_v = 1.94 \times \xi \ , \tag{6.3}$$

with healing length $\xi=(8\pi n a_{sc})^{-1/2}$, where a_{sc} is the scattering length and n is the density-weighted atom density. For the data presented, n is determined from the in-trap image before expansion.

Core size measurements and fractional core area (discussed in the next subsection) measurements require considerable attention to detail. In pursuing these measurements, we find that nearly everything — from focusing issues, to lensing due to off resonant imaging light, to even imperfect atom transfer into the anti-trapped state before expansion — can lead to an overestimation of the vortex core size. By far the biggest potential systematic error in our system is axial expansion, which, as noted in §2.3, requires careful attention.

A range of core sizes is achieved by varying the initial number of atoms loaded into the magnetic trap prior to evaporation. To avoid the core size saturation effect, due to high condensate rotation [36], we consider only clouds with $\Gamma_{LLL} > 10$, where $\Gamma_{LLL} \equiv \mu/(2\hbar\Omega)$ is the LLL parameter and μ is the chemical potential. This ratio of

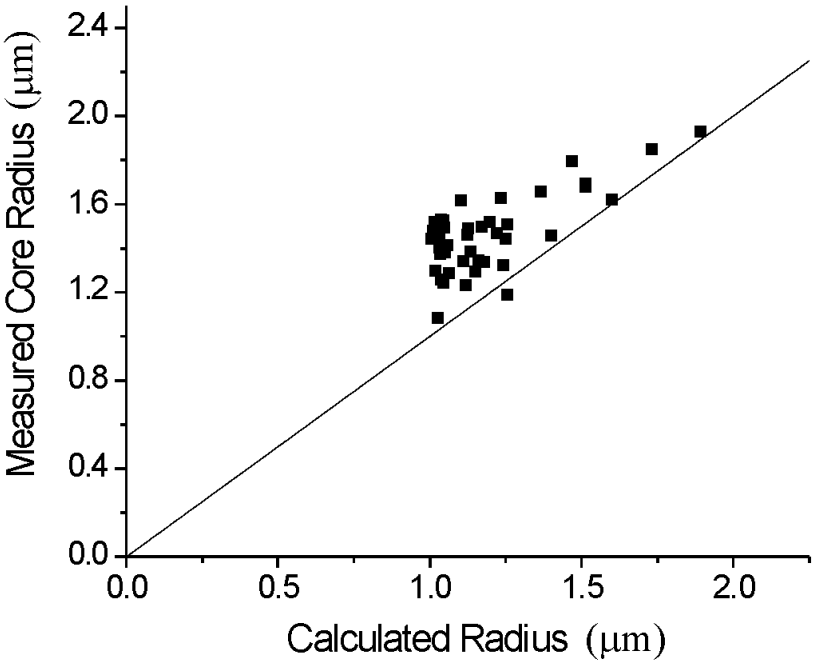

Figure 6.2: Comparison of measured core radii with the Thomas-Fermi prediction (equation (6.3)) represented by the solid line. Black squares are the core size in expansion scaled by the radial expansion of the condensate so that they correspond to the in-trap values. Data shows reasonable agreement with theory. The fact that the measured core size is consistently larger is likely due to the fact that nearly all our imaging systematics lead to an overestimation of the vortex core size.

chemical potential to rotational energy approaches unity as we enter the LLL regime, while at values of 10 or greater we should be firmly in the Thomas-Fermi regime. In practice this requires only that we keep the condensate rotation rate low. Core size is measured by fitting the expanded image with a Thomas-Fermi profile and each core with a 2D Gaussian. For figure 6.2 the measured core radius in expansion is scaled back to the corresponding in-trap value using the radial expansion factor discussed in §2.3. To reduce scatter we consider only vortices located less than half a condensate radius out from the center. Additionally we find that some vortices appear to have some excitation or bending which leads to a poor fit. To filter these out we consider only vortices that have a contrast greater than 0.6. Here contrast is defined, with respect to the integrated (along the line of sight) condensate profile, as the peak of the "missing" column density at the vortex position divided by the smoothed Thomas-Fermi profile at the same position.

From figure 6.2 we can see that the data and the Thomas-Fermi theory agree reasonably well. The data do seem to be slightly above the theory value, but we are hesitant to make too much of this because, as noted before, there are many systematic errors that tend to bias the data toward larger core size. Measurement is easier and the agreement better, on the low density, large-core side of the graph.

At an early stage in this work, we speculated that the mean-field Gross-Pitaevskii equation might not give a good quantitative description of vortex core size because the core size is particularly sensitive to the healing length ξ. At our highest densities, while the gas is nominally dilute ($na_{sc}^3 < 10^{-5}$, where a_{sc} is the interatomic scattering length), the mean interatomic distance $n^{-1/3}$ is only a factor of 1.5 less than ξ. Our data, however, do not support this hypothesis. The roughly 25% discrepancy between our measurements and the mean-field prediction shown in figure 6.2 is comparable to possible systematic errors in our measurements of the smaller cores that exist at high densities. In retrospect, our experimental design is such that we are unlikely to be able

to see a mean-field failure even if one were to exist. During the radial expansion, the density drops. Thus the accuracy of the mean-field approximation is likely to improve significantly during the expansion. Our anti-trapped expansion, while more rapid than a conventional ballistic expansion, is still slow compared to the rate at which a vortex can adiabatically relax its radius [36] (approximately $\mu/\hbar$). Any non-mean-field corrections to the vortex core size will likely relax away before the cores have expanded to be large enough for us to reliably image them.

6.4 Core contrast and condensate temperature

Since the very first observations of dilute-gas BEC, the temperature of the sample has been determined by imaging the "skirt" of thermal atoms that extends beyond the radius of the condensate. In practice, it is difficult to extend this measurement below about $T/T_c = 0.4$, except in very special cases (for instance when a Feshbach resonance is used to set the scattering length to zero). For low temperatures, the density of thermal atoms becomes so low that they are difficult to image. Moreover, when the temperature becomes lower than or comparable to the chemical potential of the self-interacting condensate, the spatial extent of the thermal cloud is no longer appreciably larger than the condensate itself.

It was suggested that vortex cores might serve as "thermal-atom concentration pits", in order to enhance thermometry at low temperatures. In a simple Hartree-Fock (HF) picture of the interaction between thermal atoms and the condensate, the condensate density represents a repulsive interaction potential to the thermal atoms. Along the nodal line of a vortex core, the condensate density and presumably its repulsive interaction potential vanish. Thus, the thermal atoms would experience the lowest combined interaction and magnetic potential within the cores of vortices. As a result, their density would be highest there. Additionally, images of thermal atoms in the vortex core could be taken against a vanishing background condensate density. Moving

beyond the HF approximation, one finds a more complicated picture. The Bogoliubov spectrum of very long wave-length thermal phonons extends all the way down to the chemical potential. One should contrast this energy with the energy of a thermal atom confined to a vortex core. Perhaps the atom experiences no interaction energy. However, the kinetic energy cost of bending its wave function to fit inside a core with a radius of the order of healing length must, by definition, be comparable to the chemical potential. In the limit of very elongated vortex cores, there can be very low-energy, core-bending modes [77, 101]. Thermal excitations of these modes would manifest as a temperature-dependent contrast ratio. We expect this effect is unlikely to be important in the relatively flattened geometry of our highly rotating condensates. In any case, without more rigorous analysis, it is not easy to predict how the contrast ratio of our vortices should vary with temperature, but we nonetheless set out to do a preliminary study of the effect.

We vary the final condensate temperature by changing our rf-evaporation end point. This produces a cloud with temperatures between $5 - 50\ nK$ or T/T_c between 1 and less than 0.4. Here T_c is calculated from the trap frequencies and a measurement of total atom number using the formula $T_c = 0.94\hbar\tilde{\omega}_{ho}N^{1/3}$, where $\tilde{\omega}_{ho}$ has been adjusted for rotation according to the equation $\tilde{\omega}_{ho} = \omega_{ho}(1 - \Omega^2/\omega_\rho^2)^{1/3}$. When possible, T is extracted from a two-component fit to the in-trap image. Because our rotation rate and temperature are linked through the 1D evaporative process, it is unavoidable that Ω also varies during the data set.

To measure core contrast, we expand the cloud using the usual expansion procedure. The atom cloud is expanded radially by a factor of 13 to ensure that the cores are large compared to our imaging resolution. However, because we no longer care about the precise core size we do not suppress the axial expansion. Additionally, the axial expansion actually reduces background fluctuations in the measured core contrast. With a factor of two axial expansion, cores become much rounder and clearer as shown

in figure 2.8(c). These changes allow us to achieve a higher core contrast and quieter signal than we can without expansion.

The term core brightness (1-contrast ratio) will be our metric for this experiment. We define core brightness ($\mathcal{B}$) as $n_{2D}(core)/n_{2D}(cloud)$, where $n_{2D}(core)$ is the observed atom density, integrated along the line of sight, at the core center, and $n_{2D}(cloud)$ is the projected integrated atom density at the same point, based on a smoothed fit to the overall atom cloud. To determine $n_{2D}(cloud)$, we fit the condensate image to a Thomas-Fermi profile and the surrounding thermal atoms to a Bose distribution. We find $n_{2D}(core)$ by fitting each vortex with a Gaussian to determine its center and then averaging five pixels around the center point to determine the integrated density. Brightness is calculated for each vortex and then averaged with other vortices in the cloud. To suppress noise from low signal, vortices further than 0.4 R_ρ from the condensate center are disregarded for this measurement. The $n_{2D}(core)$ term necessarily contains signal from the surrounding thermal atoms because the vortices do not penetrate the thermal component. Thus, one expects to see a steady decrease in $\mathcal{B}$ with decreasing temperature, as atoms not necessarily in the vortex core, but still in the integrated line of sight, disappear. One would hope that $\mathcal{B}$ continues to decrease even for T/T_c below 0.4 for this analysis to be a viable means of extending condensate thermometry.

We are in the awkward position of comparing our core contrast measurement to a temperature measurement that, as previously described, is expected to fail at low temperatures. To monitor this failure, we calculate a simplistic core brightness ($\mathcal{B}_{simple}$) by comparing the fitted in-trap condensate and thermal cloud profiles. Here $\mathcal{B}_{simple} \equiv \tilde{n}_{2D}(thermal)/(\tilde{n}_{2D}(condensate) + \tilde{n}_{2D}(thermal))$ where $\tilde{n}_{2D}(condensate)$ and $\tilde{n}_{2D}(thermal)$ are the smoothed condensate and thermal cloud profiles integrated along the z-axis and averaged over a region of radius less than 0.4 R_ρ from the condensate center. The term $\mathcal{B}_{simple}$ can be thought of as the core brightness one would expect based on the undoubtedly false assumption that the condensate and thermal atoms do

not interact. It is interesting to compare $\mathcal{B}$ to $\mathcal{B}_{simple}$ since this same dubious assumption is implicit in the standard thermometry technique of fitting the thermal "skirt".

In figure 6.3, $\mathcal{B}$ and $\mathcal{B}_{simple}$ are plotted versus the final evaporative cut. For our experiment, the thermal cloud can be reliably fit for $T/T_c > 0.6$ and less reliably fit for $T/T_c > 0.4$. In both these regions T/T_c decreases continuously with lower final evaporative cut. It is assumed that for T/T_c just below 0.4, this trend continues. For reference, three values of T/T_c (measured from the thermal "skirt") are included in the plot. One can see that $\mathcal{B}$ does steadily decrease with lower temperature for $T/T_c > 0.4$. It is interesting to note that $\mathcal{B}_{simple}$ closely tracks $\mathcal{B}$ at the higher temperatures and then diverges from $\mathcal{B}$ as the cloud gets colder. Presumably, this divergence occurs because thermal atoms are pushed away from the condensate center as interactions between the condensate and the thermal cloud become important. The fact that $\mathcal{B}_{simple}$ diverges upwards is likely due to the tendency of our fitting technique to overestimate the thermal cloud density at high condensate fractions. The failure of $\mathcal{B}_{simple}$ at low temperatures also throws into suspicion the quoted T/T_c since they are determined from the same two-component fit.

In contrast, as $\mathcal{B}_{simple}$ begins to fail, $\mathcal{B}$ continues its previous smooth downward trend. It is also interesting to note that at an rf of 2.35 MHz, we see a $\mathcal{B}$ of 0.13-0.15, which is not that far off from the work of Virtanen **et al.** [98] who predict that atoms trapped in the core would lead to a $\mathcal{B}$ of 0.1 at a T/T_c of 0.39. Unfortunately, our efforts to observe a $\mathcal{B}$ of less than 0.125 have failed so far, as can be seen from the data points at 2.3 MHz in figure 6.3. This limit impedes our ability to measure temperatures colder than 0.4 T/T_c. Currently, it is unclear what the source of this limit is. Perhaps the same imaging systematics that make our vortex radius unreliable at the 10% level are also preventing us from seeing a core brightness level less than 0.13, or a very slight tilt of the vortices may occur during expansion.

As a caveat to the previous discussion, the same limitations that inhibit conden-

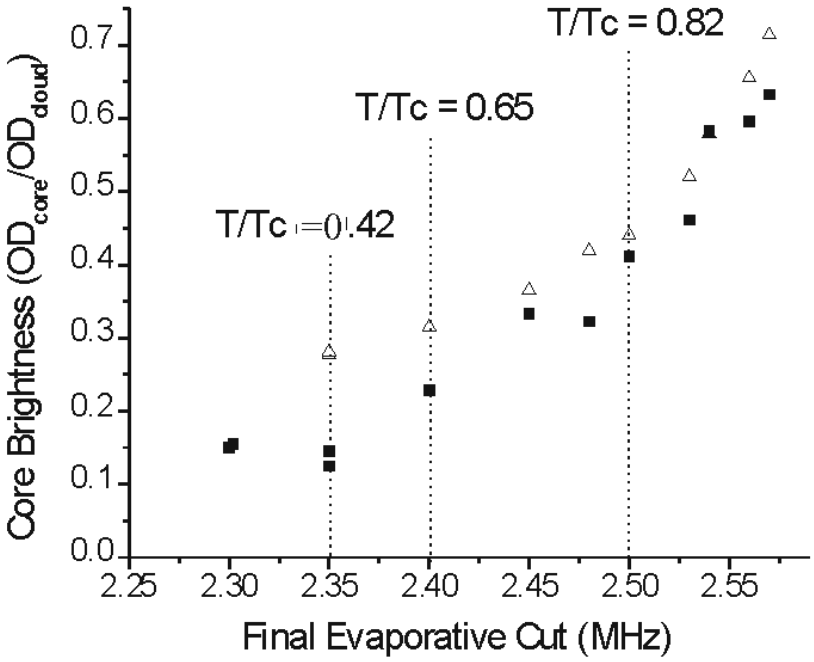

Figure 6.3: Measured core brightness as a function of final rf evaporative cut. Within our ability to measure, T/T_c decreases continuously with the rf frequency. For the black squares brightness ($\mathcal{B}$) is defined as the 2D atom density at the vortex core divided by the 2D atom density of the overall smoothed condensate plus thermal cloud profile at the same point. For the open triangles a simplistic brightness ($\mathcal{B}_{simple}$) is calculated from the ratio of the 2D atom density of the thermal cloud to the 2D atom density of the overall smoothed condensate and thermal cloud profile. At high temperatures $\mathcal{B}$ and $\mathcal{B}_{simple}$ exhibit a clear dependance on the final rf cut. At lower temperatures it is encouraging that as $\mathcal{B}_{simple}$, begins to fail $\mathcal{B}$ is still continuing a smooth trend downward. Disappointingly at very low temperatures, $\mathcal{B}$ plateaus at about 0.14.

sate thermometry below T/T_c of 0.4 will also reduce the efficacy of evaporative cooling in the same regime. Additionally, the already inefficient 1D nature of our evaporation would exacerbate such a cooling problem. Perhaps the simplest explanation for the failure of $\mathcal{B}$ to decrease with very deep rf cuts is that the condensate fraction is no longer increasing. One could imagine that our measured $\mathcal{B}$ is faithfully following the temperature we achieve.

In summary, the conclusions of our preliminary attempt to extend thermometry with core brightness are encouraging but ambiguous. New ideas are needed before we can make further progress.

Bibliography

[1] this chapter/section is a revised version taken from [100].

[2] this chapter is a revised version of [76].

[3] this chapter is a revised version of [84].

[4] this chapter is a revised version of [102] and [100].

[5] S. Bose, Z. Phys. **26**, 178 (1924).

[6] A. Einstein, Sitzungber. Preuss. Akad. Wiss. **1925**, 3 (1925).

[7] F. London, Phys. Rev. **54**, 947 (1938).

[8] F. London, Nature **141**, 643 (1938).

[9] T. Guenault, Basic Superfluids (Taylor and Francis Group, New York, 2003).

[10] J. S. Tsakadze and S. J. Tsakadze, J. Low Temp. Phys. **39**, 649 (1980).

[11] G. Baym, R. Epstein, and B. Link, Physica B **178**, 1 (1992).

[12] M. Greiner, C. A. Regal, and D. S. Jin, Nature **426**, 537 (2003).

[13] S. Jochim *et al.*, Science **302**, 2101 (2003).

[14] M. W. Zwierlein *et al.*, Phys. Rev. Lett. **91**, 250401 (2003).

[15] L. Onsager, Nuovo Cimento Suppl. **6**, 249 (1949).

[16] R. P. Feynman, Progress in Low Temperature Physics, Vol. 1 (North-Holland Pub. Co, ADDRESS, YEAR).

[17] U. Essmann and H. Trauble, Physics Letters **24A**, 526 (1967).

[18] E. J. Yarmchuk, M. J. V. Gordon, and R. E. Packard, Phys. Rev. Lett. **43**, 214 (1979).

[19] U. R. Fischer and G. Baym, Phys. Rev. Lett. **90**, 140402 (2003).

[20] M. R. Matthews *et al.*, Phys. Rev. Lett. **83**, 2498 (1999).

[21] B. P. Anderson, P. C. Haljan, C. E. Wieman, and E. A. Cornell, Phys. Rev. Lett. **85**, 2857 (2000).

[22] K. W. Madison, F. Chevy, W. Wohlleben, and J. Dalibard, Phys. Rev. Lett. **84**, 806 (2000).

[23] E. Hodby *et al.*, Phys. Rev. Lett. **88**, 010405 (2001).

[24] J. R. Abo-Shaeer, C. Raman, J. M. Vogels, and W. Ketterle, Science **292**, 476 (2001).

[25] P. C. Haljan, I. Coddington, P. Engels, and E. A. Cornell, Phys. Rev. Lett. **87**, 210403 (2001).

[26] V. K. Tkachenko, Sov. Phys. JETP **23**, 1049 (1966).

[27] C. D. Andereck, J. Chalupa, and W. I. Glaberson, Phys. Rev. Lett. **44**, 33 (1980).

[28] J. R. Anglin and M. Crescimanno, cond-mat/0210063.

[29] G. Baym, Phys. Rev. Lett. **91**, 110402 (2003).

[30] L. O. Baksmaty, S. J. Woo, S. Choi, and N. P. Bigelow, Phys. Rev. Lett. **92**, 160405 (2004).

[31] T. Mizushima *et al.*, Phys. Rev. Lett. **92**, 060407 (2004).

[32] M. Cozzini, L. P. Pitaevskii, and S. Stringari, Phys. Rev. Lett. **92**, 220401 (2004).

[33] E. Sonin, cond-mat/0405474.

[34] l. O. Baksmaty, private communication.

[35] T.-L. Ho, Phys. Rev. Lett. **87**, 060403 (2001).

[36] G. Baym and C. J. Pethick, Phys. Rev. Lett. **69**, 043619 (2004).

[37] N. R. Cooper, N. K. Wilkin, and J. M. F. Gunn, Phys. Rev. Lett. **87**, 120405 (2001).

[38] J. Sinova, C. B. Hanna, and A. H. MacDonald, Phys. Rev. Lett. **89**, 030403 (2002).

[39] B. Paredes, P. Fedichev, J. I. Cirac, and P. Zoller, Phys. Rev. Lett. **87**, 010402 (2001).

[40] M. Cozzini and S. Stringari, Phys. Rev. A. **67**, 041602 (2003).

[41] G. Watanabe, G. Baym, and C. J. Pethick, cond-mat/0403470.

[42] N. Cooper, S. Komineas, and N. Read, cond-mat/0404112.

[43] a. H. MacDonald, private communication.

[44] D. E. Sheehy and L. Radzihovsky, cond-mat/0402637,and cond-mat/0406205.

[45] D. L. Feder and C. W. Clark, Phys. Rev. Lett. **87**, 190401 (2001).

[46] A. L. Fetter, Phys. Rev. A **64**, 063608 (2001).

[47] R. Blaauwgeers *et al.*, Nature **404**, 471 (2000).

[48] M. Baert *et al.*, Europhys. Lett **29**, 157 (1995).

[49] V. Moshchalkov *et al.*, Phys. Rev. B **54**, 7385 (1996).

[50] G. Braverman, S. Gredeskul, and Y. Avishai, Phys. Rev. B **57**, 13899 (1998).

[51] A. E. Leanhardt *et al.*, Phys. Rev. Lett. **89**, 190403 (2002).

[52] P. O. Fedichev and U. R. Fischer, Phys. Rev. Lett. **91**, 240407 (2003).

[53] A. Marte *et al.*, Phys. Rev. Lett. **89**, 283202 (2002).

[54] P. C. Haljan, Ph.D. thesis, University of Colorado (Boulder), 2003.

[55] D. Guery-Odelin and S. Stringari, Phys. Rev. Lett. **83**, 4452 (1999).

[56] O. M. Marago *et al.*, Phys. Rev. Lett. **84**, 2056 (2000).

[57] J. R. Ensher, Ph.D. thesis, University of Colorado (Boulder), 1998.

[58] M. R. Andrews *et al.*, Phys. Rev. Lett. **79**, 553 (1997).

[59] M. R. Matthews, Ph.D. thesis, University of Colorado (Boulder), 1999.

[60] D. Guery-Odelin, Phys. Rev. A **62**, 033607 (2000).

[61] H. J. Lewandowski, D. M. Harber, D. L. Whitaker, and E. A. Cornell, J. Low Temp. Phys. **132**, 309 (2003).

[62] F. Dalfovo and M. Modugno, Phys. Rev. A **61**, 023605 (2000).

[63] Y. Castin and R. Dum, Phys. Rev. Lett. **77**, 5315 (1996).

[64] B. P. Anderson *et al.*, Phys. Rev. Lett. **86**, 2926 (2001).

[65] C. S. Z. Dutton, M. Budde and L. V. Hau, Science **293**, 663 (2001).

[66] K. W. Madison, F. Chevy, V. Bretin, and J. Dalibard, Phys. Rev. Lett. **96**, 4443 (2001).

[67] E. Lundh, Phys. Rev. A **65**, 043604 (2002).

[68] K. Kasamatsu, M. Tsubota, and M. Ueda, Phys. Rev. A **66**, 053606 (2002).

[69] G. M. Kovoulakis and G. Baym, New Journal of Physics **5**, 51.1 (2003).

[70] T. P. Simula, S. M. M. Virtanen, and M. M. Salomaa, Phys. Rev. A **65**, 033614 (2002).

[71] P. Engels, I. Coddington, P. C. Haljan, and E. A. Cornell, Phys. Rev. Lett. **89**, 100403 (2002).

[72] J. R. Abo-Shaeer, C. Raman, and W. Ketterle, Phys. Rev. Lett. **88**, 070409 (2002).

[73] A. L. Fetter, cond-mat/0309204.

[74] A. A. Abrikosov, Sov. Phys. JETP **5**, 1174 (1957).

[75] E. B. Sonin, Rev. Mod. Phys. **59**, 87 (1987).

[76] P. Engels *et al.*, Phys. Rev. Lett. **90**, 170405 (2003).

[77] V. Bretin *et al.*, Phys. Rev. Lett. **90**, 100403 (2003).

[78] A. A. Svidzinsky and A. L. Fetter, Phys. Rev. A. **58**, 3168 (1998).

[79] personal communication with James Anglin.

[80] personal communication with John Toner.

[81] F. Chevy, K. W. Madison, and J. Dalibard, Phys. Rev. Lett. **85**, 2223 (2000).

[82] personal communication with Marco Cozzini and Sandro Stringari.

[83] S. Choi, L. O. Baksmaty, S. J. Woo, and N. P. Bigelow, Phys. Rev. A **68**, 031605 (2003).

[84] I. Coddington, P. Engels, V. Schweikhard, and E. A. Cornell, Phys. Rev. Lett. **91**, 100402 (2003).

[85] S. A. Gifford and G. Baym, cond-mat/0405182.

[86] A. B. Bhattacherjee, Journal of Physics B **37**, 2699 (2004).

[87] G. Baym, cond-mat/0308342.

[88] G. Baym, cond-mat/0408401.

[89] J. Sinova, C. B. Hanna, and A. H. MacDonald, Phys. Rev. Lett. **90**, 120401 (2003).

[90] R. B. Laughlin, Rev. Mod. Phys. **71**, 863 (1999).

[91] R. J. Donelly, Quantized Vortices in Helium II (Cambridge University Press, Cambridge, 1991).

[92] P. Rosenbusch *et al.*, Phys. Rev. Lett. **88**, 250403 (2002).

[93] V. Bretin, S. Stock, Y. Seurin, and J. Dalibard, Phys. Rev. Lett. **92**, 050403 (2004).

[94] A. Fetter, Lectures in Theoretical Physics, Vol. XIB, p. 351 (Gordon And Breach, New York, 1969).

[95] F. Chevy and S. Stringari, Phys. Rev. A. **68**, 053601 (2003).

[96] J. P. Martikainen and H. T. C. Stoof, Phys. Rev. Lett. **91**, 240403 (2003).

[97] T. Isoshima and K. Machida, Phys. Rev. A **59**, 2203 (1999).

[98] S. M. M. Virtanen, T. P. Simula, and M. M. Salomaa, Phys. Rev. Lett. **86**, 2704 (2001).

[99] S. Stringari, Phys. Rev. Lett. **82**, 4371 (1999).

[100] I. Coddington *et al.*, cond-mat/0405240.

[101] P. C. Haljan, B. P. Anderson, I. Coddington, and E. A. Cornell, Phys. Rev. Lett. **86**, 2922 (2001).

[102] V. Schweikhard *et al.*, Phys. Rev. Lett. **92**, 040404 (2004).

[103] D. S. Petrov, M. Holzmann, and G. V. Shlyapnikov, Phys. Rev. Lett. **84**, 2551 (2000).

[104] G. Baym, Phys. Rev. A **69**, 043618 (2004).

[105] H. J. Lewandowski, Ph.D. thesis, University of Colorado (Boulder), 2001.

Appendix A

Numerical TOP trap model

What follows is a brief outline of the numerical TOP trap simulator that has been passed down through the generations. In this code the condensate position is found from locating a minimum in the combined magnetic plus gravitational potential. Trap frequencies are then determined from the second derivative of this potential at the condensate position. For this model we define the total potential as.

$$E_{potential} = E_{Breit-Rabi} + mgz \tag{A.1}$$

Here m is the mass of ^{87}Rb, g is 9.8 m/s^2 and z is the displacement from the quadrupole center. $E_{Breit-Rabi}$ is an augmented form of equation 3.7 of Heather Lewandowski's Thesis [105][1] .

$$E_{Breit-Rabi} = -\frac{h\nu_{hs}}{8} - g_I \mu_{bohr} B m_F \pm h\nu_{hs}\sqrt{1 + m_F x(B) + x^2(B)} \tag{A.2}$$

$$x(B) = (g_J + g_I)\frac{\mu_{bohr}}{h\nu_{hs}}B \tag{A.3}$$

Here ν_{hs} is hyperfine splitting for ^{87}Rb and h is planks constant. F and m_F refer to the magnetic state of the atom being trapped (F=1 and $m_F = -1$ for the purpose of

[1] Note that this is not the same as equations 3.2 and 3.3 of Matthews [59] which appears to contain a typo

this thesis), and B is the magnitude of the instantaneous magnetic field. Using the full Breit-Rabi equation is clearly over kill for the application described in §2.3, but the generality of this method is useful in calculating two-photon transition frequencies [59] not discussed in this thesis. The magnetic field, B, can be broken into two key parts: the magnitude of the bias field B_0, and the gradient to the quadrupole field along the z axis B'_q. In these terms B can be written

$$B = \sqrt{(\frac{B'_q}{2}x + B_0\xi_1 sin(2\pi\nu t))^2 + (\frac{B'_q}{2}y + B_0\sqrt{1-\xi_1^2}cos(2\pi\nu t))^2 + (B'_q z + (-1)^{(f+1)}\frac{2h\nu}{\mu_{bohr}})^2}\,. \tag{A.4}$$

This is a slightly more concise form of equation 3.16 from Matthews [59]. Note that the $2h\nu/\mu_{bohr}$ term is an effective field that arises from the inability of the atom spin to adiabatically track the rotating bias field, otherwise known as the wierd Bohn effect (see [59]). The TOP frequency, ν, is 1800 Hz for the purpose of this thesis. The parameter is ξ_1 inserted to model the effect of the distorted bias field. Using the notation from §2.2 the distortion of the rotating bias field has the form

$$\varepsilon = \frac{1-\xi_1/\sqrt{1-\xi_1^2}}{1+\xi_1/\sqrt{1-\xi_1^2}}. \tag{A.5}$$

Table A.1: Table of useful constants, largely from Lewandowski [105]

constant	value	unit
μ_{bohr}	$9.27400899(37) \times 10^{-28}$	J/G
ν_{hs}	6834.68261090434(3)	MHz
g_J	2.00233113(20)	
g_I	$.9951414(10) \times 10^{-3}$	

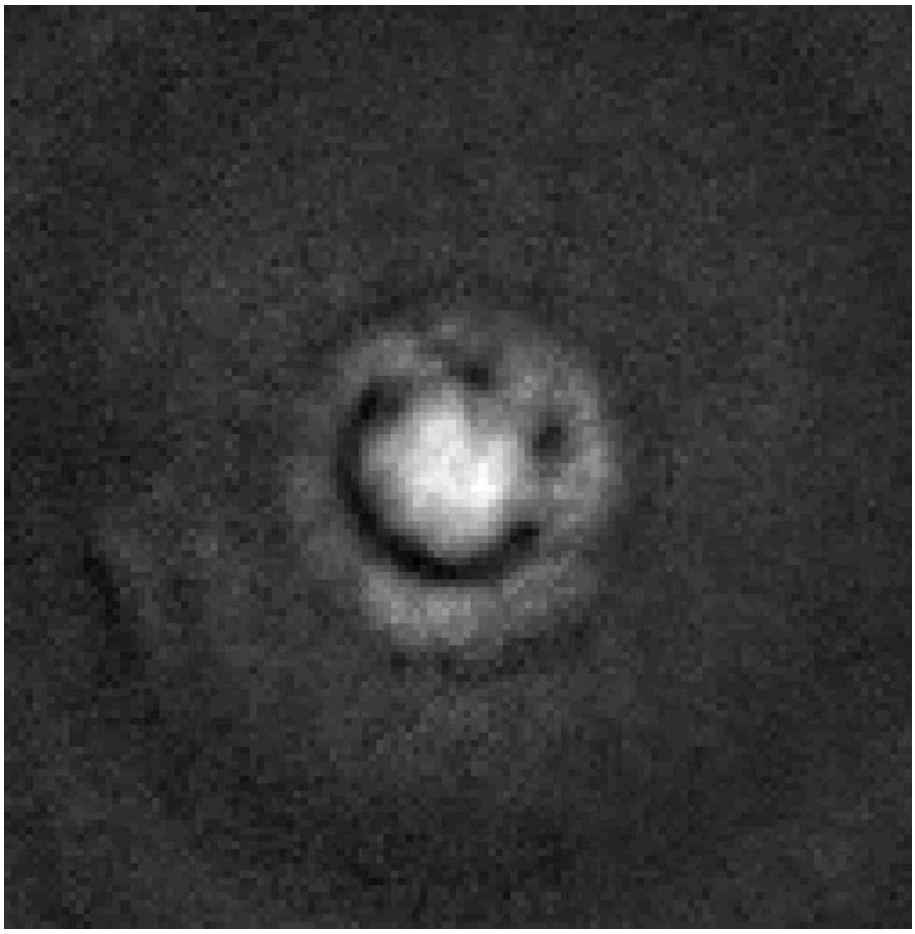

Figure A.1: